Transport within protocell-nanotube networks and its implications for communication of primitive cells

Ingrid Jin Schanke

Thesis submitted for the degree of
Master in Biomolecules and Soft Matter
60 credits

Department of Chemistry
Faculty of Mathematics and Natural Sciences

UNIVERSITY OF OSLO

June 2021

Transport within protocell-nanotube networks and its implications for communication of primitive cells

Master's thesis in Chemistry

Ingrid Jin Schanke

2021

Transport within protocell-nanotube networks and its implications for communication of primitive cells

Ingrid Jin Schanke

http://www.duo.uio.no/

Print: Reprosentralen, University of Oslo

Abstract

Protocells are self-organized primitive compartments which are thought to be precursors to first living cells at the origin of life. Several different types of model protocell structures have been proposed; among them, the most recently identified protocell nanotube networks (PNNs). A PNN consists of tens of surface adhered lipid compartments physically connected via lipid nanotubes. In this work, it is shown for the first time using differential interference contrast (DIC) microscopy that the PNNs can successfully form by using lipid compositions that are completely label-free. It has also been shown via confocal microscopy that the lipid nanotubes allow the transport of fluorescently labeled water soluble compounds, RNA and DNA among the compartments in the network. By employing fluorescence recovery after photobleaching (FRAP) technique, the diffusive redistribution of encapsulated fluorophores among compartments that are not in direct contact with each other, has been depicted. Results show that the transportation of the compounds in PNNs is possible due to the interconnecting nanotubes, which is proposed as a plausible chemical communication and replication mechanism between the protocells on the early Earth.

Acknowledgements

The work presented in this thesis was carried out at Forskningsparken, Centre for Molecular Medicine Norway (NCMM) as a part of the master's program at the Department of Chemistry, University of Oslo, from August 2019 to June 2021, under supervision of İrep Gözen.

First and foremost, I want to thank my supervisor, İrep Gözen, for introducing me to her group and giving me the opportunity to work on a very interesting topic concerning the origin of life. Thank you for your patience and generous support.

I wish to give a special thanks to Lin for assisting me with recording data for the thesis, and I want to express my gratitude to my other group members, Karolina, Elif, Inga, Aysu and Maivizhi, for all their advice and support, and for providing a comfortable working environment.

Finally, I would like to thank my parents for their unconditional love and for always believing in me, and last but not least my partner, Espen, for his encouragement and emotional support.

Table of contents

Terms and abbreviations

ATTO488	brand name of a fluorescein derived dye delivered by Sigma-Aldrich
Ca-HEPES	HEPES-buffer with sodium and calcium
DIC	differential interference contrast
DMPC	dimyristoylphosphatidylcholine
DPG	diphosphatidylglycerol
EPL	E. coli polar lipid extract
ER	endoplasmic reticulum
FAM	fluorescein amidite
FITC	fluorescein isothiocyanate
FRAP	fluorescence recovery after photobleaching
GUV	giant unilamellar vesicle
LUCA	last universal common ancestor
LUV	large unilamellar vesicle
MLV	multilamellar vesicle
NA	numerical aperture
Na-HEPES	HEPES-buffer with sodium
NVN	nanotube-vesicle network
PA	phosphatidic acid
PBS	phosphate buffered saline
PC	phosphatidylcholine

PDMS	polydimethylsiloxane
PE	phosphatidylethanolamine
PG	phosphatidylglycerol
PI	phosphatidylinositol
PNN	protocell-nanotube network (spontaneously formed NVN and a protocell model)
PS	phosphatidylserine
PVD	physical vapor deposition
ROI	region of interest
SPL	soybean polar lipid extract
SUV	small unilamellar vesicle

1 Introduction

Abiogenesis, i.e., origins of life is one of the pending yet fundamental questions in life sciences. In order to establish exactly how and when the transition from a soup of molecules to a living structure occurred, life must be defined first. The capacity of self-replication and Darwinian evolution, i.e., natural selection based on adaptability, are considered to be the key features that describes life [1]. Top-down approaches traces the lineage history of modern cells to their hypothetical last common universal ancestor (LUCA) to predict which molecules are persistently important for biological systems [2]. Bottom-up studies start from the simplest cell-like compartments structures and make it gradually more complex towards LUCA.

The genetic information required for self-replication flows from the DNA to RNA to protein and this is common for all living cells today. Information stored in DNA can be used to make new DNA (replication) or to synthesize RNA (transcription). The RNA is then used as a template in protein synthesis (translation). This order is called the *central dogma* of molecular biology [3]. The synthesis of proteins relies on the sequence of the nucleotides in DNA and RNA, but the amino acid sequence of a protein cannot be used to make either RNA or DNA. However, replication, transcription and translation are all processes that depend on proteins. These macromolecules are all essential in the self-replication and sustainability of cells, but their synthesis is dependent on each other. The debate focusing on identifying which came first, the protein or nucleic acids, is ongoing.

Many of the bottom-up theories regarding the origins of life can be sorted into the metabolism-first hypothesis, or the genes-first hypothesis. As the names suggest, they differ in the order of which came first, stable metabolism or replicating genes, both are essential for living cells. A popular theory is the RNA-world hypothesis which states that RNA molecules were synthesized first, and that they could replicate themselves before the arrival of protein or DNA. The RNA-world revolves around ribozymes, which are RNA molecules that can store genetic information like DNA, but also act as catalysts in chemical reactions, like enzymatic proteins [1, 3, 4]. There are three points that support this hypothesis: RNA is likely to have appeared before proteins, as protein replication without RNA is implausible. Furthermore RNA nucleotides are easier to

synthesize than those of DNA, and the more stable DNA molecule could have evolved from RNA and gradually taken over its role [1].

DNA, RNA, and proteins are complex macromolecules which must have been synthesized and evolved from simple organic molecules at a time when the macromolecules themselves were not yet present. Thus, the simple organic molecules must have been catalyzed with the few compounds and energy resources that were available on the prebiotic Earth.

1.1 Early Earth and origins of organic molecules

The earliest signs of life was found in Australian stromatolites, a sedimentary rock containing laminated precipitates that are thought to have originated from microbes [5], dates to around 3.5 Gya (giga years ago) [6]. Hot springs on land [7, 8] and hydrothermal vents [9] have been proposed as possible locations for the origin of life where thermal energy could be used to catalyze chemical reactions and produce simple organic molecules, with the support of mineral surfaces [10].

Organic molecules have been successfully reproduced while mimicking early Earth conditions. Among the most famous studies is the Miller-Urey experiment. According to the experiment, one flask containing CH_4 (g), NH_3 (g), and H_2 (g) and a second flask, filled with water, were connected in a loop, imitating the early Earth's ocean and atmosphere, respectively. When the vapor of boiling water began circulating through the system and mixed with the gasses mentioned above, an electrical discharge (spark) was produced, corresponding to lightning providing the energy needed for chemical reactions. As a result, amino acids, the building blocks of proteins, under the abiotic conditions were formed [1].

It is speculated that certain organic molecules on early Earth, could be formed in outer space, and arrived on our planet with meteorites. For example, when the Murchison meteoritewhich was discovered in 1969, was analyzed, water, lipids, amino acids, monosaccharides (sugars), phosphate and nitrogenous bases were detected [1]. The findings support the panspermia theory [11], which suggests that space could have been the source of the missing organic building blocks of life, and that the life could have started and evolved throughout the Universe.

Besides the meteorites which have been suggested as a source for amphiphiles on the early Earth, chemical synthesis have been performed mimicking the early Earth conditions [12] which led to the synthesis of phosphatidylcholine (PC) [13] and phosphatidyletanolamine (PE) [14]. Suggested pathways have been also proposed for both oligopeptides [15] and ribonucleotides [16], which indicate that both simple proteins and RNA synthesis could in principle be possible.

Having some of the building blocks present, is not considered to be sufficient to initiate reactions towards abiogenesis. An essential step in the origin of life is to accumulate the various organic compounds so they can react with each other. By concentrating the reactants and catalysts together in an enclosed space, in a simple compartment, the chances of reactants to interact with each other increases significantly.

1.2 Protocell models and compartmentalization

A protocell is defined as a self-organized structure which can serve as a model for the hypothetical precursor of the first cells [2], and they are therefore considered to be the stepping-stone for the emergence of life [17]. Prior to the arrival of complex biochemical machinery, the protocells would have to be self-assembled structures [18]. How exactly protocells were formed on the early Earth and what their exact structural and dynamic properties were, are still open questions.

Several different types of protocell models have been suggested. Among the structurally most simple protocells is the so called coacervate. The coacervates are droplets of macromolecule-rich phase submerged in an aqueous phase, much like an oil drop in water. These structures are not surrounded by any membrane; the aggregated macromolecules are held together by intermolecular forces. The macromolecules in a coacervate can be almost anything, such as lipids, peptides, polyelectrolytes, sugar molecules and nucleotides [2, 19].

Protocells with an organized lipid membrane bear a higher resemblance to the current plasma membrane surrounded cells as we know today. Membrane-surrounding protocells are thought to have self-assembled from amphiphiles which were present on the early Earth and functioned as compartments which confine and protect the first genetic/biochemical reactions [20]. Compartmentalization is considered to be a fundamental principle of life [17], because the ability to concentrate and seclude substrates and catalysts to enhance the production of convenient

molecules, is essential for further evolution of functional protocells [21, 22]. Amphiphiles, such as fatty acids, can assemble without the establishment of covalent bonds thus the membrane does not have to be formed as a result of chemical reactions, as the nucleotides and amino acids do, to make nucleic acids and proteins. Self-assembled, spherical membrane compartments, freely suspending in an aqueous environment, are widely the most accepted protocell models so far.

Lipid membranes have multiple biological functions that are crucial to life. Membranes can adopt many shapes due to their fluid nature [23]. In addition to forming spherical compartments to make organelles, or small cargo vesicles, the membranes in cells can also make nanotubular structures and networks. Examples of a lipid tubular network is the endoplasmic reticulum (ER) which is known to extend into the cell to enhance communication with other cellular organelles [3]. Tubular structures called the stromules have also been observed between plastids of plant cells and are thought to aid intracellular transport [24, 25] while tunneling nanotubes are used for intercellular cell-to-cell communication [26], both in bacteria [27] and eucaryotes [26, 28]. Cells have also been observed leaving behind nanotubes during migration, an action that is speculated to be used in cell-to-cell communication with the cells that are trailing behind [29, 30].

1.3 Motivation and previous work

Study of the cell membranes is of great interest, as it can help to address for example the research problems related to the membrane-associated proteins with important biological functions. Surface-supported lipid membranes serve as suitable models to mimic the biomembranes. They consist of 2D membrane areas that are easy to monitor and work with, compared to free-floating vesicles [31, 32]. Other forms of model lipid membranes exist. In order to study tubular membrane structures and their ability to act as transport routes to distribute cargo between their connected compartments, vesicle-nanotube networks (NVN) have been previously fabricated. Simple surface-supported NVNs can be made by manually by using micro-capillary needles [33-36], and transport through the nanotubes can be investigated using fluorescence microscopy [34].

Recent findings show how membranous protocells can autonomously form and grow on mineral-like surfaces in an aqueous environment, leading to the protocell-nanotube networks (PNNs). To form PNNs, small lipid compartments bud from the nanotube networks and grow over time into

giant protocells. The formation of the nanotubes and growth of the protocell are spontaneous processes, and self-driven by the surface free energy of the system [37]. (cf. Background section for detailed mechanisms behind the PNN formation). Note that the word “vesicle” has been substituted with “protocell” to distinguish between the spontaneously- (PNN) and the manually-formed networks (NVN). All the protocells in the PNNs are essentially unilamellar vesicular compartments maintaining connection to lipid nanotubes.

Division of a protocell freely suspending in bulk solution, occurs via elongation of the vesicular compartment in bulk solution, contraction in the middle and eventual separation [38]. From a free energy point of view, this scenario has not been considered realistic. An experimentally feasible alternative division event has been reported where multilamellar vesicles in bulk transform into tubular vesicles due to fusion of micelles to the original compartment and later divide with gentle mechanical agitation of the sample [39].

Recently a new division hypothesis has been developed focusing on the PNNs [40]. According to this proposed model, the encapsulated content e.g., genetic material, can transport through the tubes to nearby vesicles, resulting in protocells carrying the same genetic content (replication). Upon gentle push of hydrodynamic flow, the compartments can physically separate from the rest of the population (division) and migrate [40]. The division of the first cells could therefore have occurred already when the protocell network is formed [37, 40].

The diffusive transport of fluorescein through toroidal membrane tubes has previously been demonstrated in nanotube-vesicle networks manually created with glass capillaries, leading to an evenly distributed fluorescein concentration among the vesicles within the network [41]. Further evidence for transport through the nanotubes of the PNNs would support the possibility of an alternative pathway for early, passive-diffusion based communication between the protocells followed by division [40], and corroborate that PNNs can be plausible models for primitive cell-like compartments.

1.4 Aim

The formation of PNNs was for the first time shown and characterized by Köksal et al. by using several different lipid compositions [37]. In the previous studies, 0.5-1% of dye-conjugated lipids

were added to view the membrane with fluorescence microscopy. It has been reported that labeling a protein with dyes can affect the function of the protein [42], or that the labeled target can interact with the membrane [43]. This opens up the possibility that the dye-conjugated lipids might have influenced the membrane dynamics and played a key role in PNN formation and development. It has not yet been ascertained if the protocell-nanotube network could be formed with the absence of these dye-conjugated lipids. Thus, one aim of this thesis is to confirm whether the protocell-nanotube network could be formed with pure, unlabeled phospholipids.

It was also previously shown that the fluorescent compounds could be encapsulated by the compartments, and these molecules could be redistributed through instant fusion with other compartments [37]. The possible transport of the contents through the nanotubes in the PNNs has not yet been explored. The main aim of this thesis is therefore to show that the nanotubes are open structures (not blocked by membrane defects) allowing the passage of contents and investigate the diffusional transport of compounds inside protocell-nanotube networks (**Figure 1**). By using fluorescently labelled compounds, we aim to monitor and quantify the fluorophore transport in the nanotubes by using optical microscopy.

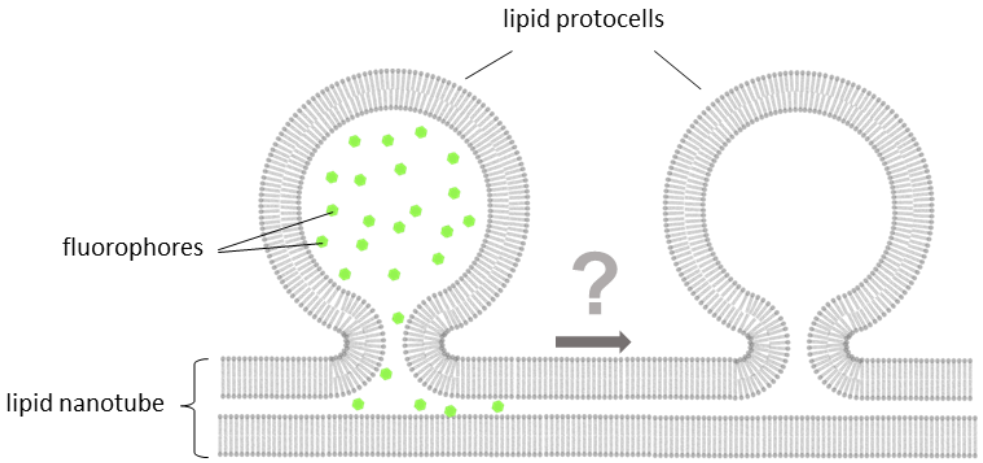

Figure 1: Schematic drawing showing the cross-sectional profile of a protocell-nanotube network. If the nanotubes are open, transport of compounds from one compartment to another through nanotubes, would be possible. The investigations on the possible transport via nanotubes, is the aim of this thesis.

In summary, there are two aims of this thesis: to find out whether PNNs can be formed from membranes consisting purely of unlabeled phospholipids, and if the nanotubes between the protocells of a PNN are open and can facilitate the communication between protocells.

2 Background

This section contains the basic theoretical knowledge that is necessary to get a deeper understanding of the lipid membranes, the main material used in this thesis work for model protocell formation.

2.1 Lipid chemistry

Lipids are one of the four major classes of biomolecules; alongside carbohydrates, proteins, and nucleic acids, they are the building blocks of life. Lipids are highly soluble in organic solvents, and they are classified as: free fatty acids, triacylglycerols, phospholipids, glycolipids, and sterols [44].

The simple fatty acids consist of a carboxylic acid followed by chain of hydrocarbons and are used to store energy which can be used to fuel the cells. Naturally occurring fatty acids usually have an even number of carbon atoms, ranging from 14 to 24 carbons [3, 44]. The fatty acids can be saturated, meaning no double bonds between the carbons, or unsaturated where they have one or a few double bonds, most commonly in a cis configuration at the end of the tail. The chain length and degree of saturation determine the properties of the fatty acid. As seen in **Figure 2**, the cis-double bond creates a kink in the hydrocarbon chain and limits the number of van der Waals interactions by preventing tight packing of the fatty acids. Likewise, the shorter chains have less opportunity for hydrophobic interactions [44]. Short tails and unsaturated cis configuration lead to fewer interactions between the fatty acids, which lowers their melting point [44].

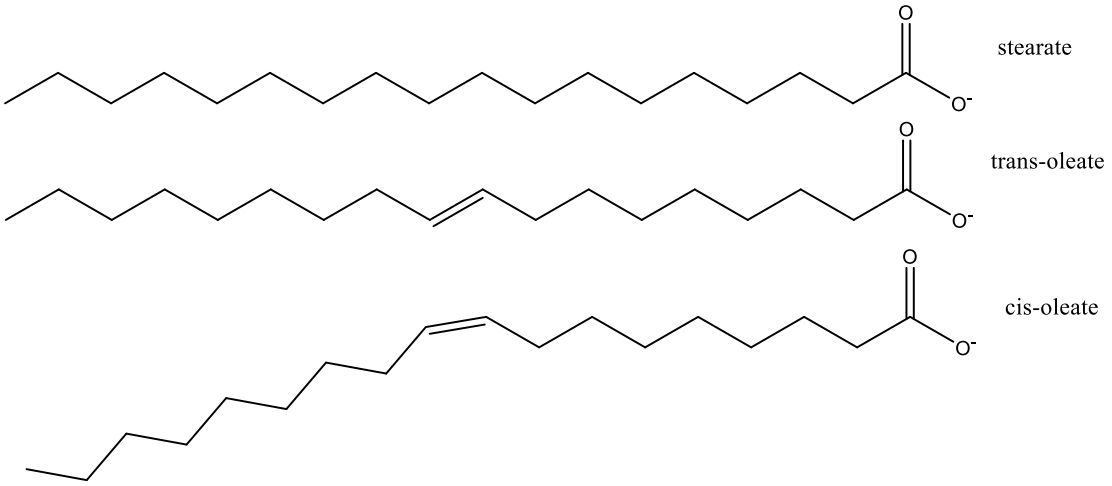

Figure 2: Ionized structures of C18 fatty acids, the saturated stearate and unsaturated oleate.

At physiological pH, the fatty acids are ionized and are represented by their carboxylate anion forms (**Fig. 2**). In the body, fatty acids are stored as acyl chains in triacylglycerols to prevent their acidic nature to disrupt the pH balance of the cells. Three arbitrary fatty acids are linked to a glycerol (propane-1,2,3-triol) backbone through esterification to create triacylglycerols. Esterification is the combination of an alcohol (ROH) and a carboxylic acid (RCOOH) to obtain an ester (RCOOR) and water (HOH). After three consecutive reactions, the glycerol which has gained three acyl chains becomes a triacylglycerol. It is also through esterification processes that many of the bigger lipids are formed. [44]

2.1.1 Phospholipids

Phospholipids, glycolipids and a sterol, cholesterol, are the three major lipids found in the membrane, with the former being the most abundant. The phospholipid molecule contains one or more fatty acids and a phosphate with an alcohol attached to it. The fatty acids and phosphate are connected to a platform, either glycerol or sphingosine through esterification. Phospholipids with glycerol backbones are called phosphoglycerides [44].

As stated by Jouhet [45, p. 2], “Major membrane phospholipids found in prokaryotes and eukaryotes are phosphatidylcholine (PC), phosphatidylethanolamine (PE), phosphatidylglycerol (PG), diphosphatidylglycerol (DPG) also called cardiolipin, phosphatidylinositol (PI), phosphatidylserine (PS), and phosphatidic acid (PA)”. These are all phosphoglycerides, with PA

being simplest one, having only a phosphate group at the end of its head. The other phosphoglycerides are derived from PA through ester linkage with alcohol groups of other molecules onto the phosphate of PA. Combination of PA and a choline molecule creates a PC as seen in **Figure 3**, where two myristic acids (saturated C12) are used to make dimyristoylphosphatidylcholine (DMPC) [44].

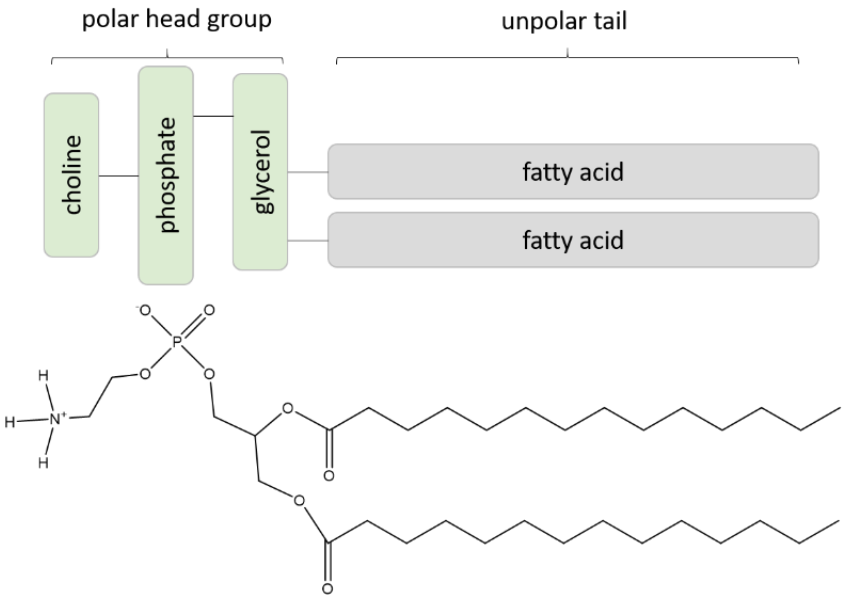

Figure 3: Structure of the phospholipid dimyristoylphosphatidylcholine (DMPC).

2.1.2 Lipid self-assembly

Lipids consist of a polar head-group and at least one long, nonpolar tail. This makes the lipid both hydrophilic and hydrophobic; a common term for containing both is amphiphilic. It is the long organic tail that make the lipids insoluble in water. When pure lipids are submerged in water, the hydrophobic region will not interact with the water molecules, and the presence of the freely floating tail will restrict the movement of the water molecules. This increases the order of the water molecules surrounding the chain [44], i.e., lowering the entropy, *S*, of the system. Since the entropy change is negative ($\Delta S < 0$), it results in an increase in Gibbs free energy, $\Delta G = \Delta H - T\Delta S$. This is unfavorable, as the system will always try to minimize its energy and become more stable.

One way of reducing the free energy is to minimize the hydrophobic area that is exposed to the water molecules. This effect, called the *hydrophobic effect*, causes the lipids to assemble to seclude

their tails from the water. Although the aggregation of lipids increases the order, the freed water molecules cause more disorder, and the net entropy change is negative. The lipids assemble spontaneously because it is a process that is self-driven by the hydrophobic effect [44, 46]. The geometry of the lipid molecule affects the type of assembly, and depends on a factor called the packing ratio, which is given by **Equation 1** [46, p. 332]:

$$N = \frac{V_c}{L_c\, A_h} \qquad 1$$

The V_c and L_c are the volume and length of the hydrophobic chain, respectively, and A_h is the effective area of the head group [46, p. 332-334]. Examples of structural aggregates the lipids can self-assemble into are shown in **Figure 4**. Lysophospholipids are phospholipids which contain a single acyl chain, and they generally have a large head group compared to the chain body. Such lipids will naturally form a positive curvature [45] upon gathering in a polar solvent (**Fig. 4a**). Lipids with packing ratios of $N \sim 0.33$ adopt spherical shaped micelles (**Fig. 4b**). At $N \sim 0.5$, the shape of the micelles become cylindrical, and they can pack together hexagonally (**Fig. 4c**).

In contrast, lipids with a small head group and a big tail make a negative curvature [45] (**Fig. 4d**). Simple fatty acids fall into this category. Correspondingly these lipids tend to self-assemble into inverted micelles (**Fig. 4e**) or hexagonally packed inverted cylindrical micelles (**Fig. 4f**) in nonpolar solvents.

Meanwhile, lipids with $N = 0.5–1$ prefer to arrange themselves into lamellar structured bilayers. Phospholipids with two alkyl chains are examples of such bilayer lipids. With a packing ratio slightly below 1, these bilayers are flexible and can form liposomes, i.e., vesicles (**Fig. 4h**), while lipids with packing ratio, $N = 1$, are arranged into real planar bilayer (**Fig. 4i**). Inverted liposomes can also exist, but only in nonpolar solvents [46, p. 332-334].

Many kinds of lamellar structures are given different names. Vesicles that are called unilamellar vesicles (UVs) consists of a single bilayer and they come various sized. A small unilamellar vesicle (SUV) is smaller than 100 nm in diameter. Large unilamellar vesicles (LUVs) ranges between 100 nm to 1 μm, and giant unilamellar vesicles (GUVs) are larger than 1 μm. Vesicles with more than one bilayer are called multilamellar vesicles (MLVs) and they contain a lot of lipids [47]. The

PNN arise from an MLV, creating many unilamellar protocells in a process that will be explained later.

The structure of the acyl chains incorporated in the phospholipid determines the properties of the membrane [48]. Adjacent phospholipids in a membrane can switch positions about 10^7 times per second, which means a lateral movement of 2 μm/s [49]. The fluidity of a membrane directly affects the permeability of the membrane, which regulates how easily molecules can pass. Even the water molecules can not readily pass, thus the biological cells employ aquaporins to allow the water to pass the membrane (up to $3 \cdot 10^9$ molecules per second) [49]. The restriction of ions and H^+ ensures that organelles can have the optimal pH for their respective enzymatic reactions, and allows the buildup of a proton gradient in the mitochondria, which is essential to produce energy [3].

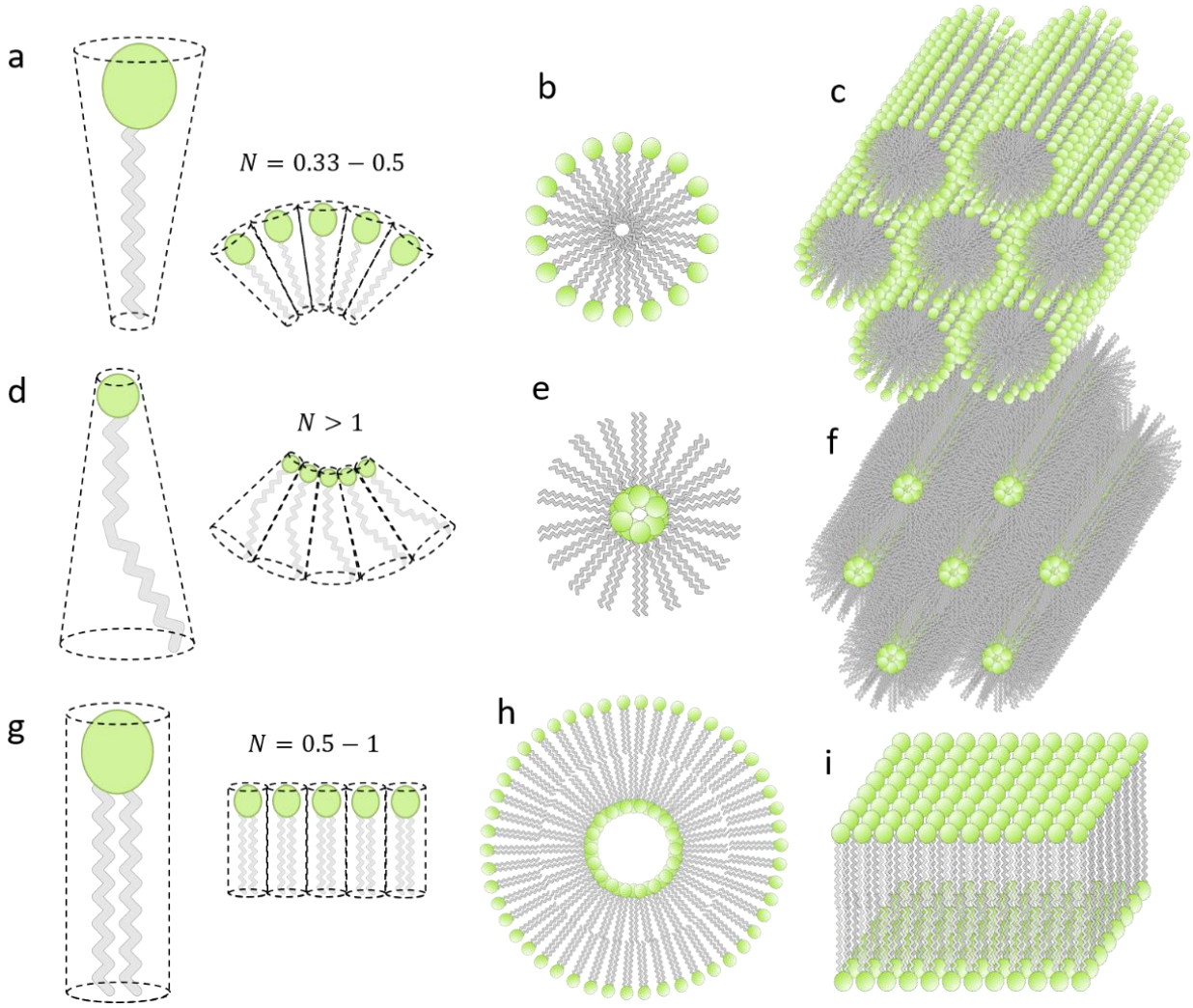

Figure 4: Lipids can self-assemble into various of aggregate shapes. (a) Lipids with large head group assemble into (b) spherical micelles or (c) cylindrical rods which can be packed hexagonally. In nonpolar solvents: (d) lipids with small headgroup arrange themselves into (e) inverted spherical micelles, or (f) inverted cylindrical micelles which can also be stacked hexagonally. (g) Lipids which structures resembles a cylinder, create less curvature, and they assemble into lamellar phases like (h) vesicles or (i) plane bilayers in aqueous solution.

2.2 Surface energy

It was briefly mentioned in the Introduction that mineral surfaces on the early Earth could have supported catalytical reactions [10]. In fact, it has been shown in [50] that minerals interacting with amphiphiles enhances the assembly of vesicles. To be able to explain how surfaces can facilitate membrane assembly at the mesoscale, an understanding of surface/interface energy is essential.

An interface is the region between two phases. The term is used when the phases are given by name, for instance, the water-air interface, or water-oil interfaces. For the three phases, solid, liquid and gas, there are five types of interfaces: solid-solid, solid-liquid, solid-gas, liquid-liquid, and liquid-gas. There is no boundary between gasses, thus a gas-gas interface does not make sense. The word "surface" is often used interchangeably with interface, preferably between a condensed phase (either a solid or liquid) and the non-condensed gas phase. For instance, the glass-air and water-air interfaces are usually called glass surface and water surface [46, p. 1].

At an interface, the situations of the atoms or molecules are different than in bulk. The surface of water is illustrated in **Figure 5**. In the bulk phase, each molecule is interacting uniformly with its surrounding neighboring molecules through the hydrogen bonds. The water molecules at the surface can only interact with a limited number of neighbors, creating a net force pulling the molecules into the bulk. Some energy is stored in the hydrogen bonds, and the surface molecules have fewer interactions, resulting in a higher free potential energy compared to the bulk, i.e., higher surface tension. The stronger the interactions are within the bulk, the higher the surface tension is.

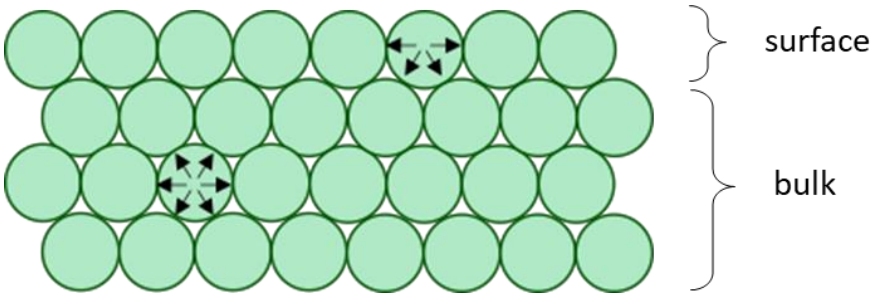

Figure 5: Interactions of the adjacent molecules to a water molecule at the surface compared to those in the bulk.

The system will try to minimize the surface area, to decrease the surface tension. The surface tension, γ, is defined in **Equation 2** as:

$$\gamma = \frac{W}{A} \qquad 2$$

and is given in units of (J/m^2 or N/m). W is the work needed to expand the surface by an area, A. The surface tensions of liquids are typically 20-80 mN/m [46]. For solid surfaces, this tension is usually called surface energy, and in this thesis, we look at tension and energy as the same.

Figure 6 illustrates a liquid drop (phase 1) on top of a solid material (phase 2), in a surrounding, second liquid (phase 3). At the edge of the drop, where all three phases meet, is also the meeting point between all three interfaces and their energies (γ_{12}, γ_{13} and $, \gamma_{23}$) can be seen as forces wourking on the drop (arrows). The angle, θ, between the γ_{12} and γ_{13} is called the contact angle.

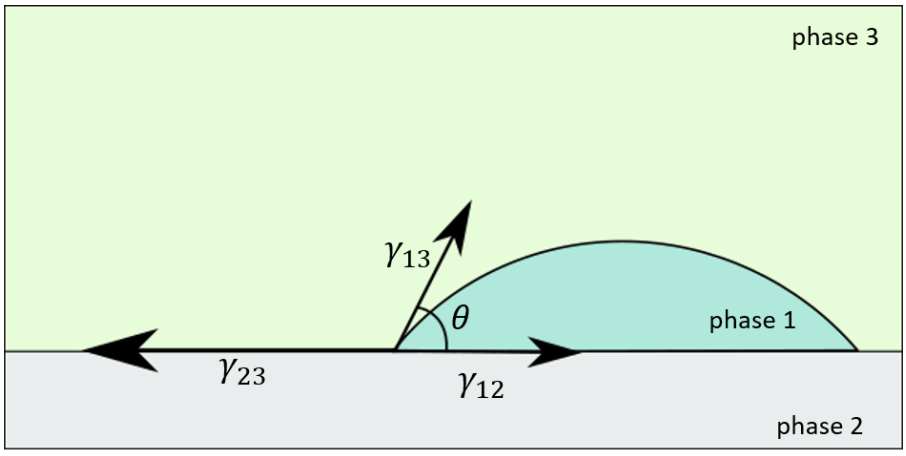

Figure 6: Interfacial energies working at the corner of a lipid drop.

The situation in **Fig. 6** can be described by **Equation 3** which is the Young's equation [46],

$$\gamma_{23} = \gamma_{13}\, cos(\theta) + \gamma_{12} \qquad 3$$

where θ is the contact angle between the liquid drop and the solid material. The interfacial energies act as forces on the drop, in the direction which minimize the total energy of the system. If the drop were to spread and wet the solid material, there would be an increase in the interfacial area between phase 1 and 2, as well as phase 1 and 3, but a decrease in interfacial area between phase 2 and 3. For a complete spreading the contact angle is zero, so $\cos\theta = 1$ and the spreading coefficient S_{12}, given by **Equation 4**:

$$S_{12} = \gamma_{23} - \gamma_{13} - \gamma_{12} \qquad 4$$

is zero. When $S_{12} \geq 0$, γ_{23} is larger than or equal to γ_{13} and γ_{12} added together, and it means that net force ecnourages spontaneous spreading. This means that wettability is favored by large γ_{23}. High-energy solid surfaces will therefore contribute to more spreading, and acording to de Gennes, "Most molecular liquids achieve complete wetting ($S \geq 0$) with high-energy surfaces" [51, p. 831]. Lipid membranes are 2D fluids which can wet mineral high energy surfaces. The mechanisms that drive nanotube and protocell formation relies in the (Helfrich) membrane energy, which will be explained in the following section.Methods

2.3 Membrane energy

Lipid membrane consists of two layers of lipid sheets, also called leaflets. Two leaflets with the hydrophobic tails facing each other make a bilayer which is about 5 nm thick [3]. A flat membrane can undergo deformation and be arranged into a variety of shapes and structures. The types of deformation are shear, thickness change, stretching and bending. In the plasma membrane, proteins can form raft domains that are segments of concentrated membrane proteins held together with weak interactions. These domains have an increased membrane thickness and their composition differ from the outside [3, p. 572]. Opposite (shear) forces on the two leaflets can therefore cause shear and thickness deformation in the membrane. In a pure lipid membrane without proteins, a uniform thickness and composition is assumed. Therefore, the only deformities to consider are

stretching and bending. The stretching and bending energies of a lipid bilayer can be summed up in **Equation 5**, which describes Helfrich's theory of membrane elasticity [52].

$$E = \int \left[\frac{1}{2}\kappa_b(c_1 + c_2 + c_0)^2 + \overline{\kappa}_b c_1 c_2\right] dA + \int \gamma \; dA \qquad 5$$

where the first term is the bending energy, and the last term is the stretching energy. The latter includes the membrane tension, γ, which is related to the stretching modulus, κ_a by **Equation 6** [52]:

$$\gamma = \kappa_a \frac{\Delta A}{A_0} \qquad 6$$

Here, ΔA is the surface area change, and A_0 is the inital surface area. The c_1 and c_2 in the bending term are the principal curvatures, and A is the surface area. κ_b is the bending modulus for rigidity and lies between $10 - 20\ k_bT$ [53], where $k_b = 1.38 \cdot 10m^{-23}J/K$ is the Boltzmann constant. The Gaussian bending modulus, $\overline{\kappa}_b$ is only important for systems undergoing drastic topological changes. The spontaneous curvature, c_0, appears when there is a variation in the lipid species comprising each monolayer leaflet. This does not apply to the membranes we used to form PNN. By omitting c_0 and $\overline{\kappa}_b$, the elastic membrane energy is simplified to **Equation 7** [53]:

$$E_{bend} = \frac{\kappa_b}{2}\int (c_1 + c_2)^2 dA \qquad 7$$

Various lamellar structures have different principal curvatures and surface areas, some of them are given in **Figure 7**, and their bending energies can be calculated using **Eq. 7**.

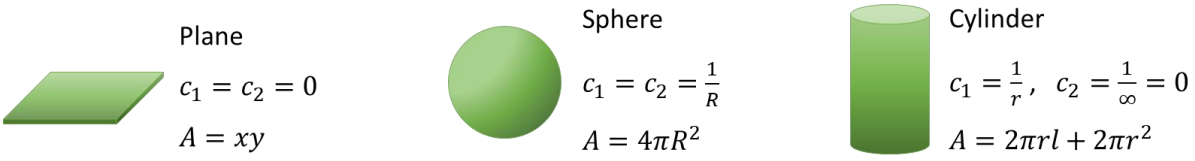

Figure 7: The principal curvatures and surface areas of different geometries. The cross sectional area of the cylinder is omitted [53].

For a plane membrane with no principal curvatures, there is no bending energy. A cylinder has a curvature of $\frac{1}{r}$, where r, is the radius of the cylinder. With the surface area of a tube being $2\pi rl$, where l is the length of the tube, the bending energy for a nanotube can be calculated as in **Equation 8**:

$$E_{b,nanotube} = \frac{\kappa_b}{2}\int\left(\frac{1}{r}\right)^2 dA = \frac{\kappa_b}{2}\cdot\frac{1}{r^2}\cdot 2\pi rL = \frac{\pi\kappa_b L}{r} \qquad 8$$

A sphere has two equal principal curvatures of $\frac{1}{R}$, where R, is the radius of the sphere. A spherical vesicle with the surface area of a cylinder, $4\pi R^2$, the bending energy for the vesicle is given by **Equation 9**:

$$E_{b,vesicle} = \frac{\kappa_b}{2}\int\left(\frac{2}{R}\right)^2 dA = \frac{\kappa_b}{2}\cdot\frac{4}{R^2}\cdot 4\pi R^2 = 8\pi\kappa_b \qquad 9$$

The bending energy of a pure lipid vesicle is independent of its size, since the radius has disappeared from the final term [54].

2.4 Protocell-nanotube network formation

The formation of phospholipid films on solid substrates have been investigated on several surface materials by Jõemetsa et al. [55]. Formation of monolayers, single bilayers, and double bilayers, were observed in this study, which depended on both the lipid composition and the surface. Lipid reservoirs (MLVs) form a double bilayer film upon contact with a high energy solid surfaces [56].

2.4.1 Double bilayer adhesion and spreading on the surface

In an aqueous environment, upon contact with a high-energy surface, a multilamellar vesicle (MLV) starts to spread on the surface due to adhesion; a process termed *surface wetting*. The spreading of the membrane on the solid surface is surface tension driven, where the system lowers the overall surface energy [57]. This is illustrated in **Figure 8**.

The interfacial energy between the SiO_2 surface and the aqueous ambient buffer is higher than the interface of a membrane covered surface, which leads to the spreading of the membrane in form of a double bilayer. The proximal bilayer (lower with respect to the surface) gets pinned to the surface as it spreads on the surface, while the distal (upper) bilayer keeps spreading on the proximal membrane. The MLV at the center of the spreading is the lipid source which provides lipid material to the expanding double bilayer. In addition, the edge of the spreading, where the proximal and distal membrane is connected has a sharp curvature, causing high membrane tension. The lipids in lower tension areas of the membrane will therefore be rapidly drawn to the spreading edge. The tension-driven flow of the lipids is due to the Marangoni effect [58]. The Marangoni flow directs the lipids in the distal bilayer to the edge, drawing material from the reservoir for continuous spreading.

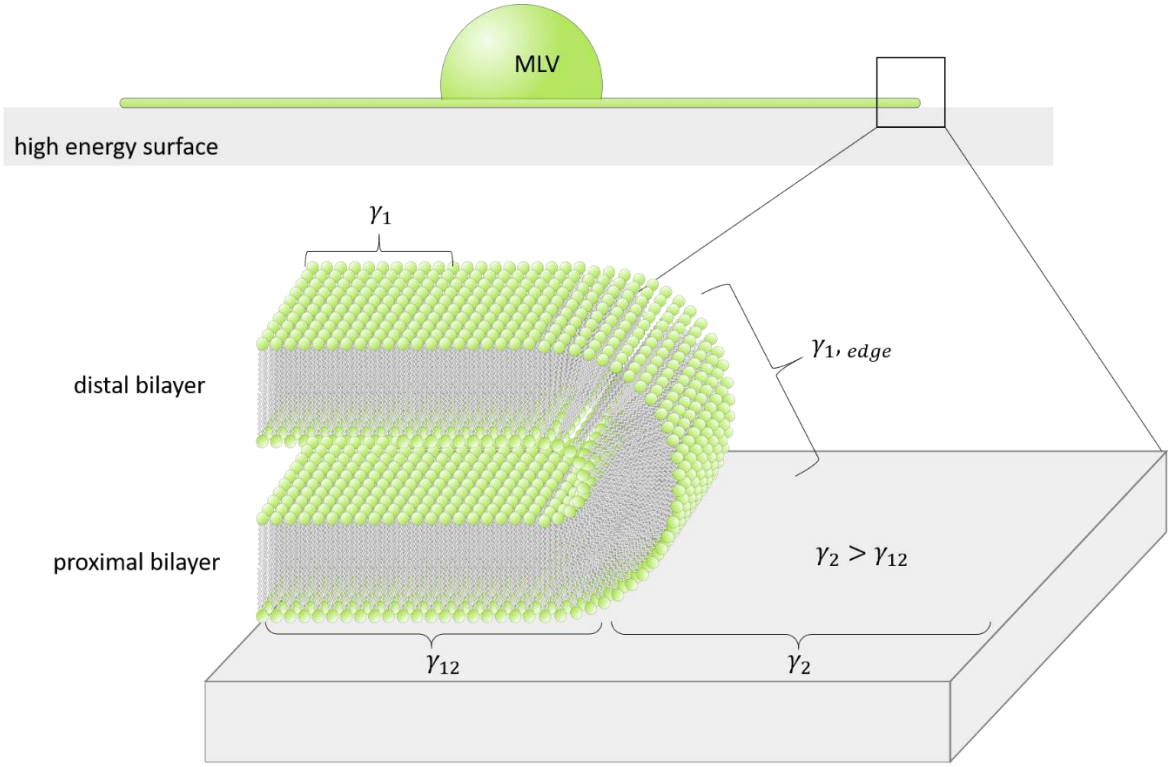

Figure 8: The surface tensions involved in the spreading. The membrane tension at the edge, $\gamma_{1,edge}$, is higher than the membrane tension elsewhere γ_1, because of the curvature. The interfacial energy between the membrane and the SiO_2 surface, γ_{12}, is lower than the energy of the aqueous buffer-substrate interface, γ_2.

2.4.2 Nanotube and protocell growth

At some point, the wetting of the surface by the membrane comes to a halt. The reason can be that the MLV is used up, or the spreading has proceeded so much that the amount of lipids needed for further wetting cannot be provided to the membrane edge fast enough. When this happens, the distal membrane becomes stretched and tense due to continuous adhesion [37].

Figure 9 illustrates the steps in PNN formation. When the tension becomes too high, the distal membrane shown in **Fig. 9a** eventually ruptures, and retracts on (de-wets) the proximal membrane and rolls out onto the surface [37]. Because Ca^{2+} in between the two bilayers promotes pinning [59] and the adhesion of the two bilayers, some regions of the distal layer remain intact during rupturing and remains adhered to the proximal layer (**Fig. 9b**). These fragments eventually become lipid nanotubes (**Fig. 9c**). Small vesicles bud from the nanotubes (**Fig. 9d**) and mature over time (**Fig. 9e**) [37].

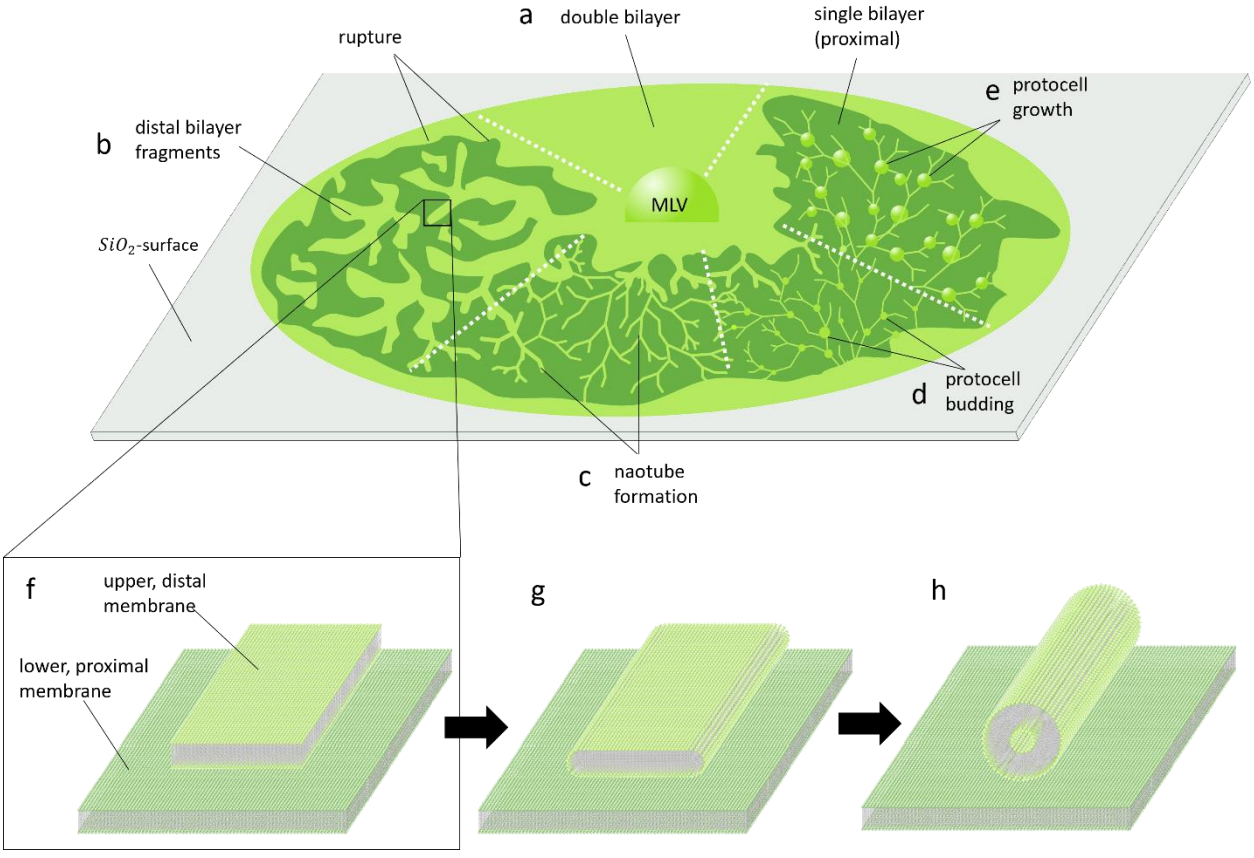

Figure 9: The steps in PNN formation after double bilayer spreading of an MLV. (a) intact double bilayer becomes tense and (b) the distal membrane ruptures. (b) Pinning of calcium between the upper and lower bilayer makes the retracting bilayer leave behind lipids in as elongated fragments (not to scale). The fragments (f) which in reality feature a curved edge (g) bend into a nanotube (h, not to scale), and the latter constitute nanotubes (c) from which protocells can emerge (d) and grow (e).

The transitions from lipid patches to nanotubes, and finally to protocells are driven by membrane tension and membrane energy. **Fig. 9f** shows a schematic drawing of a long distal membrane fragment formed during rupturing. This fragment is pinned by Ca^{2+} to the proximal bilayer. To shield the hydrophobic tails of the lipids at the ruptured edge, the bilayer instantly creates a strongly curved edge along the sides (**Fig. 9g**). The energy required to maintain the curved edge is proportional to the length of the edge and the membrane tension at the edge. **Equation 10** shows the edge energy of a circular pore with radius, r, and line tension, γ, for a membrane with thickness d_m [54]:

$$E_{pore} = 2\pi r \gamma d_m \qquad 10$$

For a narrow thread of membrane like in **Fig. 9f**, the edge energy is proportional to the length of the membrane, and **Eq. 10** can be written as **Equation 11**:

$$E_{edge} = 2\mathrm{L}\gamma d_m \qquad 11$$

According to Sackmann [54], $\gamma d_m = 5 \cdot 10^{-11}\ N$ at room temperature for a membrane that is composed of phospholipid DMPC (structure in Fig. 3). The edge energy required to create an edge along the sides of a 10 μm long DMPC membrane is calculated with **Eq. 11** and in an order of $2 \cdot 10^5\ k_b T$.

Another way to shield the lipid tails from the water is shown in **Fig. 9h**, in which, the membrane bends to form a nanotube. **Eq. 8** shows that the energy required to bend an elongated membrane region into a nanotube is $\frac{\kappa_b \pi l}{r}$. The bending energy for a 10 μm nanotube with 50 nm radius is in the order of $7 \cdot 10^3\ k_b T$, for T=300 K and $\kappa_b = 0.5\ J$. The edge energy required to maintain the membrane in its flat form is about a 100-fold higher than the bending energy cost required to form a nanotube from it. As a result, the formation of a nanotube is more favorable.

A nanotube, however, still has a high curvature and energy. In comparison, a vesicle with the same lipid composition and of any size would have a bending energy in the order of around $100\ k_bT$. Over time, the highly curved nanotube fragments swell where membrane curvature is reduced, leading to the formation of spherical lipid compartments: model protocells. The membrane material required for swelling is either obtained through consuming the nanotubes (complete transformation of a nanotube to a spherical compartment) or is provided by the flow from the reservoirs in remote locations through connected nanotubes (Marangoni effect).

3 Methods

This section will focus on the methods and setup employed to perform the experimental work discussed in this thesis. The utilized methods are the preparation of lipid suspensions and vesicles, preparation of the sample chamber, fluorescence and differential interference contrast (DIC) microscopy, application of an open-volume microfluidic device for superfusion. A detailed description of the important microscope techniques along with FRAP is included.

3.1 Chemicals and buffer solutions

Deionized (DI) water (acquired with a Millipore Milli-Q® Gradient A10 water purification system from Merck) was used for the preparation of all buffers. Cleaning of all items, e.g., glassware, was done following the same procedure: rinsing with isopropanol three times, followed by rinsing with water three times, and blow-drying with N_2.

Following chemicals were obtained from Sigma-Aldrich/Merck (Darmstadt, Germany):

- 4-(2-hydroxyethyl)-1-piperazineethanesulfonic acid (HEPES, titration, ≥ 99,5%)
- NaCl (for molecular biology, titration, ≥ 99%)
- $CaCl_2$ (anhydrous, BioReagent grade, ≥ 96%)
- 2-Amino-2-(hydroxymethyl)-1,3-propanediol (Trizma base, crystalline, titration, ≥ 99,9%)
- K_3PO_4 (reagent grade, ≥ 98%)
- $MgSO_4 \cdot 7H_2O$ (BioUltra grade, KT, ≥ 99,5%)
- ethylenediaminetetraacetic acid disodium salt dihydrate (EDTA-Na_2, ACS reagent grade, 99.0 - 101,0%)
- H_2KPO_4 (anhydrous, ACS reagent grade, ≥ 99%)
- chloroform (anhydrous, ≥ 99%)
- glycerol (≥ 99%)
- Soybean polar lipid extract
- E. coli polar lipid extract
- 16:0 Rhod Liss PE

Sylgard™184 was purchased from Electron Microscopy Sciences. ATTO488 carboxy was purchased from Atto-Tech, and the nuclease-free water from Thermo Fisher Scientific. Fluorescein amidite (FAM) conjugated to single-stranded 20-base DNA (5'/56-FAM/TGT ACG TCA CAA CTA CCC CC-3') were obtained from Integrated DNA Technologies, USA. Fluorescein isothiocyanate (FITC) conjugated to 10-base RNA oligomer (5′-FITC-AAA AAA AAA A-3′) were obtained from Dharmacon, USA.

3.1.1 Buffer preparation

Three types of buffers were used during the experiments. Two types of HEPES buffer were used. One without Ca^{2+} to rehydrate dry lipid films, and one with Ca^{2+} to promote spreading of MLVs. The amount of chemicals in the HEPES buffers and the phosphate buffered saline (PBS) are listed in **Table 1** and **Table 2**, respectively.

Table 1: HEPES buffer

Chemicals	**Concentration (mM)**	**Mass (g)**
HEPES	10	1.906
NaCl	100	4.675
$CaCl_2$	4	0.177

To prepare the HEPES buffers, HEPES and NaCl in the stated amount in **Table 1** were added to a cleaned glass bottle with 796 mL DI water and stirred with a magnetic stirrer. The solution was then divided equally into two bottles, each containing 398 mL $CaCl_2$ was added to one of the bottles under stirring, creating one buffer with 4 mM Ca^{2+} calcium (Ca-HEPES) and the other one free of Ca2+ (Na-HEPES). The pH of the buffers was adjusted to 7.8 with 1M NaOH solution. The buffers were vacuum filtrated through a 0.2 nm filter and aliquoted into 50 mL falcon tubes and kept in -20 ℃ until use. The frequently used solution tube was kept in fridge at 4℃

Table 2: PBS buffer

Chemicals	**Mass (g)**
Trizma base	0.2424
K_3PO_4	2.5474
$MgSO_4 \cdot 7H_2O$	0.1390
Na_2EDTA	0.0749
KH_2PO_4	1.63
$MgSO_4 \cdot 7H_2O$	0.1390

For the preparation of the PBS buffer, 398 mL DI water was first added to a cleaned glass bottle and heated to 50℃. The chemicals were added under stirring in the order that is listed in table 2. The $MgSO_4 \cdot 7H_2O$ was added in two steps and the solution was stirred for 1 h in order to completely dissolve it. The pH was adjusted to 7.4 with H_3PO_4. The buffer was filtered, aliquoted to 50 mL falcon tubes, and stored in the same way as the HEPES buffers.

3.2 Preparation of lipid suspensions

Labeled and unlabeled lipid stock solutions of different compositions were prepared using the dehydration-rehydration technique [60] from soybean polar extract (SPL) and E. coli polar extract (EPL). As the first step, the lipid suspensions of 3000 μg lipids, including the lipid-conjugated fluorophores (1%), were dissolved in 300 μL chloroform in a glass vial. **Table 3** through **Table 6,** show the lipid composition of several stock lipid suspensions used in this thesis, the amount of lipid and the lipid-conjugated dye, 16:0 Rhod Liss PE (Rhod PE), that were used to prepare them. The final mixtures all have a lipid concentration of 10 mg/ml. Detailed lipid species in SPL and EPL are listed in **Table 7** and **Table 8** in the Appendix.

Table 3: Unlabeled lipid suspension made of SPL (100 wt%)

	Concentration (mg/mL)	**(wt%)**	**Lipid mass (μg)**	**Volume chloroform (μL)**
SPL	25	100	3000	120

Chloroform				180
Total			3000	300

Table 4: Labeled lipid suspension made of SPL-Rhod PE (99:1 wt%)

	Concentration (mg/mL)	**(wt%)**	**Lipid mass (µg)**	**Volume chloroform (µL)**
SPL	25	99	2990	118.8
Rhod PE	1	1	10	30
Chloroform				151.2
Total			3000	300

Table 5: Unlabeled lipid suspension made of SPL-EPL (50:50 wt%)

	Concentration (mg/mL)	**(wt%)**	**Lipid mass (µg)**	**Volume chloroform (µL)**
SPL	25	50	1500	60
EPL	25	50	1500	60
Chloroform				180
Total			3000	300

Table 6: Labeled lipid suspension made of SPL-EPL-Rhod PE (49:50:1 wt%).

	Concentration (mg/mL)	**(wt%)**	**Lipid mass (µg)**	**Volume chloroform (µL)**
SPL	25	49	1490	58.8
EPL	25	50	1500	60
Rhod PE	1	1	10	30
Chloroform				151.2
Total			3000	300

The steps for lipid preparation have been illustrated in **Figure 10**. Subsequently, the mixture was transferred to a 10 mL cleaned pear-shaped bottom flask and placed in a rotavapor where the lipid mixtures were evaporated at 24 rpm and reduced pressure (20 kPa) in 23 ℃ water bath. The chloroform inside the flask evaporated over 6 hours. 3 mL PBS and 30 µL glycerol was added to the dry lipid film in the flask and kept at 4℃ overnight for swelling. The following day, the suspension was sonicated for 5-10 s, 100 µl aliquots were prepared and stored at -18℃.

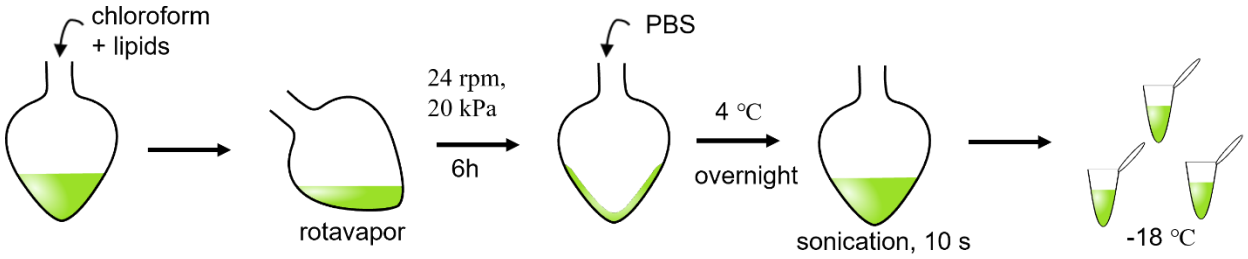

Figure 10: Preparation of lipid suspensions.

3.3 Sample preparation

The steps for sample preparation are illustrated in **Figure 11**. To prepare the samples, a 4 µL drop of thawed lipid suspension (section 3.2) was placed on a clean glass cover slip using an automatic pipette. The cover slip was then placed in a desiccator and dehydrated for 20-25 min under low pressure. The dry lipid film was rehydrated with 0.5-1 ml of Na-HEPES buffer for 10 min. The rehydration drop was aspirated with a Pasteur pipette to the observation chamber.

A silicon-frame made from polydimethylsiloxane (PDMS), adhered on the SiO_2-surface constitutes the observation chamber (**Figure 11**). The PDMS was made by mixing the Sylgard™184 elastomer base and curing agent in a 10:1 ratio and baked in a silanized glass petri dish at 100℃ for one hour [61]. A frame with desired shape and size can be cut out from the PDMS layer formed in the petri dish. The fabrication of the SiO_2-surface is explained in the next section. The SiO_2-surface was plasma cleaned for 5 minutes, and a clean, PDMS-frame was air-sealed on the SiO_2-surface. The chamber was filled with the Ca-HEPES buffer to which, the rehydrated lipids were added.

A petri dish with closed lid was used to store the sample at room temperature for 2-3 days for PNN formation and protocell growth. Ca-HEPES was added to the sample periodically to prevent it from drying out due to evaporation. Alternatively, to speed up the protocell growth, the sample was incubated in 35°C until the following day. Temperature was previously shown to facilitate the vesicle growth [62]. The samples containing the PNNs were then brought to the microscope for inspection and experiments.

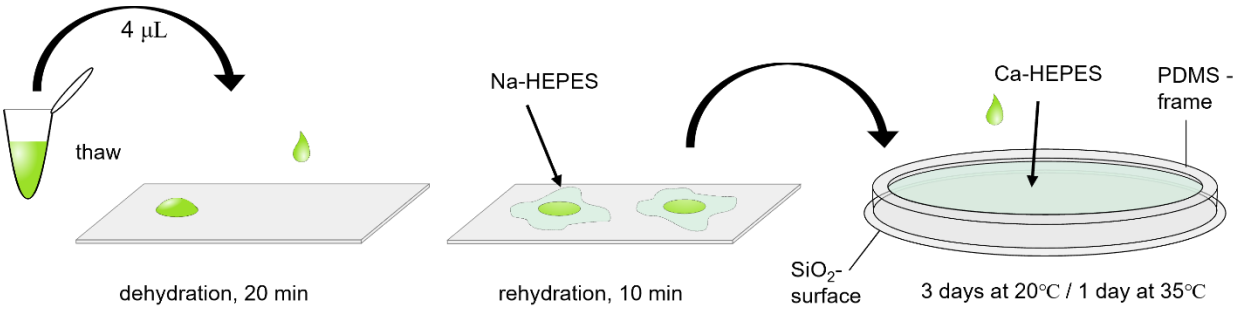

Figure 11: Sample preparation.

3.4 Surface fabrication

SiO_2-surfaces were fabricated in UiO MiNaLab, at the Norwegian Micro- and Nano-Fabrication Facility, NorFab, by using physical vapor deposition (PVD), with the Angstrom E-beam instrument.

PVD is used to deposit atomically thin films of a material onto a substrate; a simple schematic is shown in **Figure 12**. Briefly, the deposition material is placed in a crucible and heated under vacuum, until it evaporates. The vacuum minimizes interactions with other gas molecules and makes it possible for the vaporized material molecules to move in a straight path, hitting the substrate that is mounted on the sample holder above the crucible. The vaporized material condensates onto the substrate [46]. The Angstrom instrument uses an electron beam (E-beam) to evaporate silica pellets. The E-beam is guided to the crucible by an electromagnetic field. Using PVD with E-beam evaporation, glass cover slips were covered with a 84 nm thick layer of SiO_2.

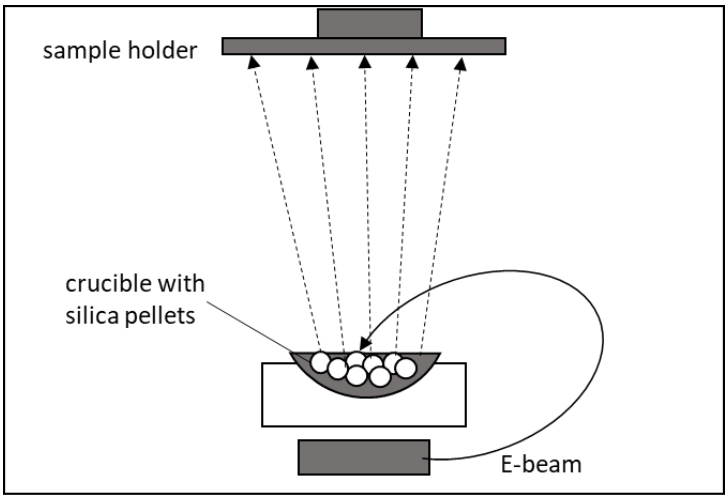

Figure 12: Schematic drawing explaining the basic principle of PVD with E-beam evaporation.

3.5 Microscopy and imaging

Two different fluorescence microscopes were used to capture the resulting images presented in this thesis: An epi-fluorescence microscope was used to capture static images of the networks: a Nikon Eclipse Ti2 combined with a Prime 95B camera from Photometrics. The other is a laser scanning confocal microscope (Leica DMi8), which was used in encapsulation and FRAP experiments. Both are inverted microscopes, with the light source and the condenser situated above the stage, while the objective is under the sample stage. **Figure 13** shows a photograph of the main components of the confocal microscope most frequently used for imaging in this thesis.

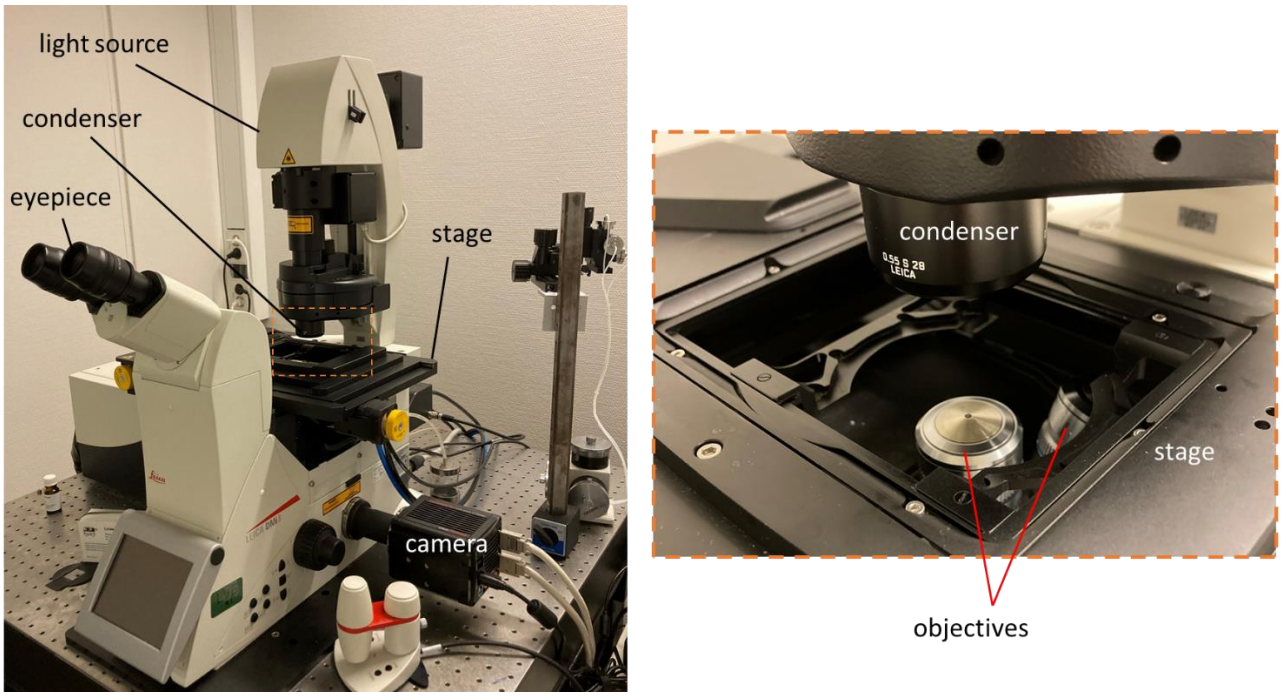

Figure 13: Photograph of the confocal microscope. It is an inverted microscope with condenser and light source positioned above the stage (left), and the objectives located underneath the stage (right).

Either a 40x objective or the 60x objectives were used with numerical apertures (NAs) of 1.3 and 1.4, respectively. Both were immersion objectives which require the use of oil with high refractive index. When loading the sample onto the stage, a drop of Leica Immersion Oil (standard and type "F") was placed between the cover slip and the objective front lens. The oil has a refractive index of 1.51, which is similar to the refractive index of glass. When light travels between media of high to low refractive indices, the refracted angle becomes larger than the incident angle. Having air as a medium between the sample and the objective instead of oil, causes refraction, lowering the resolution. Since the indices of the oil and glass are almost the same, with the use of immersion oil, the refraction at the interface can be reduced, hence more light reaches the objective resulting in high resolution. [63]

There are two ways to illuminate a sample: via transmitted (diascopic) and reflected light (episcopic). Simple schematics of the two methods are shown in **Figure 14**. Transmitted illumination is used in DIC and other bright-field techniques. The detector is at the opposite side of the light source, with respect to the sample. This means that the light coming from the light

source passes the sample where changes in transmitted light due to the structure and thickness of the sample, is detected by the detector.

Reflected illumination is used for fluorescence microscopy, where the light used to illuminate the sample is not the light that is detected. In this setup, the laser light is used to excite the fluorescent molecules in the sample, and the emitted fluorescence light is detected. The dichroic mirror allows light of certain wavelengths to pass through the material, while other wavelengths are reflected [64, 65]. More detailed information about fluorescence microscopy has been presented in the next section.

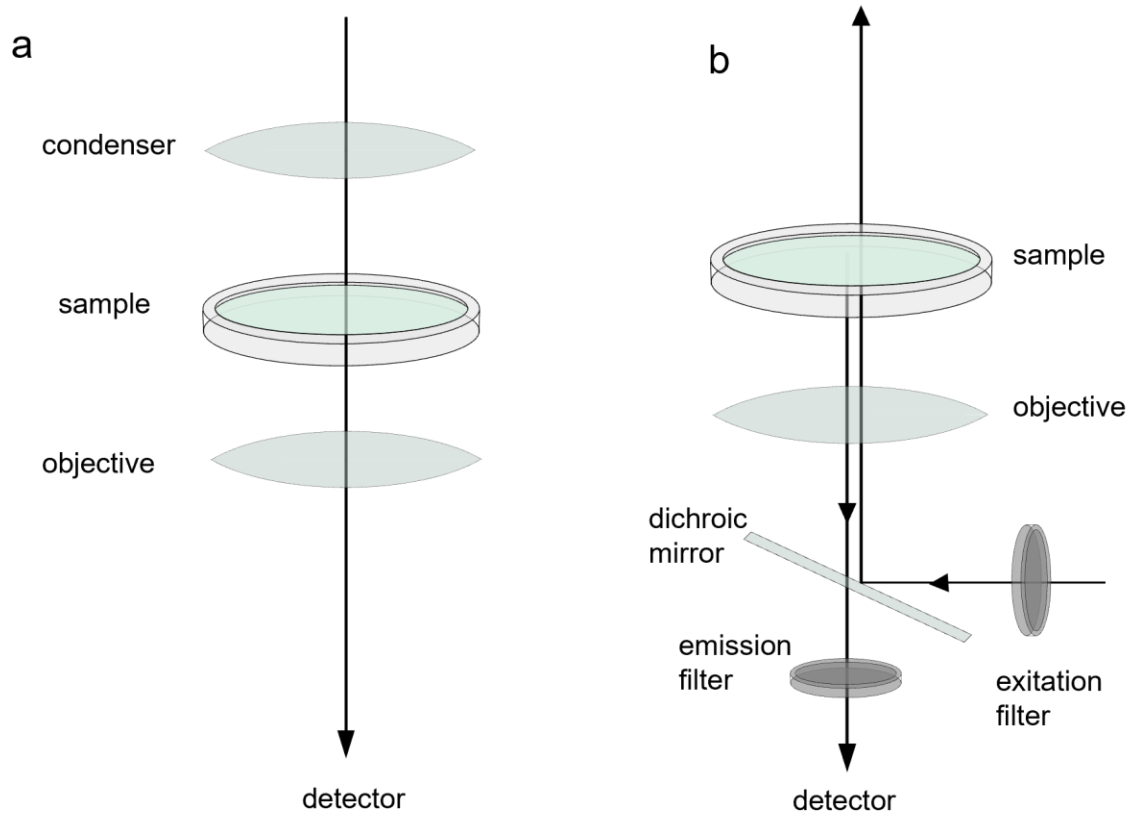

Figure 14: Simplified schematics of transmitted and reflected illumination. In transmitted illumination the light source and the objective are on opposite sides of the samples, and the light travels through the sample (left). During reflected illumination, the light source and the objective are on the same side relative to the sample (right). The light is reflected onto the sample with a dichroic mirror.

3.5.1 Fluorescence microscopy

Fluorescence is the light emission in the form of a photon during the relaxation of an excited fluorophore molecule. The Jablonski diagram in **Figure 15** shows the electronic states of a fluorophore molecule and the transitions between them [66]. During absorption, an electron in the ground energy state is excited to a higher energy state. This can happen during the exposure of the fluorophore molecule to laser light. The electron then returns to lower energy levels through non-radiative transitions, followed by releasing a photon i.e., light emission. Due to the non-radiative transitions, the energy of emitted photon is lower than the energy of the excited electron.

The energy of the photon is given by $E = \frac{c}{\lambda}$, where λ is the wavelength of the oscillating light. Since the speed of light, *c*, remains unchanged, the wavelength at which the emission occurs, is shifted to the right of the spectrum as illustrated to the right in **Fig. 15**.

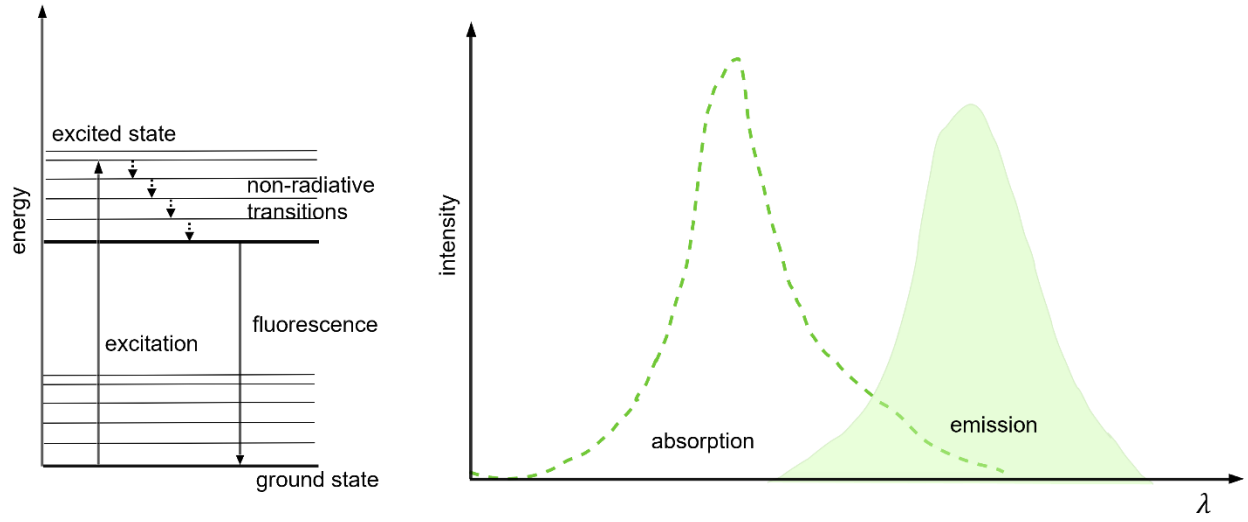

Figure 15: Jablonski diagram (left) and absorption-emission spectra for an arbitrary fluorophore (right).

The distance between the absorption maxima and the emission maxima is called the Stokes' shift. In fluorescence microscopy, a laser of certain wavelength, specifically around the absorption wavelength of the fluorophore is used to excite the molecule, and the fluorescence emission is collected at a longer wavelength.

To use fluorescence microscopy, a molecule capable of fluorescence -a *fluorophore*- is required. **Figure 16** shows structures of the fluorophores used in this thesis. The fluorescent molecules are

derived from the fluorescein molecule and are water soluble. All dyes have similar absorption and emission spectra. The fluorophores were excited by 495 nm light, and emission was collected 510-560 nm.

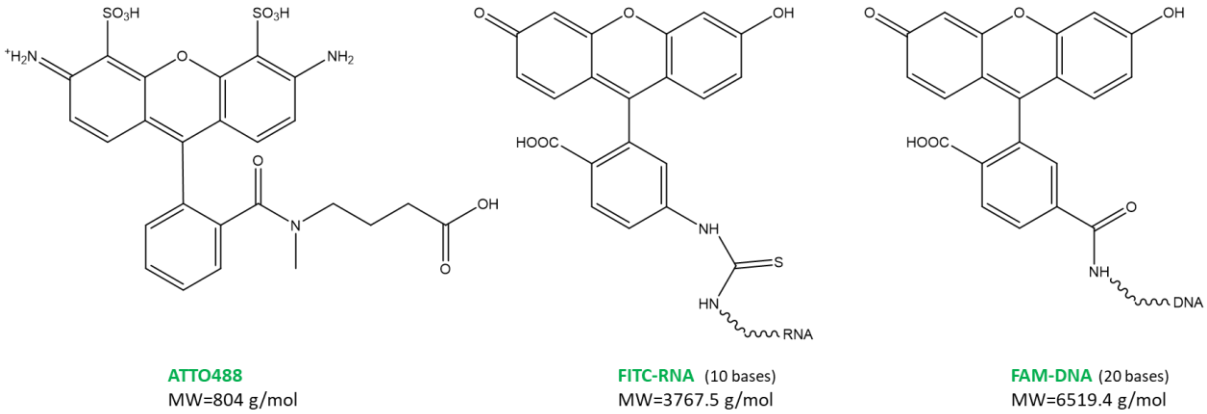

Figure 16: The structures and molecular weights of the three fluorophores that were used in the experiments. The chemical structures of RNA and DNA are not shown, but their weights are included.

3.5.2 Confocal microscopy

Confocal microscopy is essentially the same as fluorescence microscopy, but with the ability of sectioning the sample in different layers. Confocal microscopes have two pinholes in the light path, one in front of the light source, and another in front of the detector. The former limits the excitation laser to a defined focal plane of the sample, while the latter prevents the fluorescence from other planes other than that same focal plane to reach the detector [67]. An illustration on how the detector pinhole works is shown in **Figure 17**. Only fluorescence from molecules in the focal plane can go through the pinhole and be detected. The fluorescence coming from a point above the focal plane reaches the objective lens with an incident angle that makes it refract to a spot outside the pinhole, filtering it out. This also applies to any fluorescence located below the focal plane. The thickness of the section increases by increasing the size of the pinholes. Sectioning of the sample in multiple layers, makes it possible to construct 3D images with high resolution, by simply combining the scans from different sections.

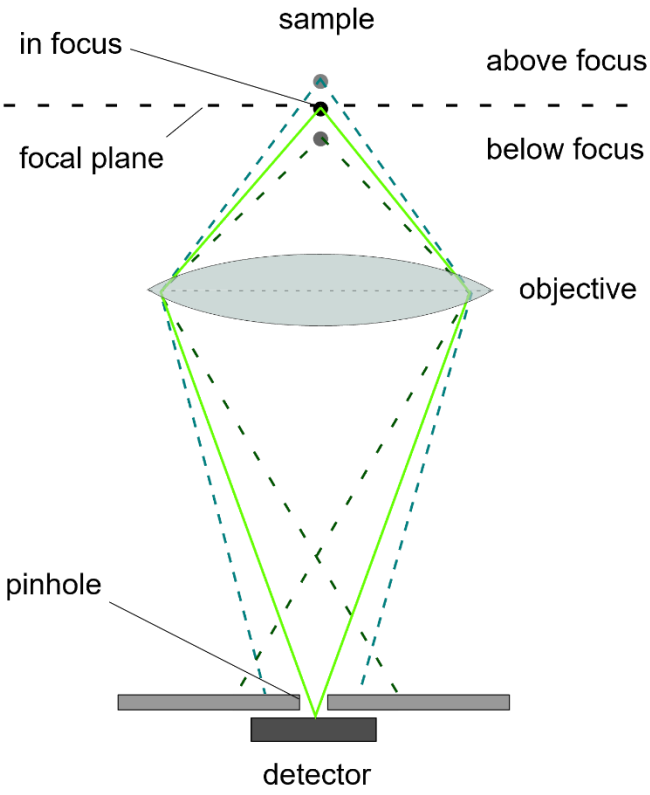

Figure 17: The confocal pinhole allows only light from the focal plane to reach the detector.

3.5.3 Differential interference contrast (DIC) microscopy

Differential interference contrast (DIC) is a diascopic wide-field microscopy technique that is suitable for imaging transparent specimen. DIC is based on the phase shift that occurs when light travels through the sample, which has a refractive index higher than air. As seen in **Figure 18** the phase shift depends on the length that the light must travel through before exiting the medium, i.e., specimen thickness.

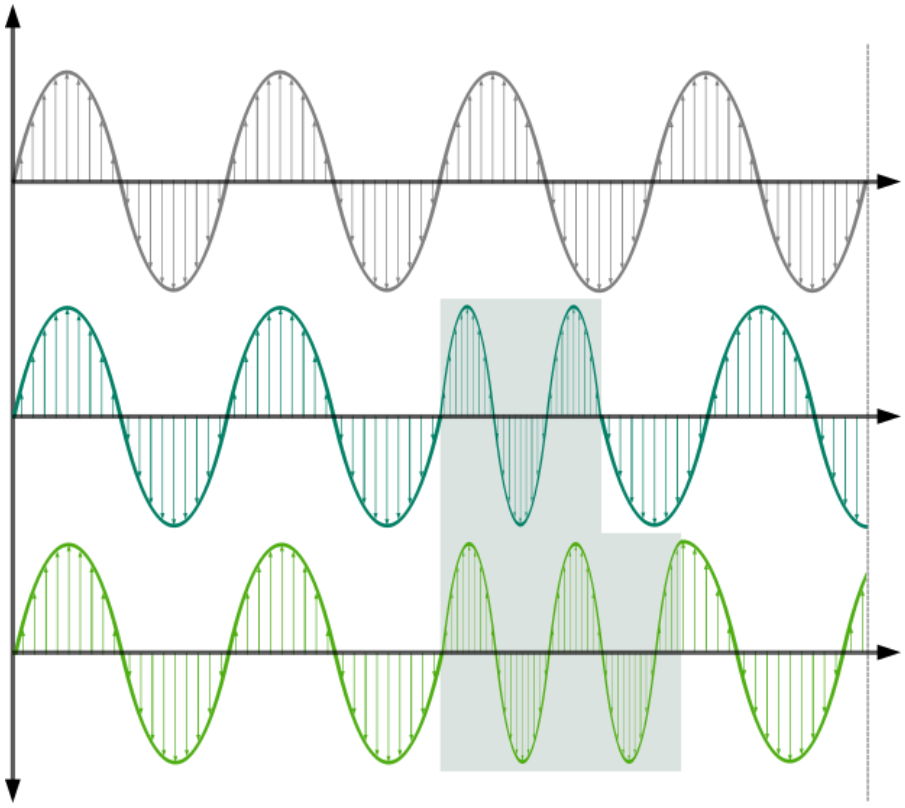

Figure 18: Going through a medium (in grey) with another refractive index and varying thickness results in phase shift.

Figure 19 is a schematic of how the light is processed in DIC microscopy. The light is first sent through a polarizer, which only allows 45º polarized light to pass. Next, it goes through the Wollaston prism which consists of two segments of birefringent material, through which, the polarized light is split into two perpendicular rays of 0º and 90º. These rays are refracted away from each other because they have different polarization. Upon going through the condenser, the two rays proceed as close parallel rays before reaching the sample. When the light rays reach the specimen, which has a higher refractive index than air, the speed of the light will slow down, and the wavelengths become compressed. Once the light exits the specimen, it recovers its previous speed and wavelength. Depending on the distance in the sample the light rays has traveled, a certain phase shift occurs. Different refractive indices within the specimen will also contribute to phase shifts. After exiting the sample, the light rays are then combined in another Wollaston prism, where they interfere. According to the interference between the rays, brightness or darkness is added to the intensities of the image, producing contrast. The light then passes through a 135º polarizer

termed the analyzer, which filters out the light ray pairs that did not experience phase shift [68]. Resulting transparent samples, e.g., unilamellar vesicles, typically have a 3D appearance.

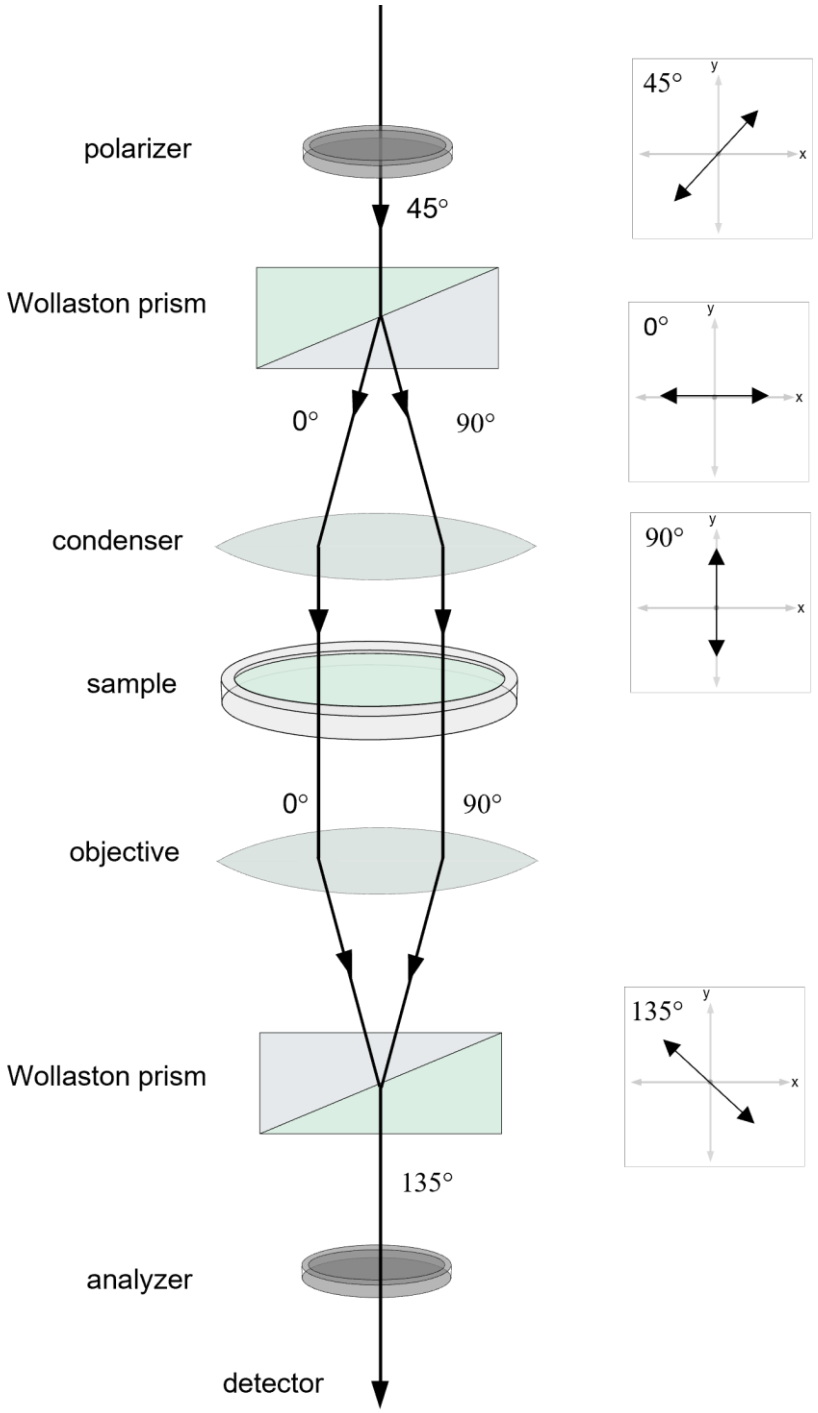

Figure 19: Schematic drawing showing the light path in DIC microscopy.

3.6 The open-space microfluidic pipette

Microfluidic pipette is an open space microfluidic device (Fluicell, Sweden) made of the flexible elastomer (PDMS). As seen in **Figure 20a**, it has a total of eight wells; the 4 front wells are filled with the fluids that are to be superfused with surface-adhered objects, while waste is collected at the four back wells. The wells are connected to the three channels on the tip of the pipette (**Fig. 20b**). The center channel is flushing the solution from a chosen front well, while the two outer channels are aspirating both the content that is released from the pipette and the ambient buffer, collecting everything at the back wells. The continuous inflow and outflow of buffers creates a recirculation zone at the tip. The controlled volume of solution in the recirculation zone is exposed to the object of interest on the solid substrate, e.g., a biological cell, and does not mix with the ambient buffer due to low diffusion [69, 70]. The flow going in and out of these channels is controlled by pressure (**Fig. 20c**), which can be adjusted to alter the shape and size of the recirculation zone.

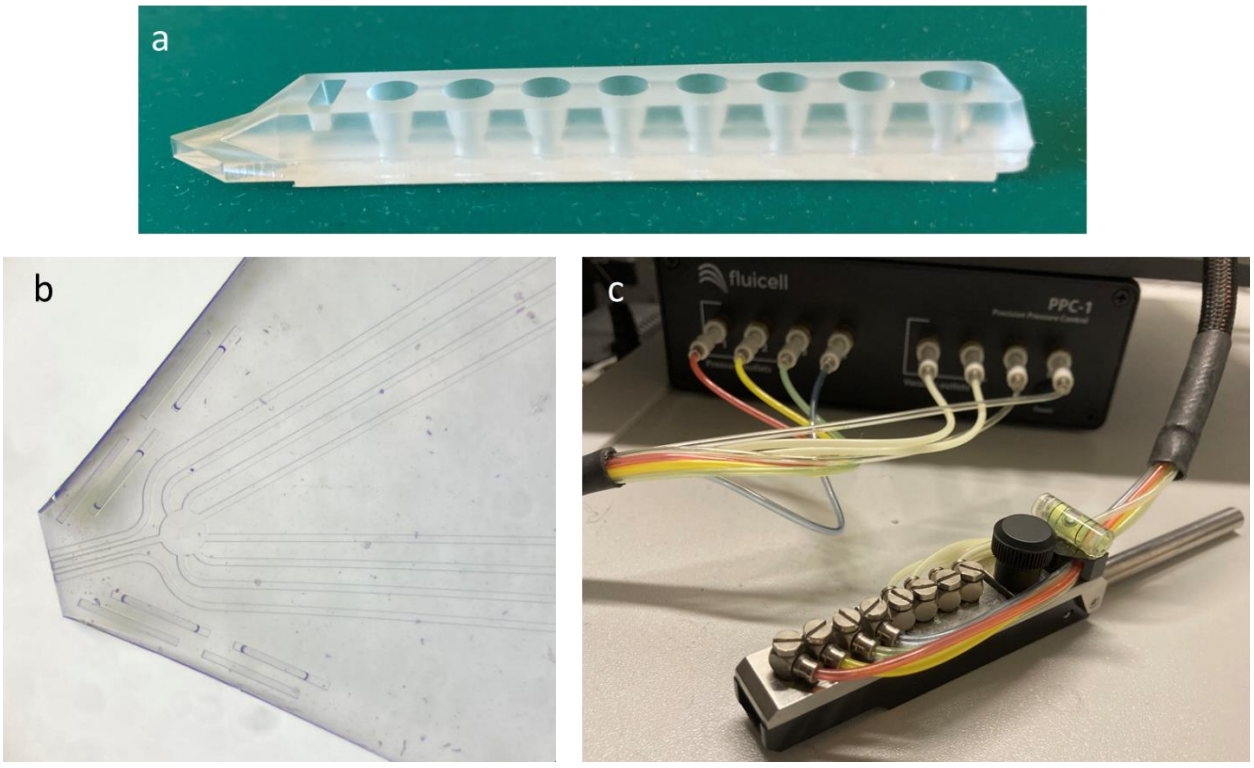

Figure 20: Microfluidic pipette. Photograph of (a) the microfluidic pipette containing eight wells, (b) the tip of the pipette, under a stereo microscope, (c) the microfluidic pipette holder, the pneumatic pump and tubing connecting the two units.

The microfluidic pipette was used to introduce the fluorescent compounds to the protocell-nanotube network. **Figure 21** illustrates of the microfluidic pipette delivering content to the local area.

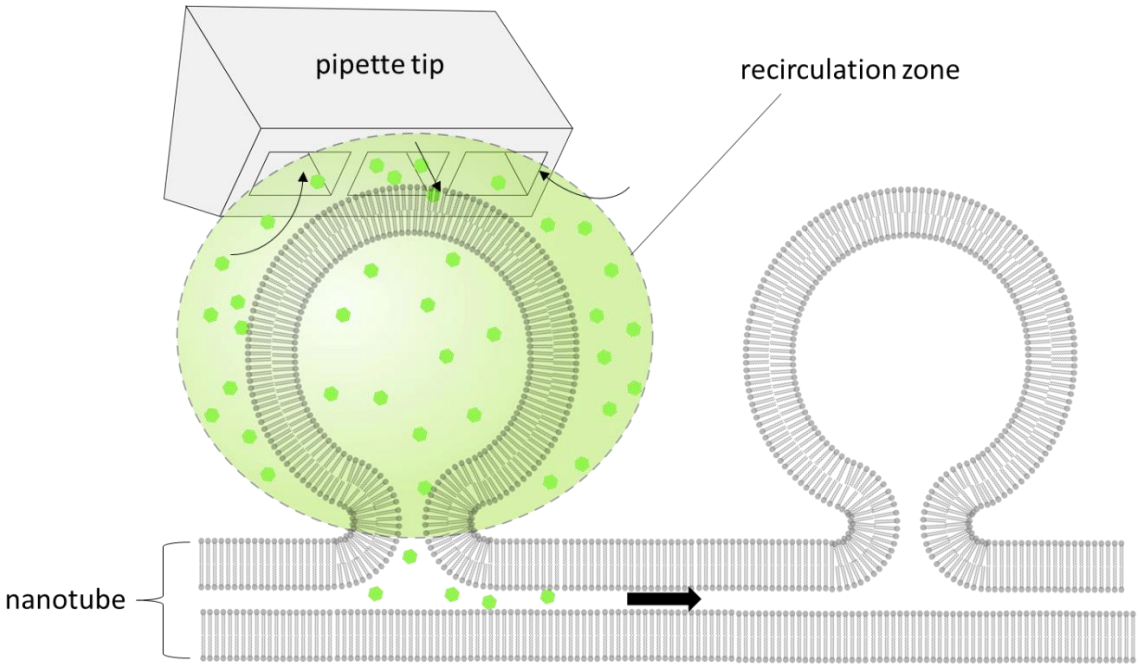

Figure 21: Microfluidic pipette creates a local recirculation zone in which selected vesicles can take up the content.

In order to encapsulate the fluorophores inside the vesicles of PNNs, the selected well was filled with 30 µl of the fluorescence solution (500 µM ATTO488 and 200 µM FAM-DNA). Because the RNA is very unstable, sterilized pipette tips were used to add nuclease-free water to dilute FITC-RNA to 100 µM.

3.7 Fluorescence recovery after photobleaching (FRAP) analyses

Fluorescence recovery after photobleaching (FRAP) is a popular fluorescence technique to study membrane dynamics and diffusion properties. By exposing a fluorophore to high energy laser, one can induce a structural change in the molecule and permanently shut off its fluorescence capability i.e., the molecule becomes photobleached. There are three stages in a FRAP experiment (**Figure**

22): the period which is recorded prior to the bleaching (**Fig. 22a**), the time when the actual photobleaching transpires (**Fig. 22b**), and the post-bleach time where the fluorescence recovery is measured (**Fig. 22c**). **Figure 22** illustrates that when a fluorescently labeled membrane is photobleached in a small area, that area will recover. This occurs due to the lipid's lateral diffusion. In a 2D fluid membrane, the lipids with functioning fluorophores mix with the photobleached lipids and as a result, the initially photobleached area becomes fluorescent again. The recovery can be observed when fluorescence intensity in the region of interest is plotted over time (**Fig. 22d**). The time it takes for fluorescence to recover is directly related to the mobility of the lipid within the membrane. Similarly, if the fluorescently labeled content of a vesicle in a protocell-nanotube network recovers after it have been photobleached, this would indicate that through the molecular diffusion of fluorescent tracers inside the network to the photobleached vesicle (**Fig. 22e**).

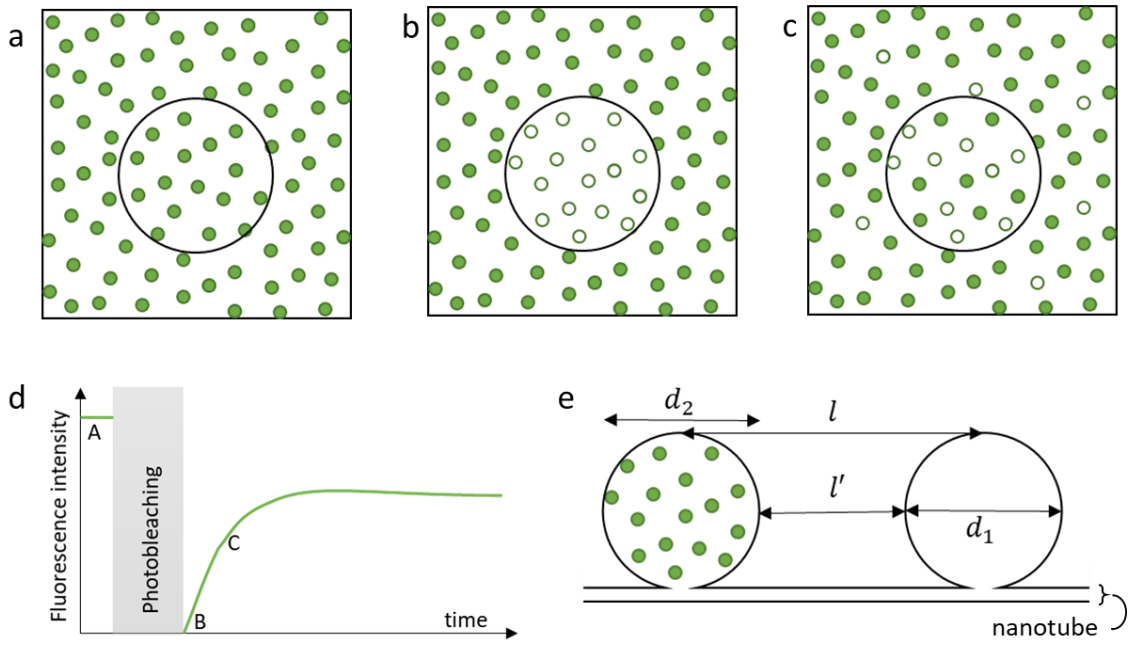

Figure 22: Illustration of the FRAP process. (a) pre-bleaching period, (b) right after photobleaching, and (c) during recovery (post-bleach). (d) Fluorescence intensity of the circular ROI in (a-c) as a function of time. (d) Diffusion of molecules between vesicles in a PNN happens through nanotubes.

Transport in lipid nanotubes can be driven by three main mechanisms [35]: diffusive motion [41], tension-driven transport (Marangoni effect) [58, 71], and electrophoretic transport [72]. Diffusive motion is driven by concentration differences. The diffusion direction of molecules is down the concentration gradient, i.e., the molecules will move from high to low concentration until the

gradient disappears. The rate of the diffusion is not constant and is determined by the gradient which is also changing over time.

Fig. 22e shows a 2-vesicle system, with one vesicle containing molecules of same type, and the other free of these molecules. The two vesicles are connected by a single nanotube. If the transportation of the molecules is only governed by molecular diffusion, the concentration difference will decay exponentially with $e^{-t/\tau_{relax}}$. The relaxation time, τ_{relax}, is given by **Equation 12** [73]:

$$\tau_{relax} = \frac{V_1 V_2}{V_1 + V_2} \frac{l}{\pi r^2 D} \qquad 12$$

where V_1 and V_2 are the volumes of the empty vesicle and the neighboring vesicle, respectively. The diffusion coefficient D, is distinct for each molecule, while r and l are the radius and length of the nanotube. If $V = \frac{\pi}{6} d^3$ and the standard length, $l = l' + \frac{d_1 + d_2}{2}$, where l' is the distance between the two vesicles, **Eq. 12** can be written as **Equation 13**:

$$\tau_{relax} = \frac{d_1^3 d_2^3}{d_1^3 + d_2^3} \frac{l' + \frac{d_1 + d_2}{2}}{6 r^2 D} \qquad 13$$

The above equation assumes that the nanotube is straight, and that it connects two spherical vesicles with the connection point being at the bottom and normal to the center of the vesicles. An important thing to mention is that in the FRAP experiments performed in this thesis, the photo-bleached vesicle is not only filled with buffer free of fluorescent molecules, but contains molecules such as RNA, where the fluorophore initially attached to it has been photobleached. In principle, the presence of molecules might affect the trafficking and influence the diffusion.

A theoretical curve can be fitted to the fluorescence recovery of a photobleached vesicle by using the relaxation time and plotting **Equation 14** [74]:

$$F(t) = F_{max}\left(1 - e^{-\frac{t}{\tau_{relax}}}\right) \qquad 14$$

with F_{max} as the maximum fluorescence recovery. The relaxation time is the time it would take for the system to reach equilibrium if the diffusion rate stayed the same as the initial diffusion rate, i.e., if the diffusion rate is constant, and the recovery is linear. The relaxation time is a time constant obtained from **Eq. 13**, and should not be confused with the recovery time.

Theoretical curves were fitted to the recovery graphs with **Eq. 14** and the relaxation time in **Eq. 13**, by changing the variables in **Eq. 13** [Section 4.2].

Figures, plots, and image editing

Most illustrations were made with Inkscape and PowerPoint, and chemical structures were created with ChemDraw. Microscopy images were edited (cropping and false coloring of gray scale images) in the Leica Application Suite X (LAS X) software or Nikon's NIS-Elements AR Analysis. The FRAP curves were plotted in MATLAB R2020b. Illustrations, plots and images were combined to figures using PowerPoint.

4 Result and discussion

In this project, the aim is to investigate if and how the material transport and communication among the compartments in a lipid protocell-nanotube network, occurs. The idea is to encapsulate fluorescently labeled molecules inside the compartments and visualize their behavior and possible transport with fluorescence microscopy.

The first step of our experimental approach is to make the PNNs without fluorescent labels to eliminate the risk of interference issues between membrane and cargo dyes. This ensures that the encapsulated fluorophore-conjugated molecules would be the only dye in the system. Since the previous work involved the fluorophore-conjugated lipids in order to visualize the PNNs with fluorescence microscopy, it was not known whether the molecular structure and features of the dyes played any role in the formation mechanism, and whether the PNNs would consistently form from unlabeled lipids [37]. The first step, the results of which are presented in 2.1, therefore help to affirm the formation of the network in the absence of fluorescently labeled lipids.

4.1 Formation of unlabeled protocell-nanotube networks

Unlabeled lipids do not contain any fluorophores and can therefore not be detected with fluorescence microscopy. For reference, a sample which contain a membrane label e.g., rhodamine have been shown in **Figure 23** after 48 hours of maturation. The membrane consists of soybean and E. coli lipids (49:50 wt%).

With fluorescence microscopy, one can readily observe various membrane structures: The round, very bright fluorescent regions represent the MLVs (big arrow in **Fig. 23a**), and the circles with a distinct fluorescence rim are the unilamellar protocell compartments (small arrow in **Fig. 23a**). The double bilayer membranes originating from different MLVs in the sample, cover the entire solid substrate over time. The boundaries of double and single bilayer membranes are visible in fluorescence microscopy in **Fig. 23b** (arrows). The fluorescently bright, thin, lengthy threads appearing in single bilayer regions are the lipid nanotubes (arrows in **Fig. 23c**) In in **Fig. 23a**, the

scanned section is further up from the surface than in the other two micrographs (**Fig. 23b -23c**), therefore the nanotubes underneath the protocells appear blurry.

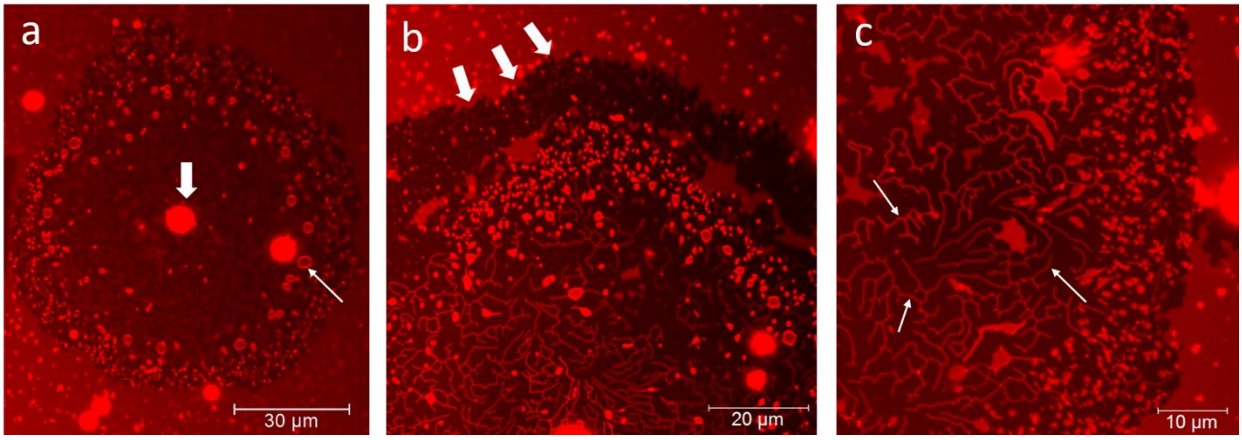

Figure 23: Confocal micrographs of a Rhod PE containing (1 wt%) protocell-nanotube networks, taken with a 40x objective (NA=1.3). (a) Membrane rupture creates nanotubes and protocells following the circular pattern of a lipid patch around an MLV (big arrow). The small arrow points at the largest protocell. (b) The boundary between the double bilayer (bright red) and the single bilayer (dark red) regions. (c) Some small patches of distal membrane (arrows) among the nanotubes on top of the proximal bilayer after rupturing.

Until now, we have shown and discussed only the fluorescence micrographs of the PNNs. In **Figure 24**, the fluorescence images and their corresponding DIC images of the labeled samples of nanotubes and PNNs, are shown. The membranes this time contain 99% soybean lipids and 1% Rhodamine B-conjugated PE. Here, a side-by-side comparison of the fluorescence mode (**Fig. 24a**) and DIC mode (**Fig. 24b**) of a MLV (white arrows) demonstrates the unique characteristics of the two techniques: The abundance of rhodamine-conjugated lipids in one location as opposed to other regions in the sample, indicates high concentration of lipid material in those regions, i.e. the MLV. The fluorescence intensity of the nanotubes and unilamellar compartments located on the surface supported lipid bilayer (dark red color) provides high contrast and can be easily visualized (**Fig. 24a** and **24c**). On the other hand, in DIC mode the MLV, the nanotubes and the model protocells appear as 3D objects (**Fig. 24b** and **24d**).

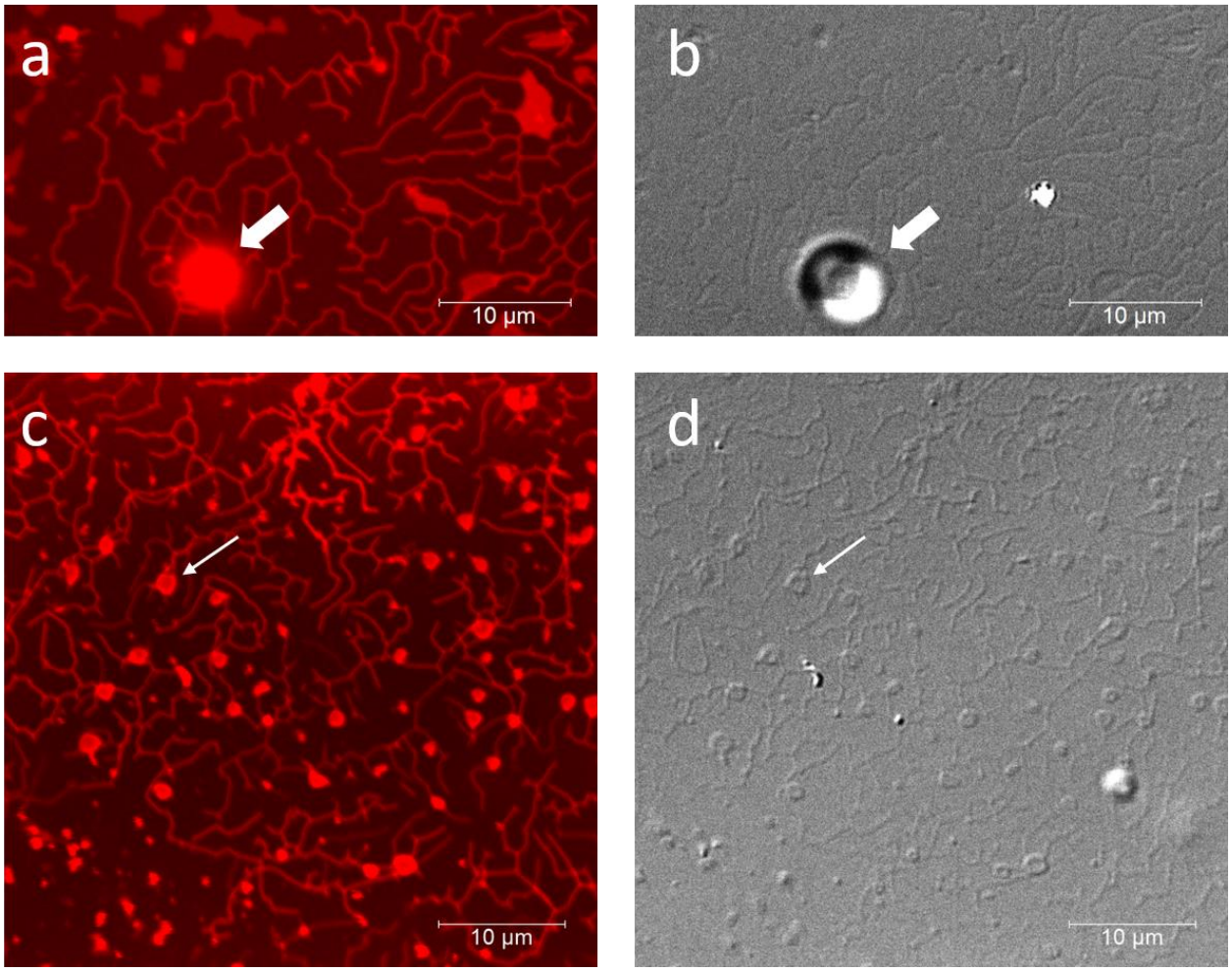

Figure 24: Fluorescence and DIC microscopy images of a labeled SPL (100 wt%) protocell-nanotube networks. The white arrows in the fluorescence images (a, c) points to the identical structures in the DIC images (b, d).

Figure 25 shows the DIC images of two unlabeled samples. The localization pattern of vesicles in a lipid patch, originating from a MLV (big arrow in **Fig. 23a**), is a recognizable characteristic of many PNNs. This pattern can be observed in **Fig. 25a**. The boundary of the circular lipid patch is indicated with white dashed line. Nanotubes and the nucleating compartments from them can also be visualized in unlabeled samples; an example is shown in **Fig. 25b**.

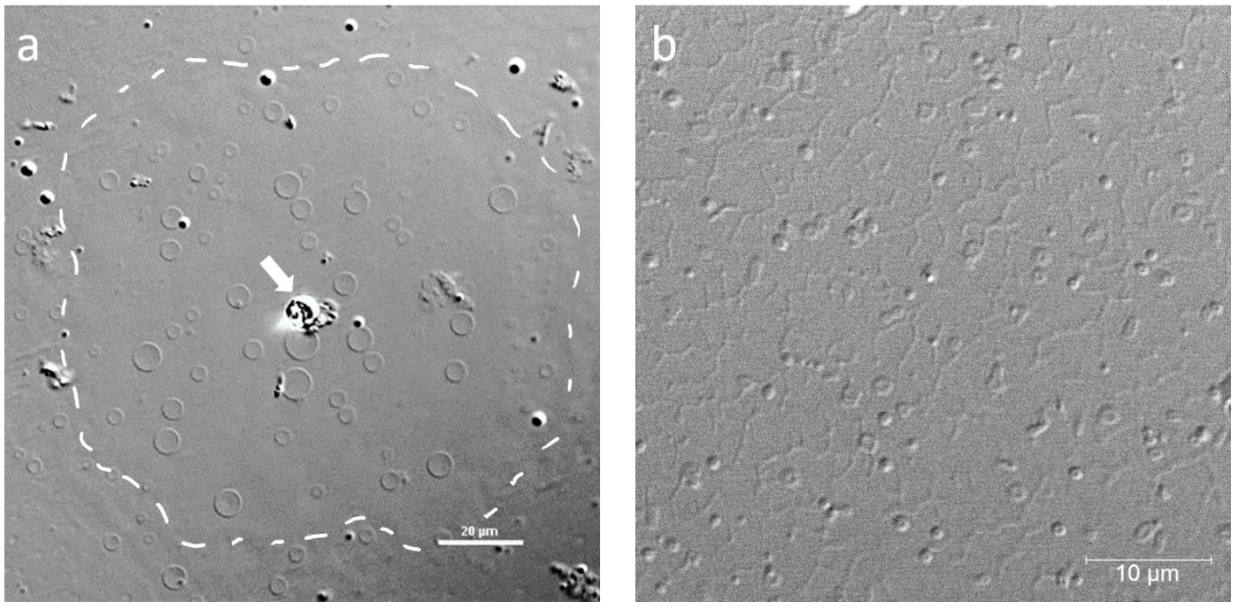

Figure 25: DIC images of protocell-nanotube network of unlabeled lipids. (a) Protocell compartments made from SPL-EPL (50:50 wt%). White arrow shows the MLV, and white dashed line, the contour of the lipid patch. The image was taken with a 40x objective (NA=0,95) with a Nikon Eclipse Ti2 microscope. (b) Protocell compartments and nanotubes made from SPL (100 wt%). The image was taken with the 40x objective (NA=1.3) Leica confocal microscope.

In conclusion, although the protocell-nanotube networks are significantly easier to locate in the fluorescence mode, they can also be detected and visualized in the DIC mode without the requirement of a membrane label. The results also confirm that the presence of the lipid-conjugated fluorophores does not play a key role in the PNN formation. All experiments from this point forward were executed solely on unlabeled PNNs with SPL-EPL (50:50 wt%) lipid composition.

4.2 Encapsulation of fluorophores by the PNN

Following the formation of the PNNs from unlabeled lipids, next step was to encapsulate the fluorescent components inside the networks. We used a microfluidic device [69, 70] to expose the model protocells to the different compounds. Briefly, we focused on a surface region of interest (ROI) containing multiple model protocells, and with the microfluidic pipette, exposed the compounds to the protocells in the ROI. It was recently shown that the surface-adhered protocell compartments were able to take up the molecules by means of molecular diffusion through nano-sized transient pores in the membrane [75, 76].

4.2.1 Fluorophore size and encapsulation yield

The three fluorescently labeled cargo components were employed: water soluble ATTO-488 dye, FITC-conjugated RNA and FAM-conjugated RNA. Fluorescein dye results in a high encapsulation yield [37] i.e. gets encapsulated in relatively higher number of vesicles in the same amount of time, but it instantly leaks from the compartments. The rapid leakage is a problem as the aim is to monitor the transport of the molecule inside the network for a long time. The simple water-soluble dye, ATTO488-carboxy, maintains in the system for a longer duration than Fluorescein and was therefore chosen for the experiment.

FITC and FAM are popular choices for fluorophore-conjugated oligonucleotides, and were used as labels for RNA and DNA, respectively. These compounds were exposed to PNNs for 4-5 minutes and the encapsulation results are shown in **Figure 26**. During the superfusion (**Fig. 26a, c, e**) the protocells appear as black circular regions inside the superfusion zone, because either there is no uptake of the compounds from the surrounding medium, or the protocells have encapsulated a relatively lower concentration of compounds than in the superfusion zone (green). Upon termination of superfusion, the buffer from the microfluidic pipette containing the fluorescently labeled molecules is replaced with the ambient buffer that is free of fluorophores. The protocells containing the encapsulated fluorophores become visible (green signal) (**Fig. 26b, d, f**).

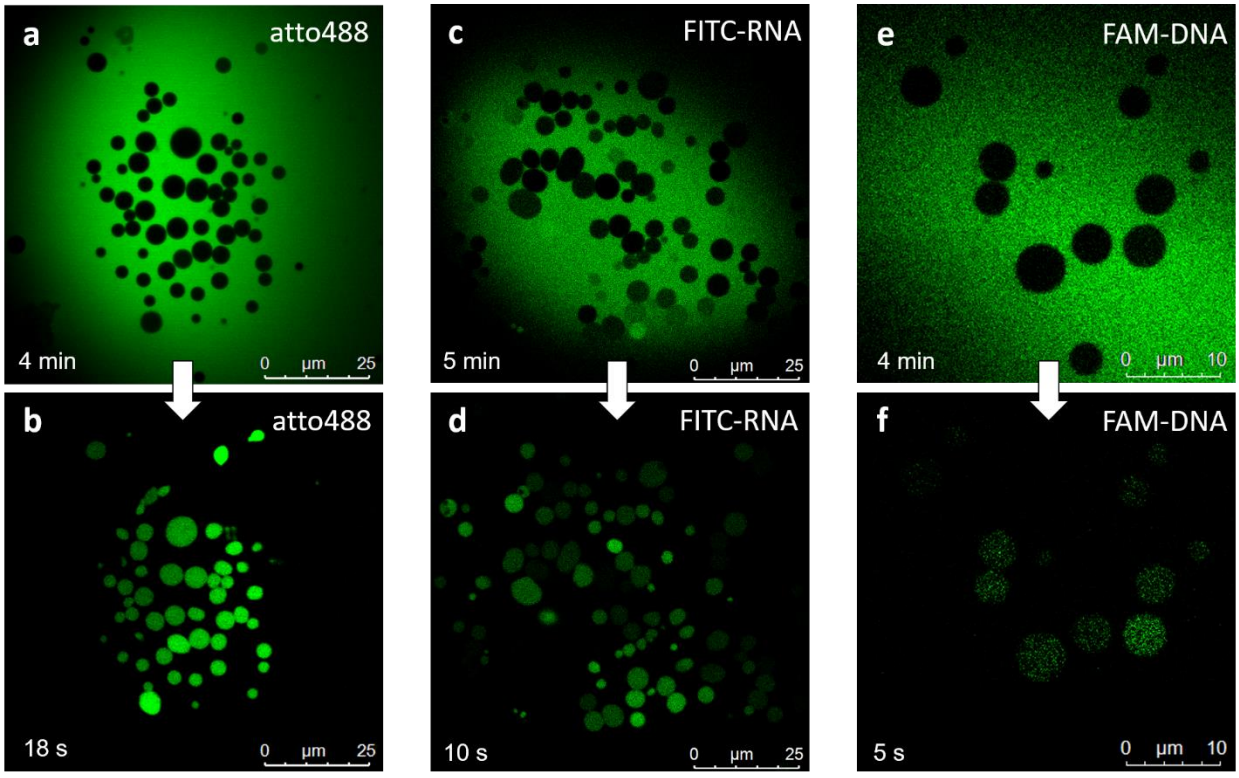

Figure 26: Encapsulation of different labeled compounds. (a-b) ATTO, (c-d) FITC-RNA and (e-f) FAM-DNA. (a, c, e) superfusion of protocells with labeled compounds. The time is the duration of the exposure. (b, d, f) snapshots of the protocells, s after the superfusion is terminated.

In general, the ATTO488-exposed PNNs appear to have a high fluorescence intensity, indicating efficient encapsulation (**Fig. 26b**). FITC-RNA (**Fig. 26d**), and FAM-DNA (**Fig. 26f**) have been also successfully encapsulated by the PNNs. The reason for the different fluorescence intensities inside the vesicular compartments can be due to the size differences of the molecules. The total molecular weight of ATTO-488 with a carboxy modification is 804 g/mol, which is small compared to the dye-conjugated RNA (3767.5 g/mol) and dye-conjugated DNA (6519.4 g/mol), respectively. Due to their relatively larger sizes, the diffusion through the nano-sized openings in the membrane, appears to be more challenging for the genetic fragments (**Fig. 26**). The larger molecules also leak slower through the pores than the simple ATTO488 dye.

4.2.2 3D confocal images reveal the internal structure of the networks

3D images of the samples can be obtained if the individual confocal slices through the sample can be reconstructed. This reconstruction takes several minutes, which is not suitable if dynamic processes are observed, e.g. molecular diffusion of encapsulated compounds. 3D images reveal multiple structural features of the PNNs compared to 2D scans, e.g. structures in x-z plane, height of the model protocells, and the arrangement of nanotubes within the PNN.

We exposed the vesicles to 500 μM of ATTO488 for 4 min. After the encapsulation of the ATTO488, 3D images of the sample were obtained to visualize the content inside the unlabeled network. **Figure 27** shows a top-view of a 3D image. The green fluorescence shows the internal space of the PNN, the encapsulated content of both protocells and nanotubes.

Our concern is not that the nanotubes are filled with a substance or adopt a membrane morphology which is not hollow inside, but that the tubes are pinned at some locations blocking the transport of material. The fact that there is fluorescence inside, does not necessarily verify that they are open because it could be that the fluorescence is entrapped between two blocked points.

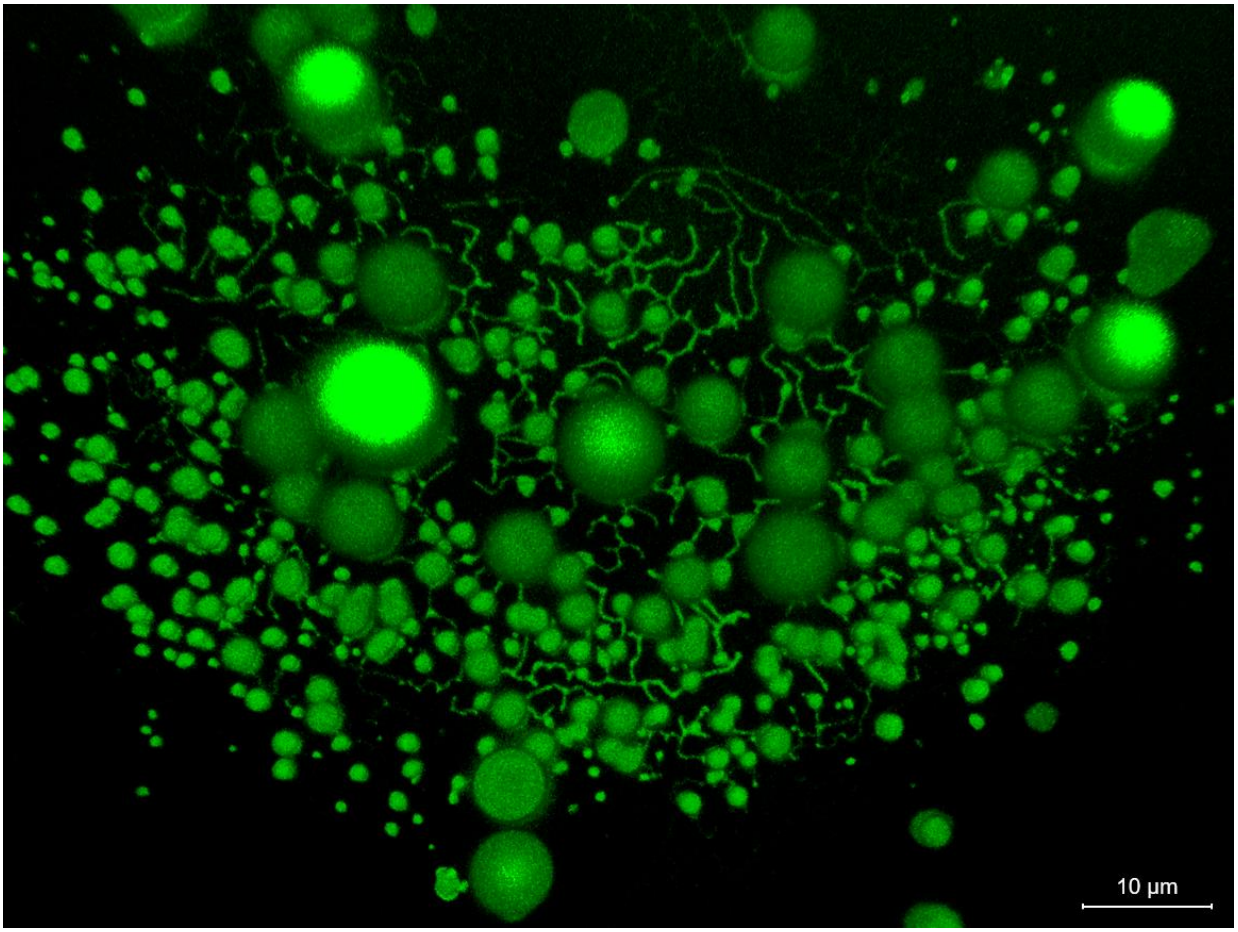

Figure 27: 3D confocal image of ATTO488 inside a protocell-nanotube network with an unlabeled membrane.

The 3D scan gives valuable information about the entire internal morphology of the PNNs. The compartments are slightly elongated, similar to a balloon with a flat bottom, or a dome (**Figure 28**). The nanotubes are aligned between the protocells and mostly not straight, indicating presence of pinning points [59] between the nanotubes and the underlying bilayer. Overall, the 3D images reveals the internal volume inside the membrane boundaries.

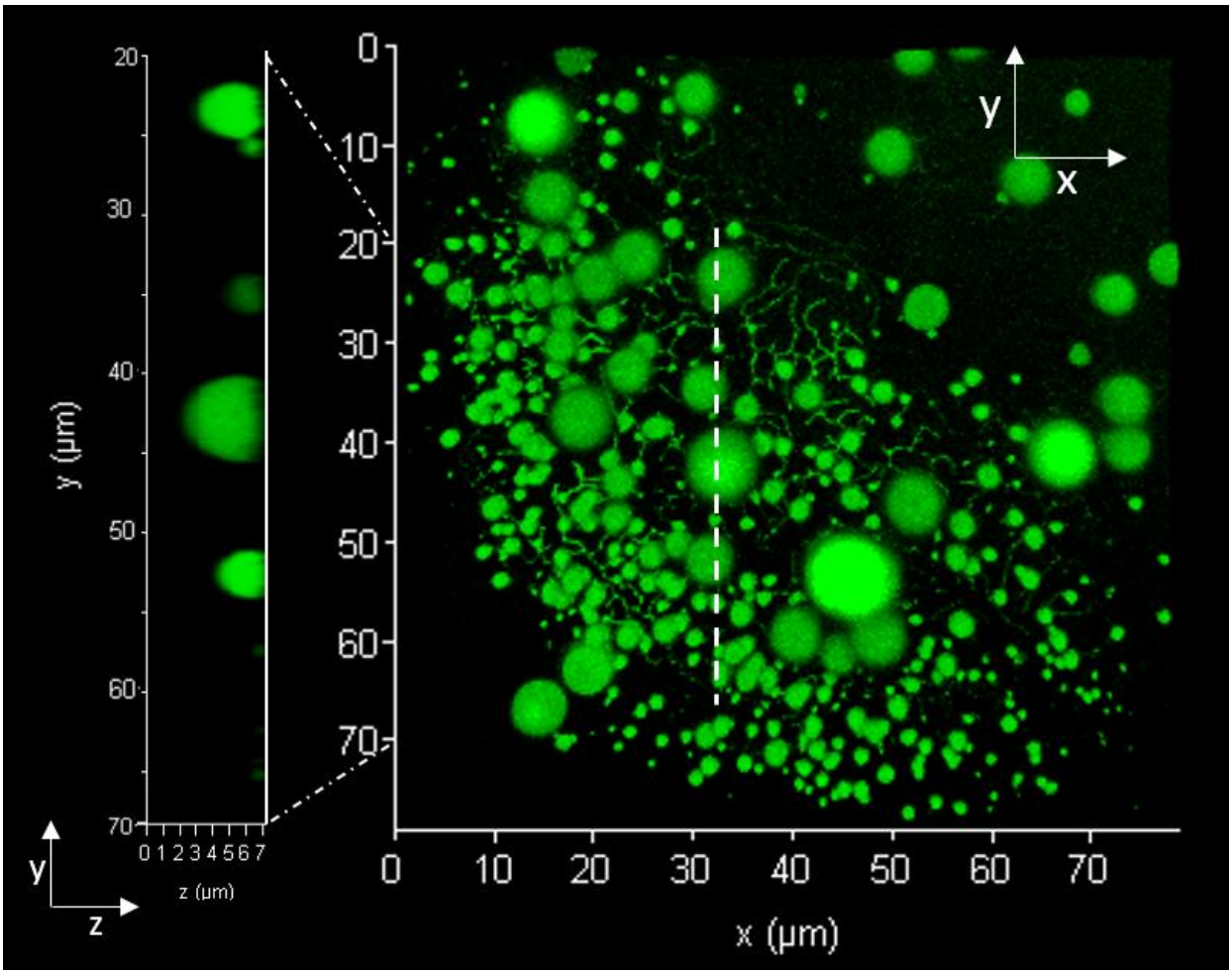

Figure 28: Cross-section of the PNN along the white dashed line in x-z plane. The encapsulated fluorescent content is clearly visible.

4.2.3 Rapid growth and fusion of vesicles

Protocell nucleation and growth occurs slowly. Normally, under room temperature, this process takes many hours and sometimes days. However, the growth can be induced with temperature, and the process can be sped up to minutes [62], as the rise in temperature increases the membrane fluidity, which enhances the Marangoni flow. This is also the reason we waited 3-days after the sample preparation or kept the sample in 35° to speed up the process.

An interesting observation during the encapsulation experiments was the rapid growth of vesicles during the exposure of the protocell compartments to fluorescently labeled compounds. **Figure 29** shows the time-lapse images of the budding and rapid growth of vesicles under FAM-DNA

superfusion. While we were targeting the big vesicles (~10 μm in diameter) in the recirculation zone for possible encapsulation (**Fig. 29a)**, many new vesicles started to appear. The contour of 3 such freshly grown vesicles are indicated with white dashed lines in **Fig. 29b**. In further time points of the experiment, these 3 vesicles fused and merged into one large vesicle (**Fig. 29c**). The material required for the growth was likely provided by the lipid reservoir in the center (arrow in **Fig. 29a**)**. Fig. 29d** shows internalized DNA in a vesicle after the termination of superfusion. However, the fluorescence intensity inside the compartment (arrow in panel d) is low, indicating poor encapsulation.

Similar observations of rapid protocell growth were made for ATTO488 and RNA (not shown), especially when the protocellular compartments were located close to the MLV. Although the investigations regarding the mechanisms underlying this phenomenon is not the scope of this thesis, it is an interesting observation which can be studied as a follow up work in the future.

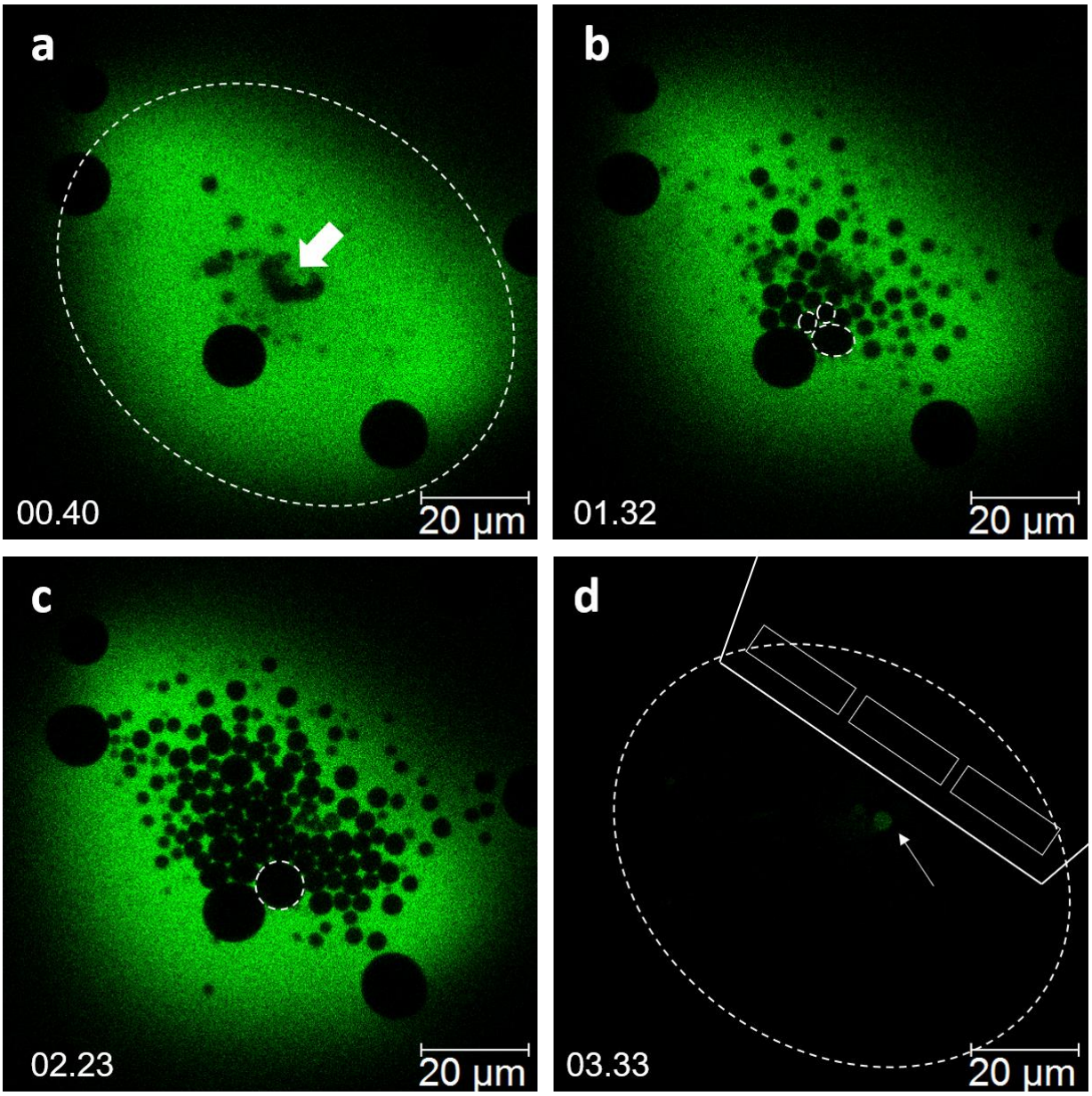

Figure 29: Rapid growth of vesicles during a 3.5 min exposure to DNA encapsulation. (a) dashed line represents the recirculation zone, and the white arrow points at the MLV in the center. (b) new vesicles have emerged, three of the vesicles (in dashed lines) have fused together in (c) as they continue to grow. (d) The arrow points to a vesicle with DNA within the recirculation zone.

4.2.4 Consumption of lipid nanotubes during compartment growth

Lipid compartments stem from nanotubes and retrieve the membrane material required for the growth through them. When the lipid reservoir is accessible, the excess lipid material is used for this transformation, transferred through the tubes over time. In settings where lipid source is scarce, such as when lipid reservoir is depleted or too far away, the nanotube itself is consumed and transformed into a lipid compartment [37]. Under the special conditions mentioned in the previous section, i.e., where the membrane is continuously perturbed due to superfusion, the growth of compartments occurs rapidly. **Figure 30** shows the consumption of nanotubes while compartments rapidly grow during the encapsulation of ATTO488. The figure shows the same region in a PNN. Some of the large vesicles (**Fig. 30a**) disappear while new vesicles emerge (**Fig. 30b**). One newly developed vesicle is marked with a red dashed line.

Fig. 30b and **30d** show the underlying nanotube network, before and after growth. It is clearly visible that, while most of the pinned nanotubes maintain their positions, the nanotubes existing initially underneath the encircled vesicle, have disappeared. This can be due to the fact that the nanotube material is consumed [37], or that the nanotubes are rearranged after vesicle nucleation in that tubular node [77].

Some of the more conspicuous-looking nanotubes in the upper and lower right corners of **Fig. 30b** are recognizable after the growth (**Fig. 30d**), and their position remain same as before. This is likely due to the strong, Ca^{2+}-induced pinning of the tubes to the proximal membrane [37]. Otherwise, the nanotubes are semi or completely suspended and can rearrange in a fashion where the membrane surface free energy is minimal [34, 78].

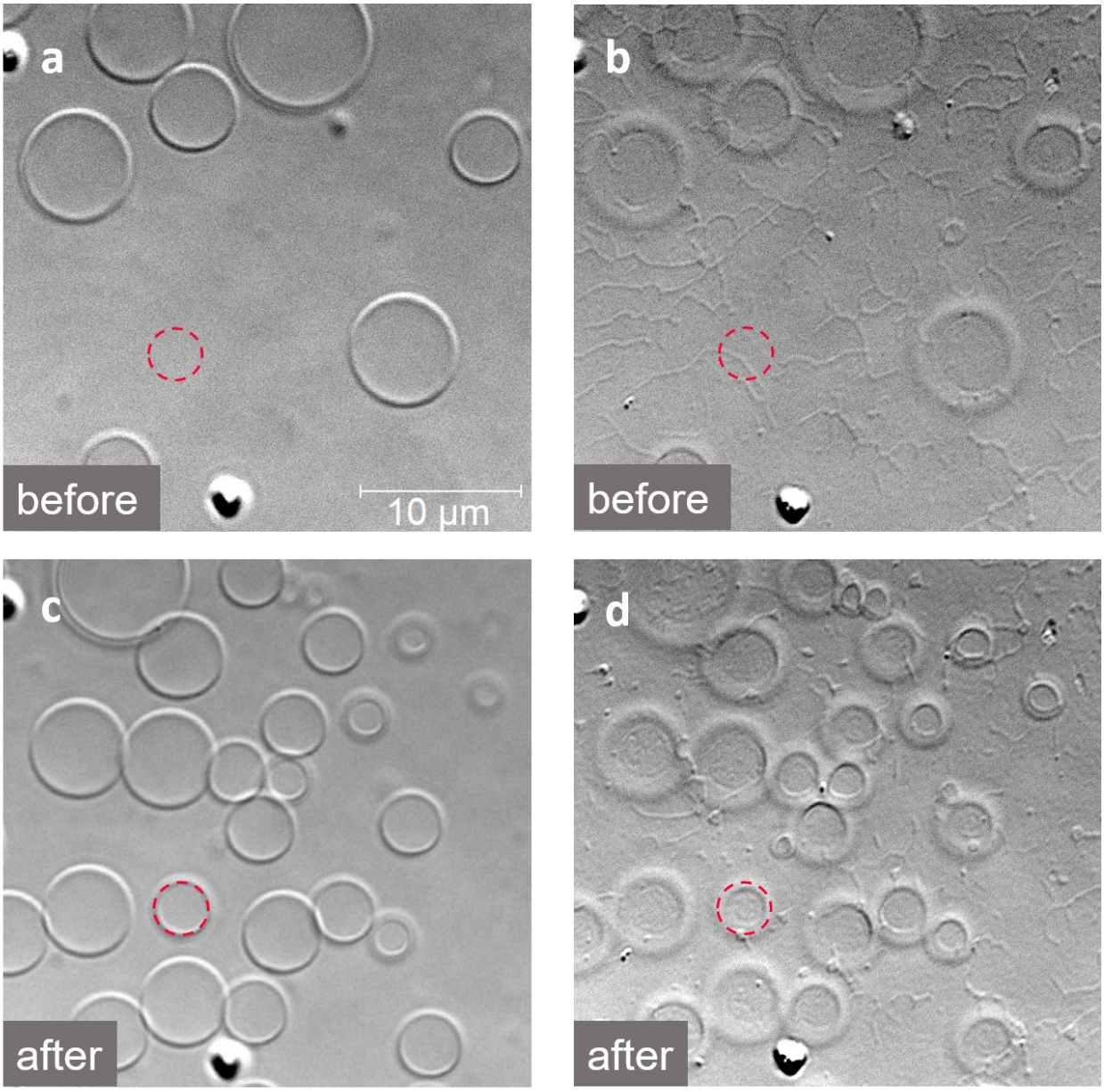

Figure 30: DIC images of a PNN region showing the change of nanotubular network during rapid compartment growth. (a-b) images of vesicles and nanotubes, respectively, before superfusion of ATTO488. (c-d) same area in (a-b) after superfusion. The red dashed circle indicates the position of the emerging vesicle. The time between the before (a-b) and after images (c-d) is 2 hours.

4.1 FRAP experiments and analysis

Following the successful encapsulation of various fluorophores into the vesicles, next step was to investigate whether the nanotubes were continuously hollow, allowing the transport and chemical communication between the vesicles. The trafficking of molecules could not be observed effectively in real time inside the nanotubes with simple time-lapse confocal fluorescence microscopy. Most importantly, monitoring the spreading of the fluorophores through a system with nanotubes branching in all directions over distances of several tens of micrometers, is challenging. Instead, we designed a FRAP experiment, in which a small region with compartments containing fluorescent content is photobleached, and possible recovery is observed. With this approach, the transport can be affirmed easily if there is fluorescence recovery.

4.1.1 Control experiment

A vesicle with no physical connection to other vesicles containing fluorophores should not show recovery after photobleaching. Demonstration of such an isolated vesicle has been shown in **Figure 31**. The vesicle is positioned on a simple glass cover slip. On glass, lipid reservoirs loosely adhere to the surface without spreading [55]. Therefore, no rupturing and nanotube formation follows the initial adhesion, and intact isolated GUVs can be found on the surface instead. **Fig. 31a-d** show the photobleached GUV which initially contains fluorescent cargo, and as expected, fluorescence content of the GUV show no recovery after photobleaching (**Fig. 31e**).

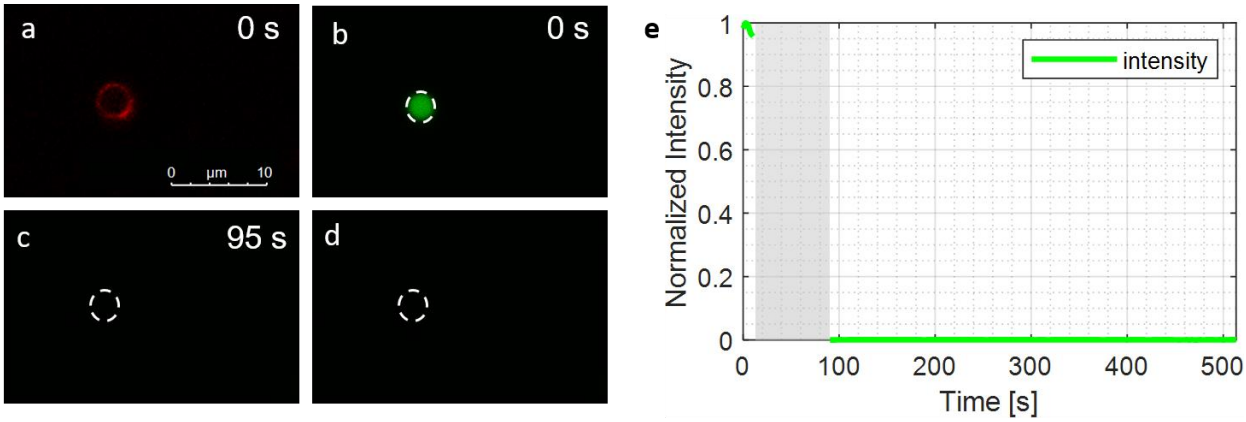

Figure 31: FRAP on an isolated GUV. (a) fluorescence micrograph of a labeled GUV membrane. (b) The ATTO488 encapsulated inside the GUV. (c-d) post-bleach images show no recovery. (e) Graphical presentation of the recovery (nearly zero), normalized to initial fluorescence intensity.

4.1.2 FRAP experiments on PNN vesicles containing ATTO488

This section deals with the FRAP experiments on ATTO488 encapsulating PNNs. Initially, an aqueous medium containing 500 μM of carboxy ATTO488, was exposed to a selected region of PNNs and eventually the dye was encapsulated. Subsequently, one or few vesicles in that region were photobleached. The results of several FRAPs on the networks containing ATTO488 are shown in **Figures 32-35**. In all figures, the vesicle of interest is circled by a red line. FRAP graphs are normalized so that the intensity prior to photobleaching is 100%, or 1, and the first data point after the photobleaching is 0, so the recovery is given as a fraction of the original fluorescence intensity. The number of nanotubes and their connections to the protocells are all unknown. Correction for photobleaching in the FRAP curves was omitted, as there was no way to tell how much fluorescence was due to the laser exposure, leaking of fluorophores through transient pores, or, if the nanotubes are open: diffusion through the network.

The system in **Figure 32** contains multiple vesicles in a PNN, all containing ATTO488. DIC images of this network before encapsulation was previously shown in **Fig. 30**, and it was revealed that the vesicles were growing during superfusion. **Fig. 32a** shows an epi-fluorescence micrograph of the same region (top view) after superfusion, and the vesicle selected for photo-bleaching is indicated with the white arrow. Except for a few, not many nanotubes connecting the vesicles are visible. **Fig. 32b** shows a graph of the measured fluorescence intensity inside the vesicle after photobleaching, and the increased intensity in the plot in the first 50 s. demonstrates that there is recovery.

Recovery can also be observed in **Fig. 32c-e** which are snapshots taken at different time-points during the FRAP experiment. **Fig. 32c** was taken during the pre-bleaching period and **Fig. 32d** right after the photobleaching (t = 0). The vesicle (red circle) is not visible in **Fig. 32d**, because the initially encapsulated fluorophores in it, are permanently shut down due to photobleaching. The return of fluorescence can be observed in **Fig. 32e**, which reveals that the fluorophores fill the vesicle over time. The functioning fluorophores must have come from adjacent vesicles through interconnecting nanotubes that are not visible in fluorescence micrographs. The nanotubes in this network are visible in DIC images, presented in **Fig. 30b** and **Fig. 30d.**

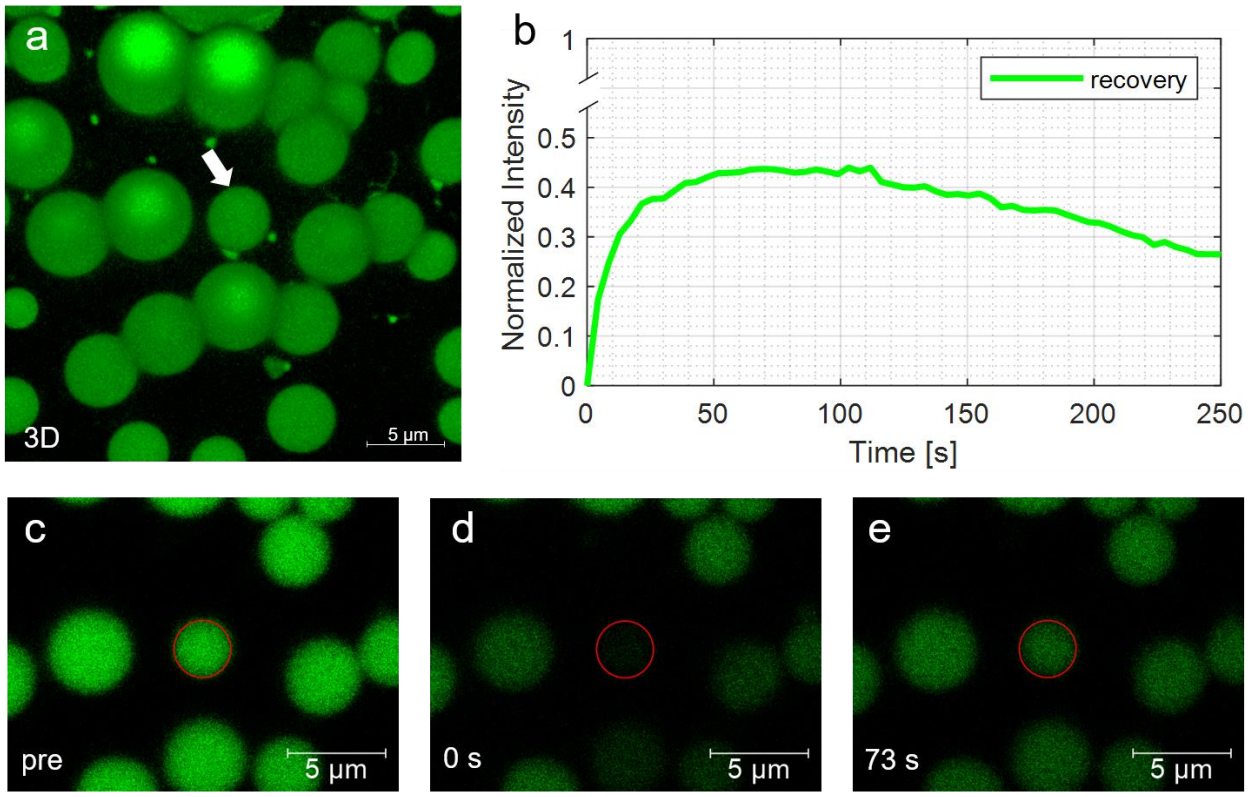

Figure 32: ATTO488 FRAP on a vesicle surrounded by many others. (a) Epi-fluorescence micrograph of a PNN. The white arrow points at the vesicle that is photobleached. (b) Fluorescence intensity (recovery) after photobleaching, vs. time. (c-e) Snapshots of the vesicle of interest (red circle) at different times during the FRAP experiment. (c) pre-bleach, (d) right after photobleaching and (e) during fluorescence recovery.

The photobleached vesicle recovers to 42% of the initial intensity before the photobleaching, in a time span of 70s, before the fluorescence intensity starts decreasing (**Fig. 32b**). The decline can be a result of photobleaching due to laser exposure during the recording, leakage of ATTO488 from the PNNs through transient pores, or, as the FRAP result indicated: molecular diffusion towards the remote parts of the network.

The vesicles in **Fig. 32c-e** that are adjacent to the photobleached one, do also show signs of photobleaching and recovery. This indicates that the transport of fluorophores from the parts of the PNN outside, to the vesicles in the region shown in Fig. 32c-e, is occurring. The fact that the adjacent vesicles also lose fluorescence intensity during photobleaching, might explain why the recovery is low (42%).

The presence of many close-by (with a distance smaller than 5 μm), connected compartments that contain fluorescent cargo, such as the ones shown in **Fig. 32**, seems to be ideal for rapid recovery. The next ATTO488 FRAP experiment was done on a vesicle with fewer neighbor vesicles as seen in **Figure 33**. The targeted vesicle (red circle) has only two compartments within a 5 μm radius, and they appear to be fused (white arrow in **Fig. 33a**). The photobleached vesicle in **Fig. 33b** have recovered some fluorescence in **Fig. 33c**, and the vesicle in recovery is plotted in **Fig. 33d**. The recovery time starting from the end of the bleaching, until the recovery curve reaches a plateau, is 8 minutes (**Fig. 33d**) which is eight times longer than the time shown in **Fig. 32b**.

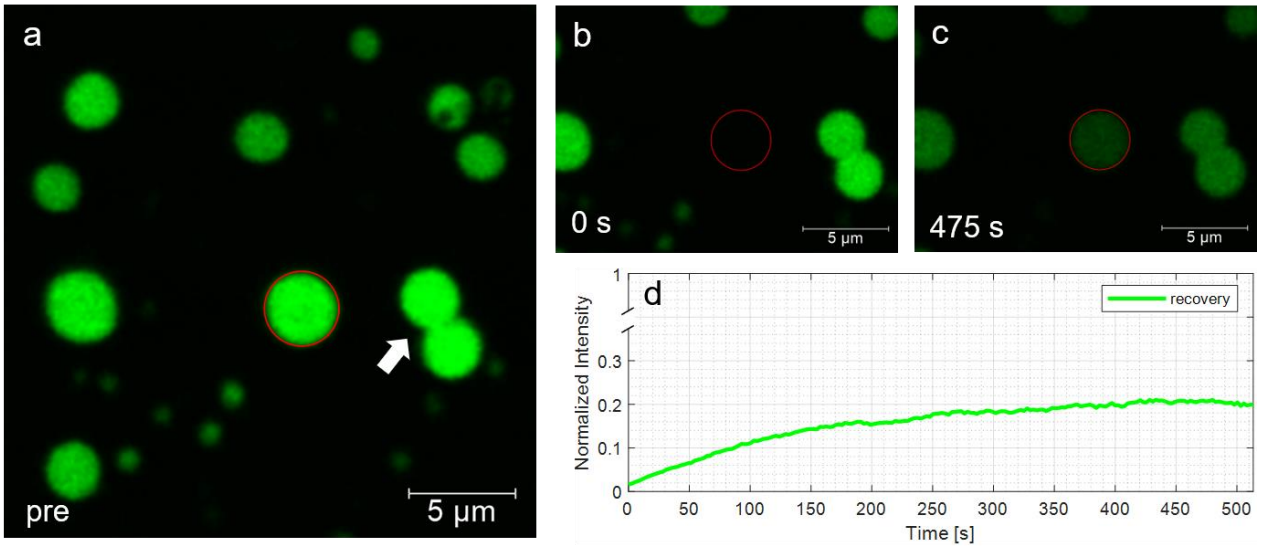

Figure 33: ATTO488 FRAP on a vesicle with a greater distance to others show slower recovery. (a-c) The vesicle (in red) is photobleached and eventually recovers. (d) FRAP graph of the recovery.

Results of a third ATTO488 FRAP experiment is shown in **Figure 34**, and is similar to the one in **Fig. 33**, where the photobleached vesicle has one compartment within a distance of 5 μm (arrow in **Fig. 34a**), while the other vesicles are further away. **Fig. 34b** and **Fig. 34c** reveal the diffusion of fluorophores to the photobleached vesicle. The plot in **Fig. 34d** displays a 25% recovery of the initial fluorescence which took around 4 minutes. This recovery time is twice as fast as the 20% recovery of the vesicle in the previous figure (**Fig. 33d**). The time disparity suggests that the photobleached vesicle in **Fig. 33a** may not be connected to the nearest vesicles (white arrow), but to a more distant compartment.

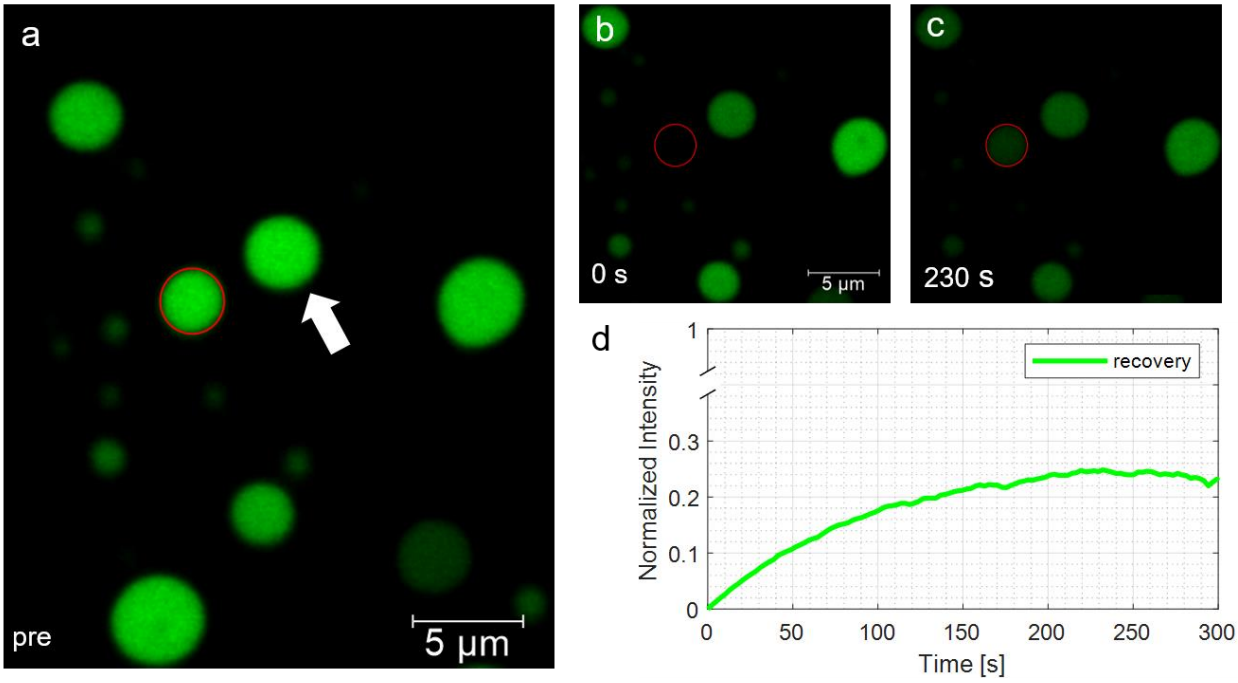

Figure 34: FRAP of a vesicle containing ATTO488. (a-c) snapshots of the pre-bleached bleached and post-bleached vesicle, respectively. (d) fluorescence recovery over time.

The fourth experiment is shown in **Figure 35**. The pre-bleach fluorescence image (**Fig. 35a**) shows which vesicle had encapsulated the ATTO488. This time a DIC image was taken after the FRAP, showing the silhouettes of nanotubes (white arrows in **Fig. 35b**).

From the DIC image it is unclear whether the vesicle encircled in a red dashed line is connected to the nearby vesicles via nanotubular connections. A photobleach (t=0) and recovery image of the vesicle encircled in red is shown in **Fig. 35c-d**. The fluorescence recovery is around 21% in 4 min (**Fig. 35b**), which is comparable to the one in **Fig. 34** (25% in 4 min).

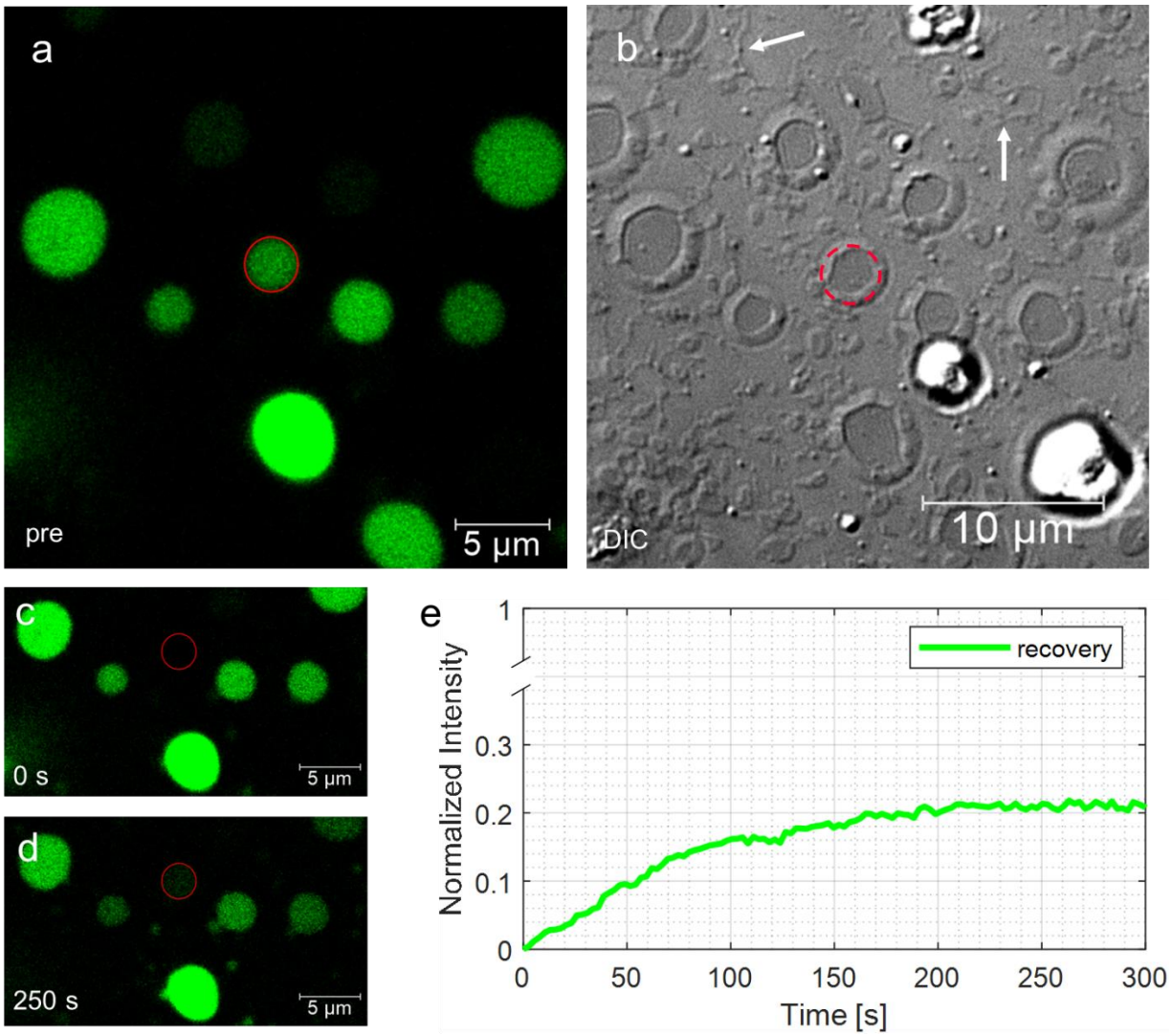

Figure 35: (a) Confocal micrograph and (b) DIC image, of a PNN region. The PNN contains ATTO488 dye. (a-d) shows the FRAP experiment: (a) pre-bleach, (c-d) post-bleach. (e) Graph showing the recovery of fluorescence intensity in the vesicle inside the red circle, over time.

4.1.3 Wave-like spreading of ATTO488 in a PNN

During one of the FRAP recordings a sudden burst of fluorescence from a nearby compartment occurred. The direction of the spreading of the fluorescence material can be seen in **Figure 36**. This is the same network shown in section **4.2.3** Rapid growth and fusion of vesicles (p.48). Due the low uptake of FAM-DNA, this network was exposed to ATTO488 which resulted in successful encapsulation (see **Figure 50** in Appendix). In **Fig. 36a-c**, the loss and return of fluorescence in the photobleached vesicle (red line) is clearly visible. The change in fluorescence intensities after the sudden release of fluorophores from a nearby compartment (white arrow) can be observed in the adjacent vesicles (black arrows and white dashed line) in **Fig. 36d-f**.

The photobleached vesicle (**Fig. 36b**) recovers to 55% in 70 s (**Fig. 36c** and **36g**), before the sudden transfer of fluorescence dye from the compartment shown with the white arrow. Diffusion is observed as a rapid rise in fluorescence intensities in the adjacent vesicles in black arrows in Fig. **36c-d**, followed by the increased intensities in the vesicles encircled in white dashed line in Fig. **36d-e**. A second recovery phase of the initially photobleached vesicle (**Fig. 36e-f**), due to the sudden fluorescence burst and transfer, is reflected in the plot in **Fig. 36g**. According to image in **Fig. 36a**, the vesicle encircled in red line, has no apparent physical connection to the vesicles which suddenly fluoresce. It is plausible that the sudden fluorescence transfer is occurring via the nanotubes between these compartments. As a result, the bleached vesicle recovers 80% of its original intensity.

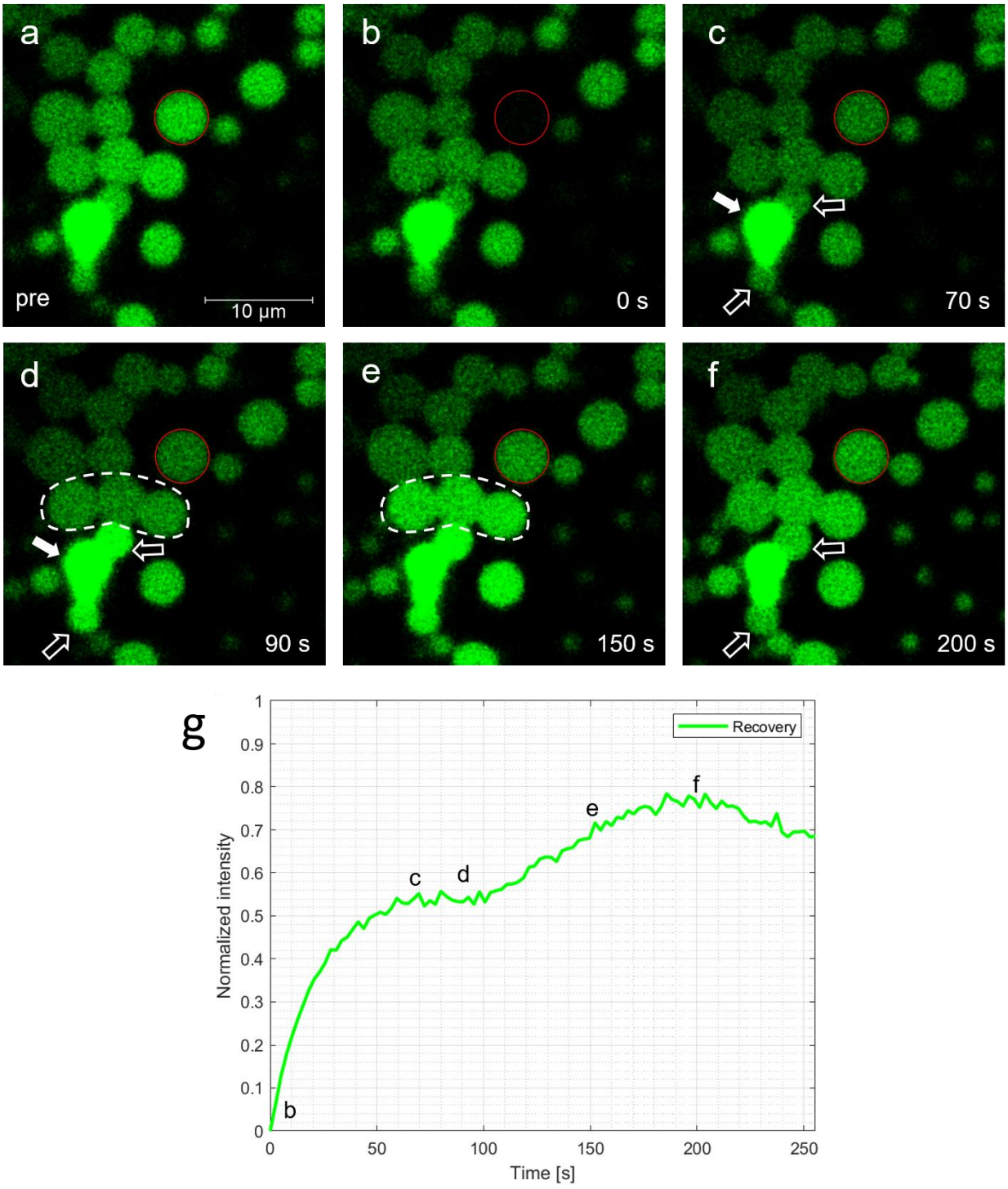

Figure 36: FRAP of a PNN vesicle containing ATTO488 (a-c). (d-f) fluorophores from a very bright compartment (white arrow) are released to the nearest vesicles (black arrows). (g) Internal fluorescence intensity of the vesicle encircled in red dashed line during (b-f).

Figure 37 shows fluorescence intensity plots of multiple vesicles in **Fig. 36a-f**. The time of the sudden fluorescence increase inside the vesicles 1-5, coincides with the increase in vesicle 6. This causes a further raise in fluorescence intensity inside this vesicle after it had recovered from the photobleaching (after 100 s.), followed by second plateau (200 s).

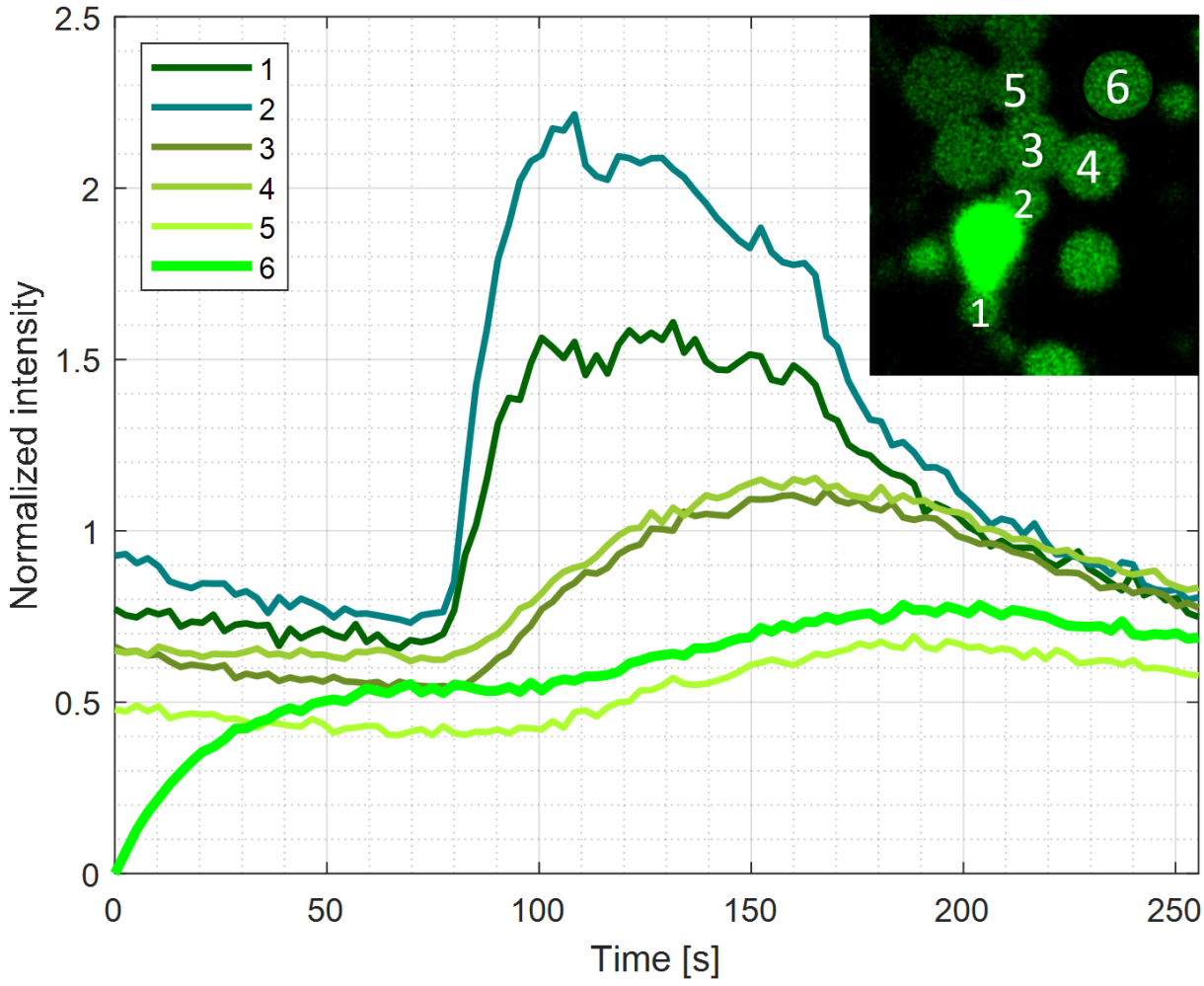

Figure 37: Fluorescence intensity of multiple vesicles (inset) during rapid fluorescence transfer. Similar to the previous recovery curves, the intensity is normalized to the values observed for the photo-bleached vesicle (6) where 1 is the average intensity before photobleaching and 0 is right after photobleaching.

There are three spreading trends based on the distance to the source compartment: Vesicle (1) and (2) are closest, then comes (3, 4) and (5, 6), where (6) is the photo-bleached vesicle. The fluorescence intensity of vesicles 1-4 decline after 170 s. This decline is delayed for vesicles 5 and 6, since they are still recovering, most likely by receiving fluorophores from vesicles 3 and 4. The fluorescence in the vesicles 1-2 (arrows in **Fig. 36f)** has diminished as compared to **Fig. 36e**,

indicating that the vesicles are no longer supplied with a high flux of fluorophores from the source vesicle. The decline in the intensity can also be due to photo-bleaching resulting from continuous imaging, or due to the distribution of the fluorescence to the compartments in the same network which are out of the field of view, or a combination of both.

It is interesting that both vesicles 1 and 2 depict an abrupt fluorescence spike at 80 s and a sudden intensity loss at 160 s. These two vesicles are positioned on opposite sides of the bright source compartment. Their synchronized response implies that they share a connection to this source compartment. It can be that the incidents are related to a sudden rupture or opening of membrane pores in the source compartment which leads to rapid release of its contents to the nearby compartments.

4.1.4 FRAP experiments on PNN vesicles containing RNA

A second set of FRAP experiments was performed on vesicles containing fluorescently labeled RNA. The protocells were initially exposed to a concentration of 100 μM of FITC-RNA for about 4 minutes. **Figures 38-41** show the results of various FITC-RNA FRAP experiments on the PNNs.

The result of the first experiment of FITC-RNA encapsulation is shown in **Fig. 38**. This is a region populated with lipid compartments of a PNN encapsulating content with high fluorescence intensity. An epi-fluorescence micrograph of the sample has been shown from top view in **Fig. 38a**, in which nanotubes are not visible. The photobleached vesicle (**Fig. 38c**) regains its fluorescence (**Fig. 38d**) where it takes about 2 minutes to reach 16% of the initial intensity as seen in the plot in **Fig. 38e**. The recovery rate is faster than for the ATTO488 FRAPs in **Fig. 34** and **Fig. 35** (both 4 minutes). The reason could be that region in **Fig. 38** is populated by more vesicles. The DIC image in **Fig. 38b** corresponds to **Fig. 38a** and shows that they are unilamellar and that there is no multilamellar vesicle in close proximity. The white arrow indicates the vesicles on which FRAP is performed.

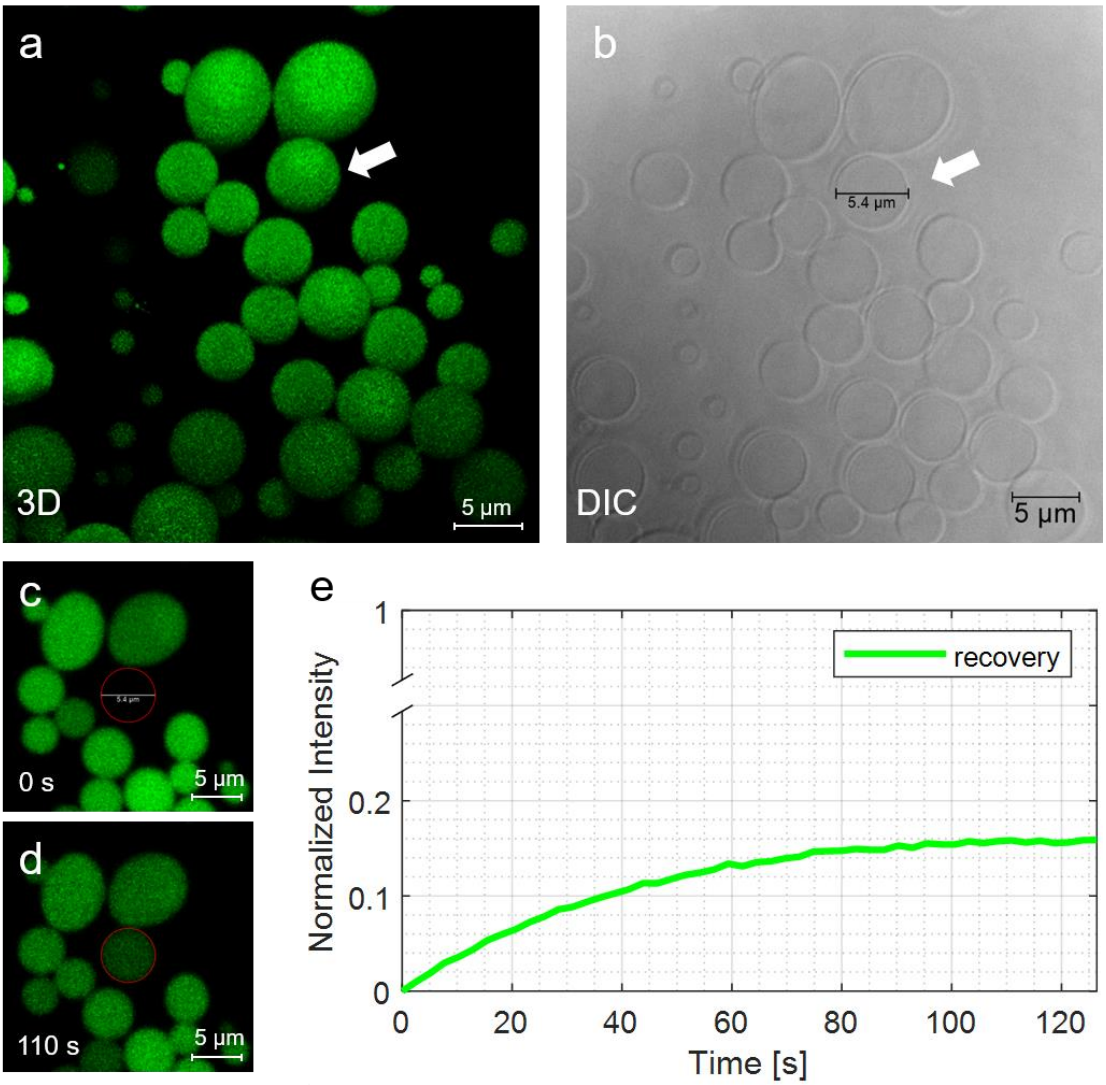

Figure 38: The first FRAP of a PNN vesicle containing FITC-RNA. White arrows in (a-b) point to the FRAP-targeted vesicle. (a) top-view fluorescence 3D micrograph, (b) DIC image of the sample region. (c-d) The photobleached vesicle (red circle) recovers as shown in the graph (e).

In the second experiment, shown in **Figure 39**, two photobleaching experiments were performed on two different vesicles within the same PNN, or in neighboring PNNs. One FRAP experiment was performed on the vesicle in **Fig. 39a, e, f** (red circle), where its fluorescence intensity reached 16% of the initial value in 1 min. (**Fig. 39h)**. The second FRAP was performed on another vesicle, indicated with a red circle in **Fig. 39b-d.** The corresponding recovery plot in **Fig. 39i** shows a 23% recovery of the initial value over 2 minutes. The regions indicated by the yellow dashed lines in the DIC image (**Fig. 39g**) display where the two photobleached vesicles (in **Fig. 39a** and **39b**) are located with respect to each other.

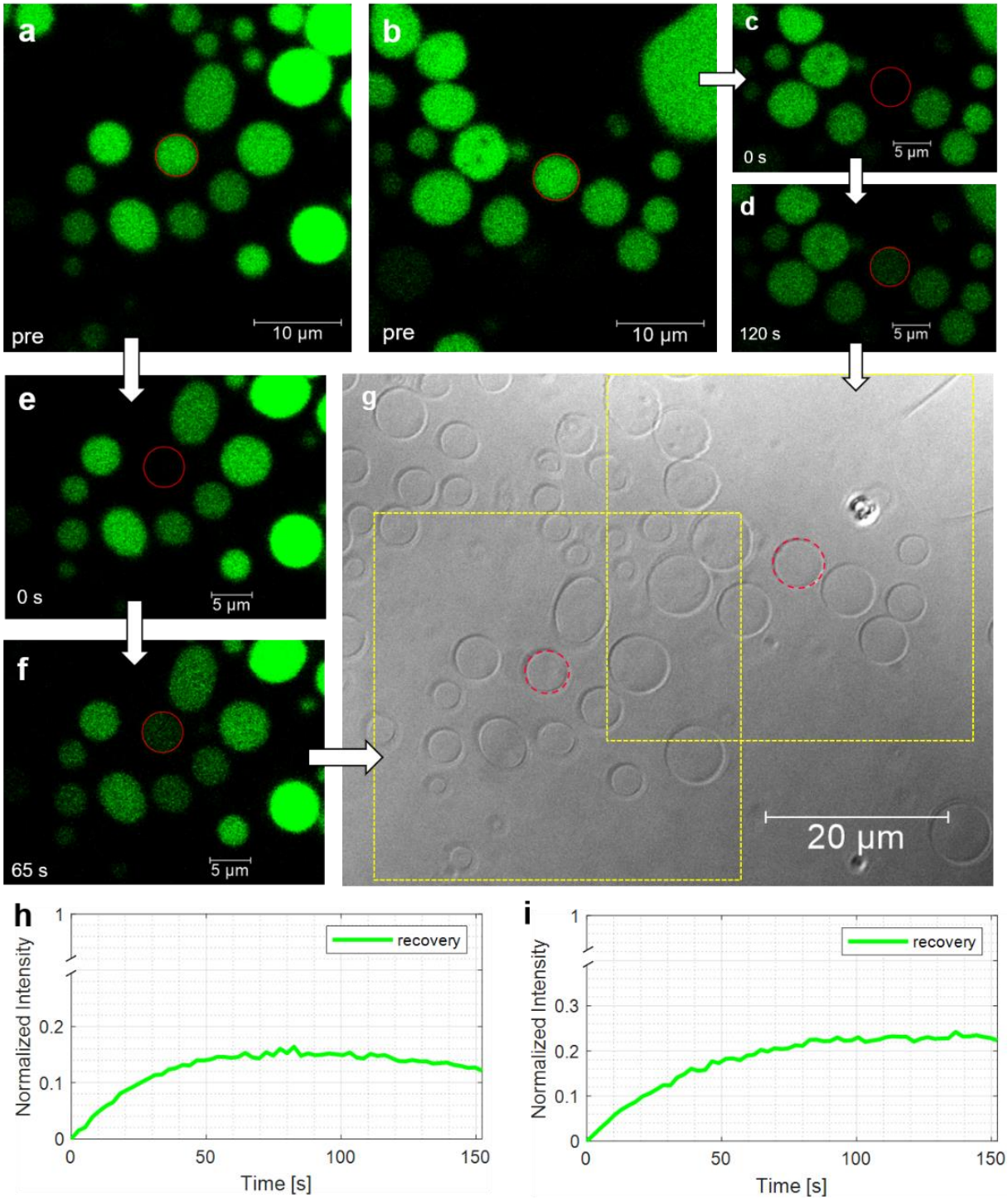

Figure 39: FRAP experiments on PNN compartments containing FITC-RNA. (a, e, f, h) shows the FRAP of one vesicle, and (b, c, d, i) shows the FRAP of a second vesicle. (g) The DIC image, which was captured after the two FRAP experiments, shows both regions in (a) and (b).

Figure 40 shows another example of FRAP on FITC-RNA containing PNN compartments. In **Fig. 40a** there are multiple fluorescent compartments, and the DIC image (**Fig. 40b**) confirms that all of them are GUVs that have encapsulated various amounts of fluorophores. **Fig. 40c** and **Fig. 40d** show the vesicle on which the FRAP was performed (red circle), at t = 0 s and t = 101 s, respectively. The recovery can be best observed in **Fig. 40e**, which demonstrates a 20% recovery of the initial fluorescence intensity in a period of 100 s.

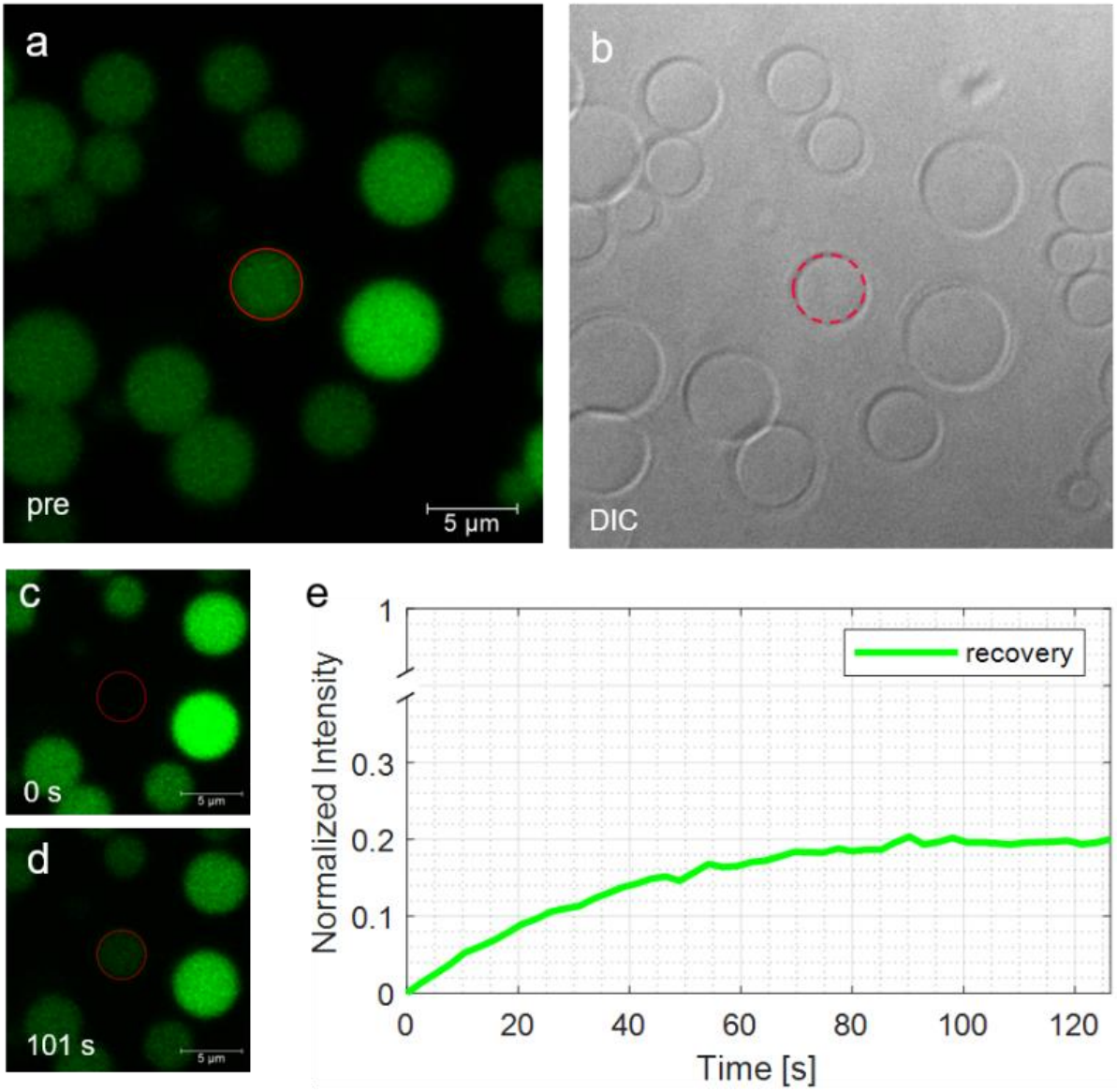

Figure 40: FRAP experiment on PNN compartments containing FITC-RNA. (a) confocal micrograph and (b) DIC image of PNN compartments. Micrographs show pre-bleach (a), and post-bleach (c, d). (e) Normalized intensity of the vesicle in red circle during recovery after photobleaching, vs. time.

The results of another FRAP experiment performed on a PNN vesicle containing FITC-RNA has been presented in **Figure 41**. A side-by-side comparison of the fluorescence image (**Fig. 41a**) and the DIC image (**Fig. 41b**) reveals that all of the vesicles in the region are GUVs with successful encapsulation. The photobleached vesicle (encircled) recovers its fluorescence (**Fig. 41c-d**) according to the plot in **Fig. 41e**. It takes approximately 100 s for the vesicle to regain 12% of its initial fluorescence intensity. In **Fig. 40e**, almost double that recovery was observed in 100 s. This indicates that the rate of the diffusion for the PNN in **Fig. 41** is somehow lower. The reason for the lower recovery could be because the photobleached vesicle in **Fig. 41** had a very high fluorescence intensity prior to photobleaching.

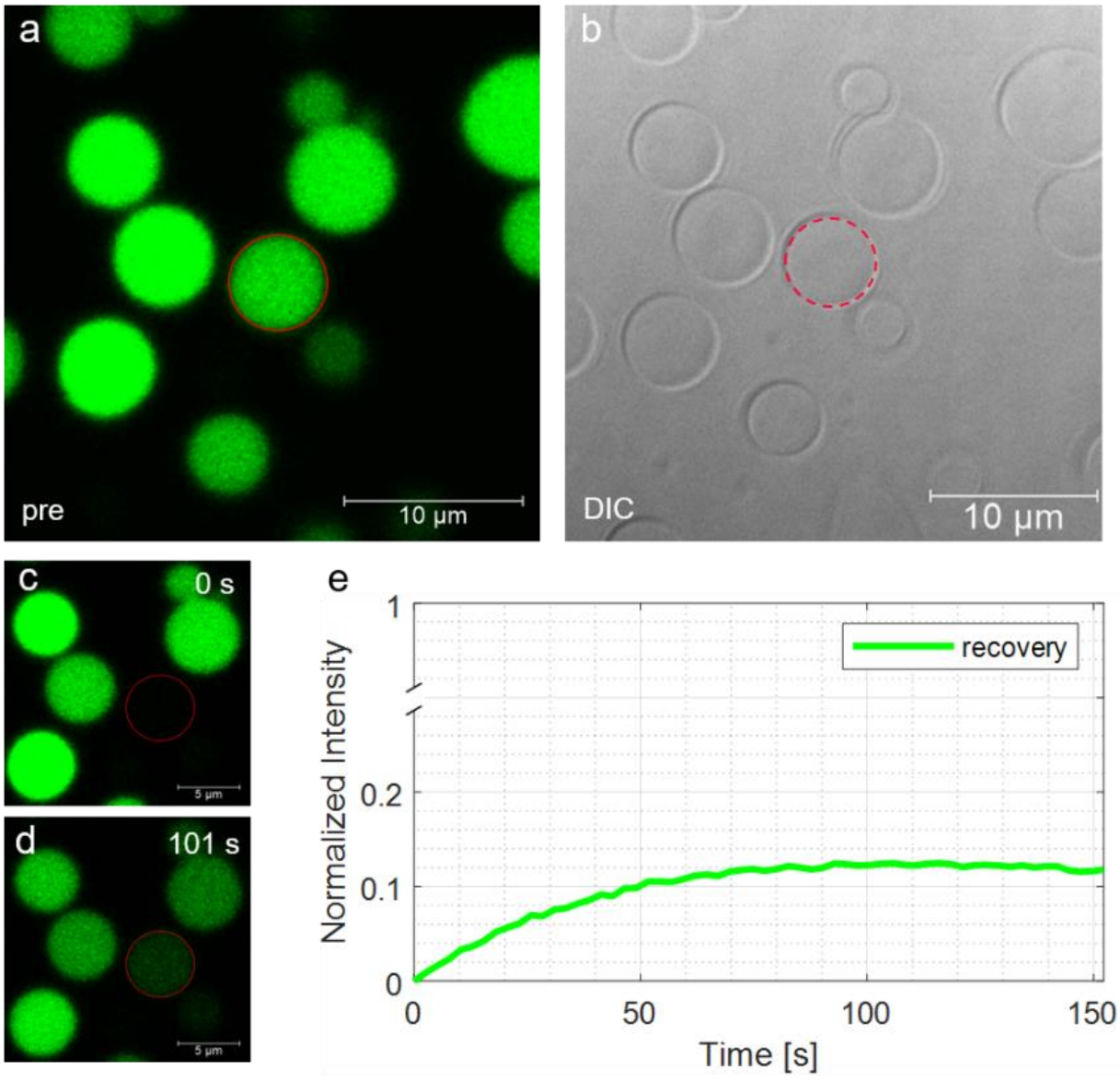

Figure 41: FRAP experiment on PNN compartments containing FITC-RNA. (a) confocal micrograph and (b) DIC image of PNN compartments. Micrographs show pre-bleach (a), and post-bleach (c, d). (e) Normalized intensity of the vesicle in red circle during recovery after photobleaching, vs. time.

In summary, the FRAP experiments with FITC-RNA in **Fig. 38-41** had comparable recovery times (around 2 min) except for the one in **Fig. 39h** which recovers relatively more rapidly (~70 s). This is comparable to the recovery observed in vesicles containing ATTO488 FRAP (1 min, **Fig. 32**).

4.1.5 FRAP experiments on PNN vesicles containing DNA

In addition to RNA, which is a single-stranded helix, a longer, single-stranded DNA was used for superfusion and studied in the context of transport within the PNNs, with FRAP. The DNA contains 20 bases and was labeled with FAM. The selected regions in PNNs were superfused with 200 μM of FAM-DNA for 3-4 min. **Figures 42-44** shows multiple FRAP experiments performed on DNA-containing PNN vesicles.

Some compartments (white arrows) in **Fig. 42a** are no longer present in the DIC image taken after the FRAP experiment (**Fig. 42b**). Their disappearance can be due to collapsing or can demonstrate that the protocells can easily separate from the network. Similar to the results shown for the networks containing ATTO488 and FITC-RNA, the fluorescence intensity of the photobleached vesicle containing FAM-DNA also recovers (**Fig. 42c-e**). The vesicle (inside the red circle) reaches a maximum recovery of 26% of the initial intensity in 4 min.

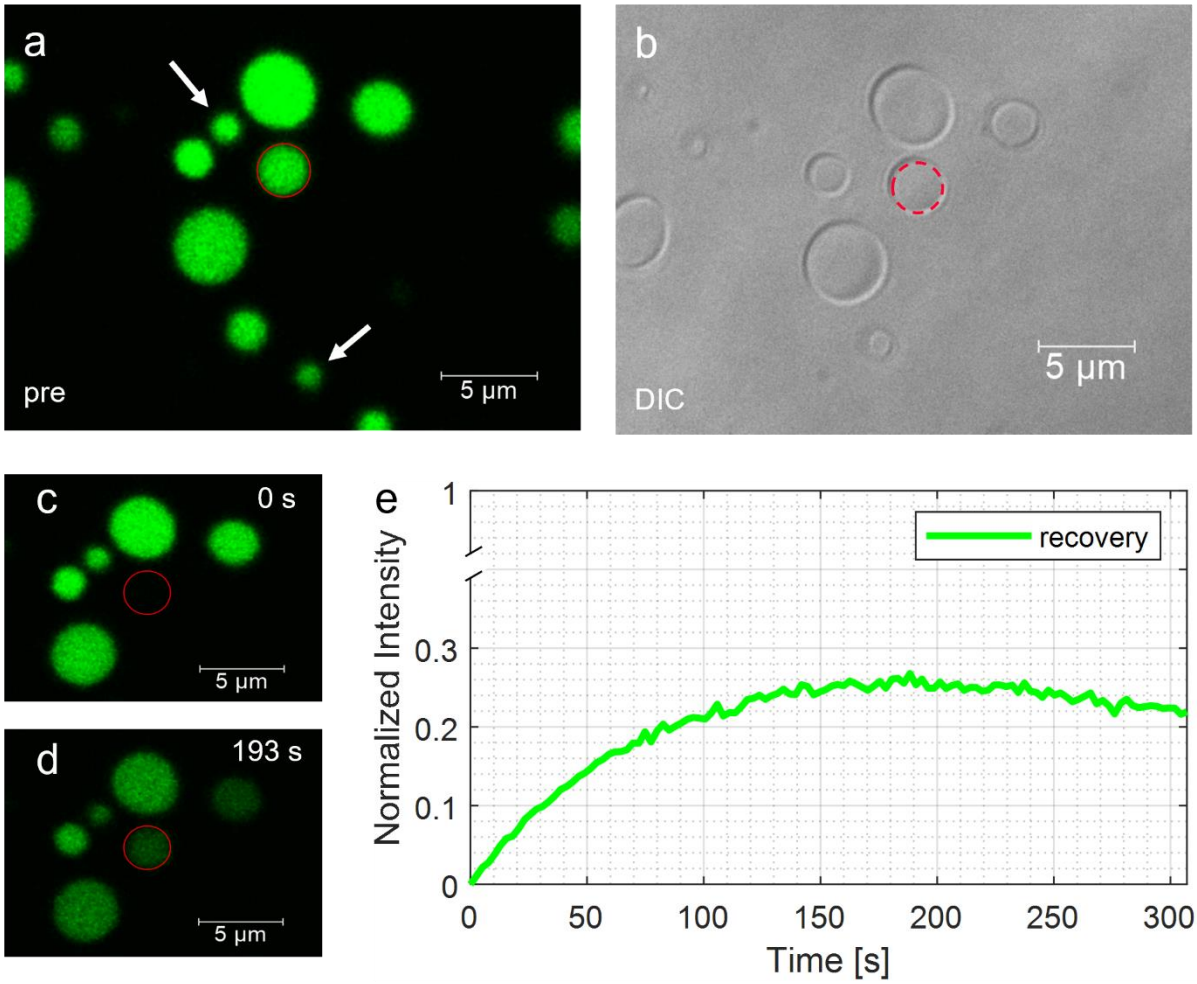

Figure 42: FRAP experiment on PNN compartments containing FAM-DNA. (a) confocal micrograph and (b) DIC image of PNN compartments. (a-d) Micrographs show pre-bleach (a), and post-bleach (c, d). (e) Normalized intensity of the vesicle in red circle during recovery after photobleaching, vs. time.

FRAP results on a second vesicle containing FAM-DNA, is shown in **Fig. 43a-c** (red circle) and its recovery curve, in **Fig. 43d**. The time for the intensity curve to reach to its plateau is approximately 3 min, which is similar to the first DNA associated experiment shown in **Fig. 42** but it only recovers to 16% of its initial pre-bleach fluorescence intensity (vs. 26% in the previous example). The surrounding vesicles in **Fig. 43d** have a high intensity relative to the recovered vesicle, suggesting that the initial transportation route (nanotube) that was responsible for the recovery during the first 150 s. has been impaired.

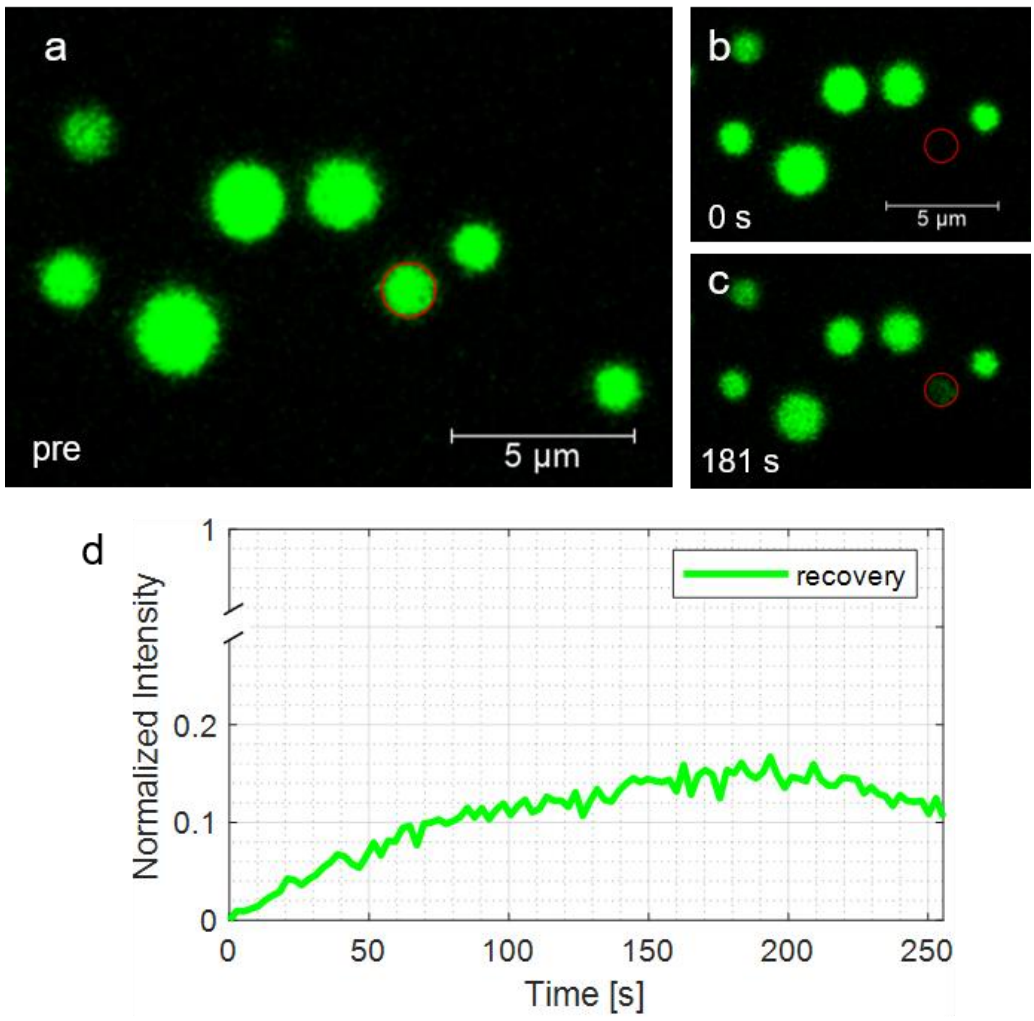

Figure 43: FRAP experiment on PNN compartments containing FAM-DNA. (a-c) confocal micrographs show pre-bleach (a), and post-bleach (b, c). (d) Normalized intensity of the vesicle in red circle during recovery after photobleaching, vs. time.

Before initializing a FRAP experiment, the recording times for pre-bleach, photobleaching, and post-bleach must be chosen. The experiment in **Figure 44** was a special case, where the FRAP lasted longer than anticipated. After 300 s, the recovery was still ongoing, but the time set for the post-bleaching time was over and the recording stopped. It took about 50 s to get the recording up and running again. Thus, the data points during ~300-360 s, the data points are missing, and the two recordings were connected with a straight line in one graph (**Fig. 44e**) By then, the fluorescence intensity was still rising, but it never reached a flat plateau, which is typical of slow and steady recovery. Instead, there was a gradual decrease in the intensity starting from 385 s and forward. The most intense fluorescence compartment in **Fig. 44c** (white arrow) disappeared

sometime between 350 s and 415 s (**Fig. 44f**). Thus, we suspect that this particular compartment was the main fluorophore supplier to the bleached vesicle. Nanotubes can be vaguely recognized in DIC mode in **Fig. 44e** between the photobleached vesicle (red dashed line) and the area where the compartment providing the fluorophores was located (yellow dashed line).

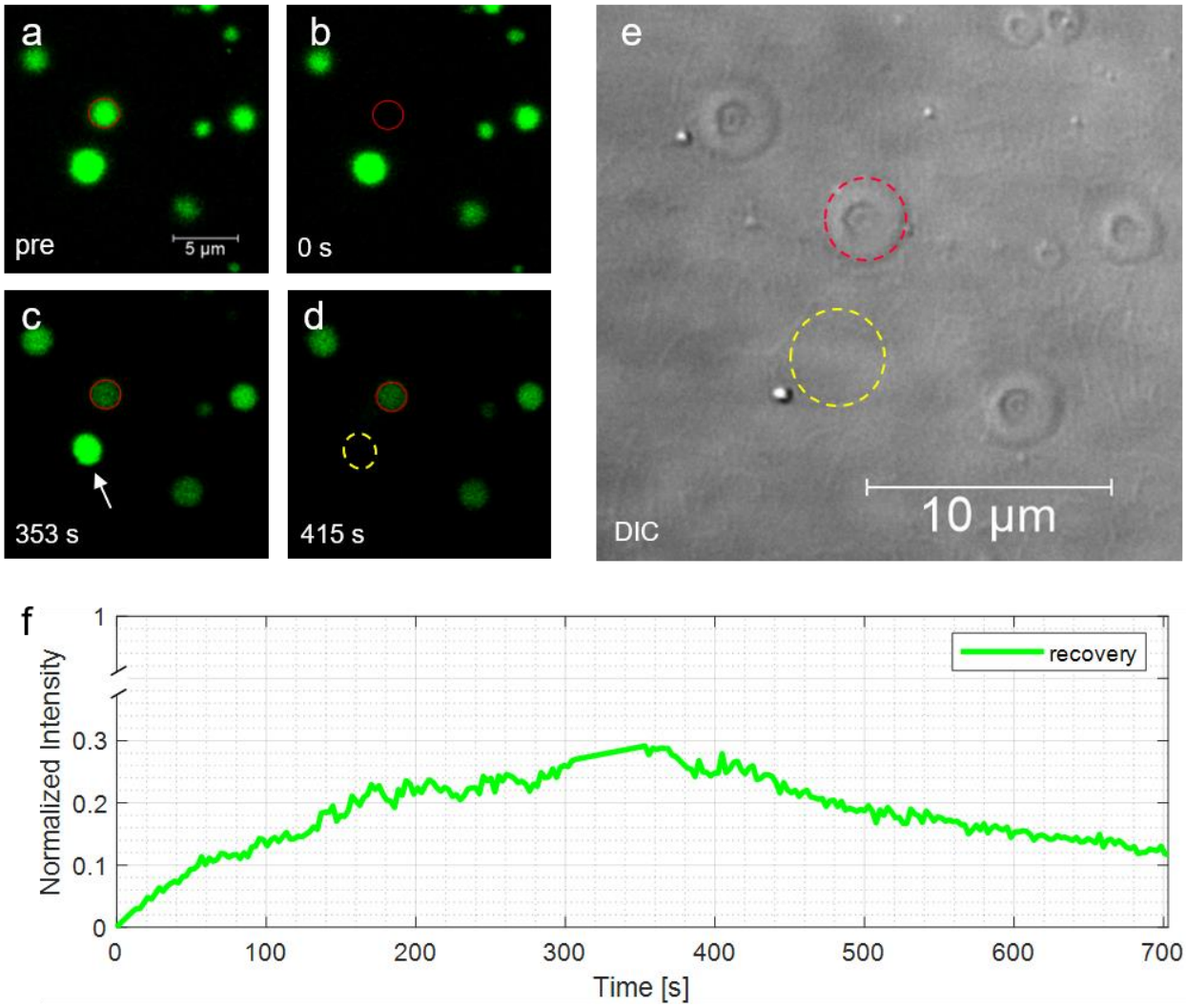

Figure 44: FRAP experiment on PNN compartments containing FAM-DNA (a-d) confocal micrographs and (e) DIC image corresponding to (a-d), of PNN compartments. (a-d) Micrographs show pre-bleach (a), and post-bleach (b-d). (f) Normalized intensity of the vesicle in red circle during recovery after photobleaching, vs. time.

The photobleached vesicles in **Fig. 42** and **Fig. 43** are 2-3 µm in diameter, and the shortest distance from them to a neighboring fluorescent vesicle, is about 1 µm. For both of these vesicles (**Fig. 42**

and **Fig. 43**), it takes 3-4 min for their FAM-DNA fluorescence to recover, which is longer than the recovery of any vesicle containing the FITC-RNA.

4.2 Determining network connections based on recovery

In this section, using the results of two FRAP experiments and insights obtained from the previous section, the simple arrangement of the nanotubes and the connection between protocells will be determined. This will be done by taking the protocells' size and distance to each other gained from microscopy images to calculate the relaxation time with **Eq. 13** and use it to fit a theoretical curve to the FRAP graph with **Eq. 14**. Some variables are unknown but can be predicted from the fit. The theoretical curve and the experimental values will then be compared to understand if the assumed connections are realistic.

4.2.1 Transport in a 2-vesicle network

The most basic system to apply the method described above is a network with only two vesicles connected with a single nanotube. **Figure 45** shows three vesicles within a 30 μm radius, all of them containing ATTO488. Two of them almost establish physical contact with each other and a slightly larger vesicle is located 10 μm away from the pair (**Fig. 45a**). For simplicity, we consider only the connection between the two vesicles in closest proximity. The two adjacent vesicles are both 4.2 μm in diameter, and after one of them is photobleached (**Fig. 45b**), it recovers its fluorescence, until the two vesicles possess the same intensity (**Fig. 45c**). The fluorescence intensities of the two vesicles over time, can be observed in **Fig. 45d**.

The relaxation time of the system was calculated with **Eq**. **13** and used in **Eq. 14** to draw an exponential curve that fits to the theoretically anticipated recovery of the fluorescence inside the photobleached vesicle **(Fig. 22e)**. In the calculations, it is assumed that the vesicles involved are perfect spheres and that straight nanotubes connect the spheres at the bottom. Hence, the length l, of the nanotube has been approximated to be the sum of the radii of the two vesicles, plus the distance l', between them. The relaxation time was calculated with **Eq. 13** using the following values: $d_1 = d_2 = 4.2\ \mu m,\ l' = 0.1\ \mu m,\ r = 50\ nm$ and $D = 4\ Å m s^{-1}$ where D corresponds to

the diffusion coefficient of ATTO488 carboxy (1 angstrom, Å = 10^{-10} m). This results in a relaxation time, $t_{relax} = 26.5\ s$, which was plugged into **Eq. 14** assuming 40% recovery (A=0.4), and we see that the theoretical curve that was plotted in **Fig. 45e** fits to the experimental trend of fluorescence recovery. As a result, instead of steady state intensity at 50%, the intensities gradually decrease over time. This observation is comparable to the numerical solution for diffusion through a two-node network proposed by Lizana and Konkoli [79, Fig. 6].

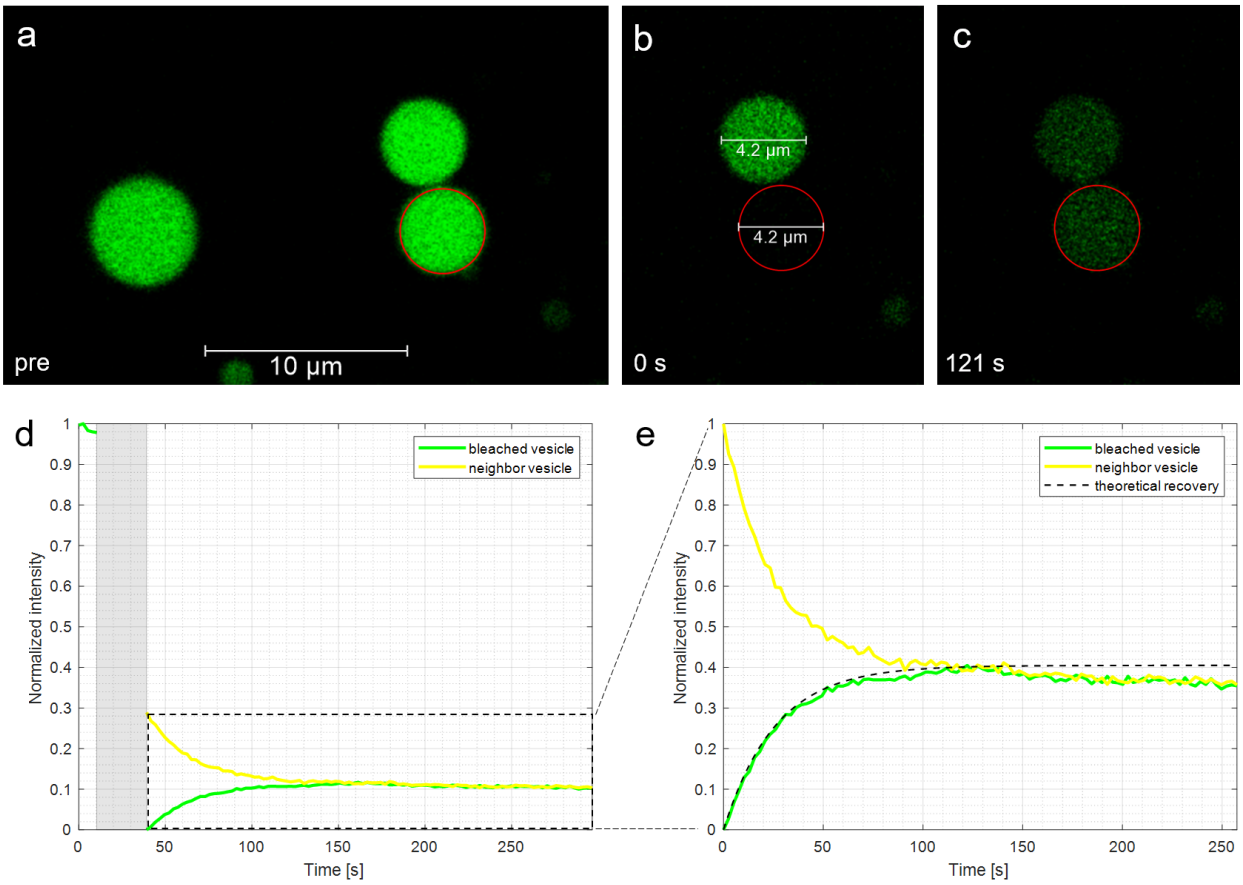

Figure 45: Transport of ATTO488 in a 2-vesicle system. (a) micrograph of the region with two compartments, one other compartment is 10 µm away. (b) 2 adjacent vesicles (4.2 µm in diameter) in (a), right after photobleaching, and (c) when their intensities reach equilibrium. (d) plot showing the fluorescence intensities in adjacent vesicles, during pre-bleach, photobleaching (gray zone) and post-bleaching periods. The values are normalized to the highest intensity value during pre-bleach period. In (e), the intensities in (d) are re-normalized to highest intensity value of the neighbor vesicle and lowest intensity value of photo-bleached vesicle, and the time at the start of the post-bleach is set to zero. The dashed line shows the theoretical fit.

The time scale of the recovery in **Fig. 45d-e**, the time spent to reach steady state fluorescence intensity, is comparable to that of the ATTO488 containing networks. The recovery time for the ATTO488 containing compartments shown in **Fig. 32** is 70 second. The photobleached compartment in this experiment has approximately 5 μm distance to others and recovering due to the presence of a nanotubular connection. In the experiment shown in **Fig. 45**, the fluorescence recovery is occurring at the same time scale as a vesicle recovering by receiving new material from another vesicle at 5 μm distance. This implies that the transport of molecules in in the 2-vesicle system in **Fig. 45** is not direct, i.e., not occurring through a fusion pore. In that case the intensity would be expected to recover in a much faster time scale.

4.2.2 Changing variables in a 4-vesicle system

The previous section demonstrated how to fit a theoretical curve to the fluorescence recovery in a simple system containing two vesicles connected with a single nanotube. Although a lot of approximations were made, the model was mostly in agreement with the experimental data. In **Figure 46** another simple PNN arrangement, this time with 4 vesicles has been investigated. In this 4-vesicle system there are three compartments in a 5 μm distance to the photobleached protocell as shown in **Fig. 46a**. The PNN was exposed to FAM-DNA, and as the scalebar in the fluorescence image indicates (**Fig. 46a**); the distances between the vesicles are about 1 μm. Protocell diameters (4–5 nm) are shown in the DIC image (**Fig. 46b**) and the rim of a double lipid bilayer patch can be observed at the lower right part of the image (white arrow). Hence, the focus is on the surface, but the nanotubes are not visible. Once again, it is the FRAP experiment (**Fig. 46a, c-d**) that reveals the presence of the nanotubes, because they are the only explanation for the recovery.

The recovery for this 4-vesicle system (**Fig. 46e**) reaches a steady state around 120 s. The time for the ATTO dye to recover in the two-vesicle system (**Fig. 45e**) was also approximately 120s. Despite that the vesicles have similar sizes in these two different systems, there are some distinctions between the two experiments. The 4-vesicle system (**Fig. 46**) contains FAM-DNA and the DNA which is single stranded and is 20-bases long has a diffusion coefficient of $1.52 \cdot 10^{-10}$ m^2s^{-1} [80]. This is one third of the diffusion coefficient of ATTO488 ($4 \cdot 10^{-10}$ m^2s^{-1}) [81]. Moreover, the distance between the vesicles in the 4-vesicle system is higher in the 2-vesicle system.

If only these two factors i.e., diffusion coefficient and inter-vesicle distance were considered, one would expect the diffusion and hence the recovery within this current system to be slower. However, the comparison between **Fig. 45e** and **Fig. 46e** reveals that this is not the case. Since we assume that the sole reason for recovery is a nanotube connection, it possible that the bleached vesicle is connected to more than one protocell.

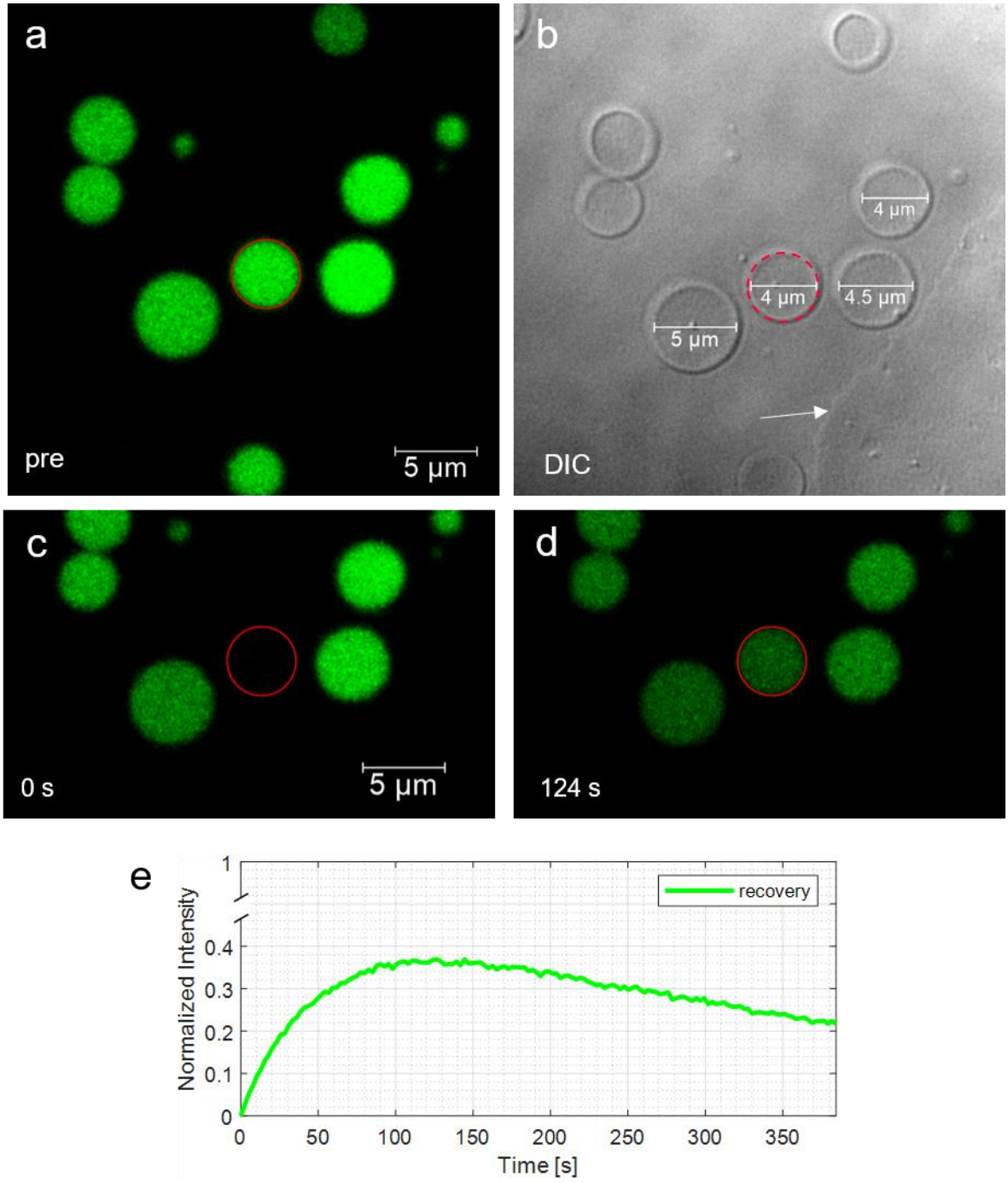

Figure 46: Transport of FAM-DNA in a 4-vesicle system. (a) Confocal micrographs and (b) DIC image of the PNN. (c-d) Recovery after photobleaching (e) Plot showing the fluorescence intensity of the vesicle in red circle, vs time.

Although the system in **Fig. 46** looks simple with only four main vesicles, there are many probable ways the vesicles could be connected. Since nanotubes are not always visible in DIC images and their positions can rearrange over time, it had been challenging to determine the position of the nanotubes underlying the vesicles by imaging. We instead, looked at the intensity drop of the compartments surrounding the recovering vesicle in the same manner. Unfortunately, it becomes more challenging to deduce the direct correlations if the recovering vesicle have several neighbors (>1).

Figure 47 shows the intensity changes over time for the protocells shown in **Fig. 46**. None of them exactly resembles the decaying trend of the supplying vesicle in the 2-vesicle system (**Fig. 45e**), but it is clear that the fluorescence intensities of all surrounding vesicles are decreasing over time. It could be that all 3 vesicles (#2-3-4) are connected to, and help recover, vesicle #1

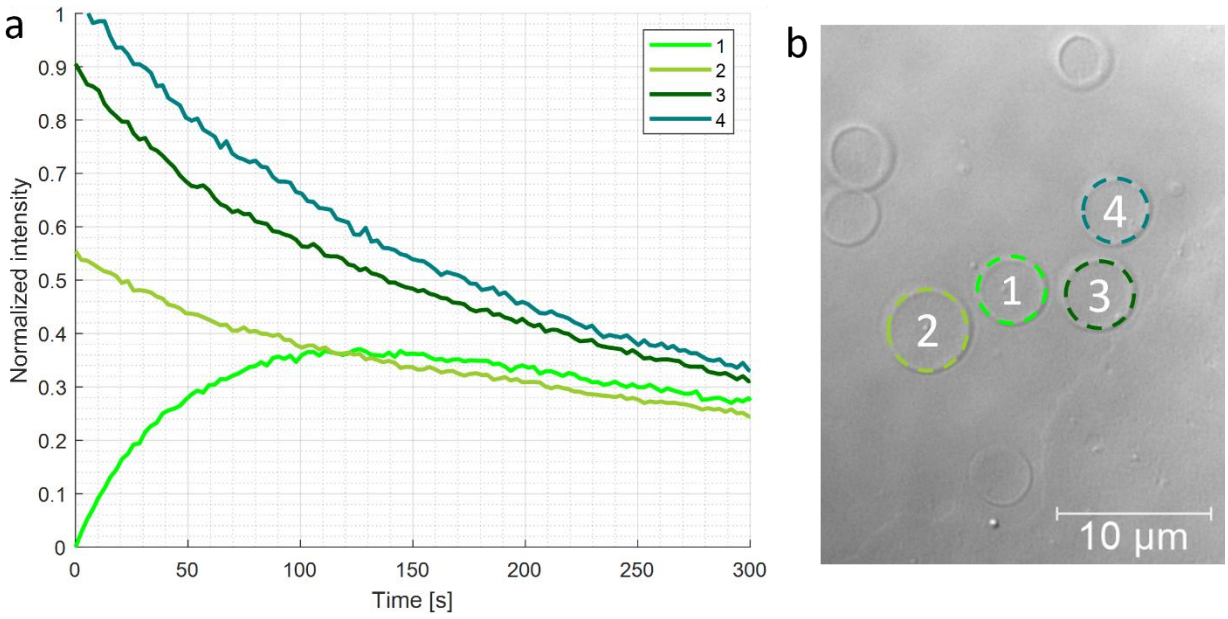

Figure 47: FAM-DNA fluorescence intensity in the adjacent protocells, over time. (a) The post-bleach intensities of the photobleached protocell (1) and three adjacent compartments (2-4). (b) DIC Image showing the numbers corresponding to each compartment in (a).

Although **Eq. 13** is suitable for a 2-vesicle system, it was still used to theoretically fit a curve to the fluorescence recovery of the network shown in **Fig. 46**. **Figure 48** shows the effect on the theoretical curve when changing either r, d_2, l' or D of **Eq. 13,** while keeping the other variables constant. The values of the constant variables are derived from the microscope images and are as follows: $d_1 = 4\ \mu m,\ d_2 = 5\ \mu m$ and $l' = 1\ \mu m$. Additionally, $D = 1.5\ Å m s^{-1}$ has been used as for the diffusion coefficient, as it corresponds to the D of 20-base single-stranded DNA. Meanwhile the recovery, A, used in **Eq. 14** to plot the theoretical fit, was set to 37% since that is how much the photo-bleached vesicle recovers in **Fig. 46e**. The theoretical fit based on all the exact values above can be observed in **Fig. 48a**. The nanotube radius, $r = 86\ nm$, can be predicted from the fit, which corresponds to a relaxation time, $t_{relax} = 35\ s$. This radius was also used as a constant while changing the other variables in **Fig. 48b-e**.

Remember that the defined length, $l = l' + \frac{1}{2}(d_1 + d_2)$, assumes that the two vesicles are spheres and that the nanotube connecting them at their base is straight. A greater value of l', signifies that a longer nanotube, for instance, a nanotube that is not straight. Similarly, a smaller l' means the nanotube is shorter. This can be the case for example if the vesicles are not perfectly spherical but have a flat base. The effect of varying the nanotube length by 2 μm is calculated and plotted in **Fig. 48b**. As expected, an increased nanotube length results in slower recovery due to the longer relaxation time calculated with **Eq. 13**.

The next variable that was investigated was the vesicle size. The diameter of the photo-bleached vesicle in **Fig. 46b** is 4 μm. Both this vesicle and the surrounding ones can vary in size. For simplicity, only one of the neighboring compartment's diameter, d_2, was adjusted by 1 μm at a time (**Fig. 48c**). From **Eq. 13** one would expect that the diameter (in form of d^3) has a huge impact on the relaxation time. However, the effect is similar to changing the nanotube length by 2 μm (**Eq. 13**), at least for vesicles with diameters (d_2) ranging from 4 μm to 6 μm. The volume of the vesicle that supplies the fluorophore to the photo-bleached vesicle for recovery, does not seem to have a big influence. Although a larger volume means the vesicle contains more fluorescence its impact is little if the concentration is the same of a smaller vesicle, since the diffusion is governed by the concentration gradient.

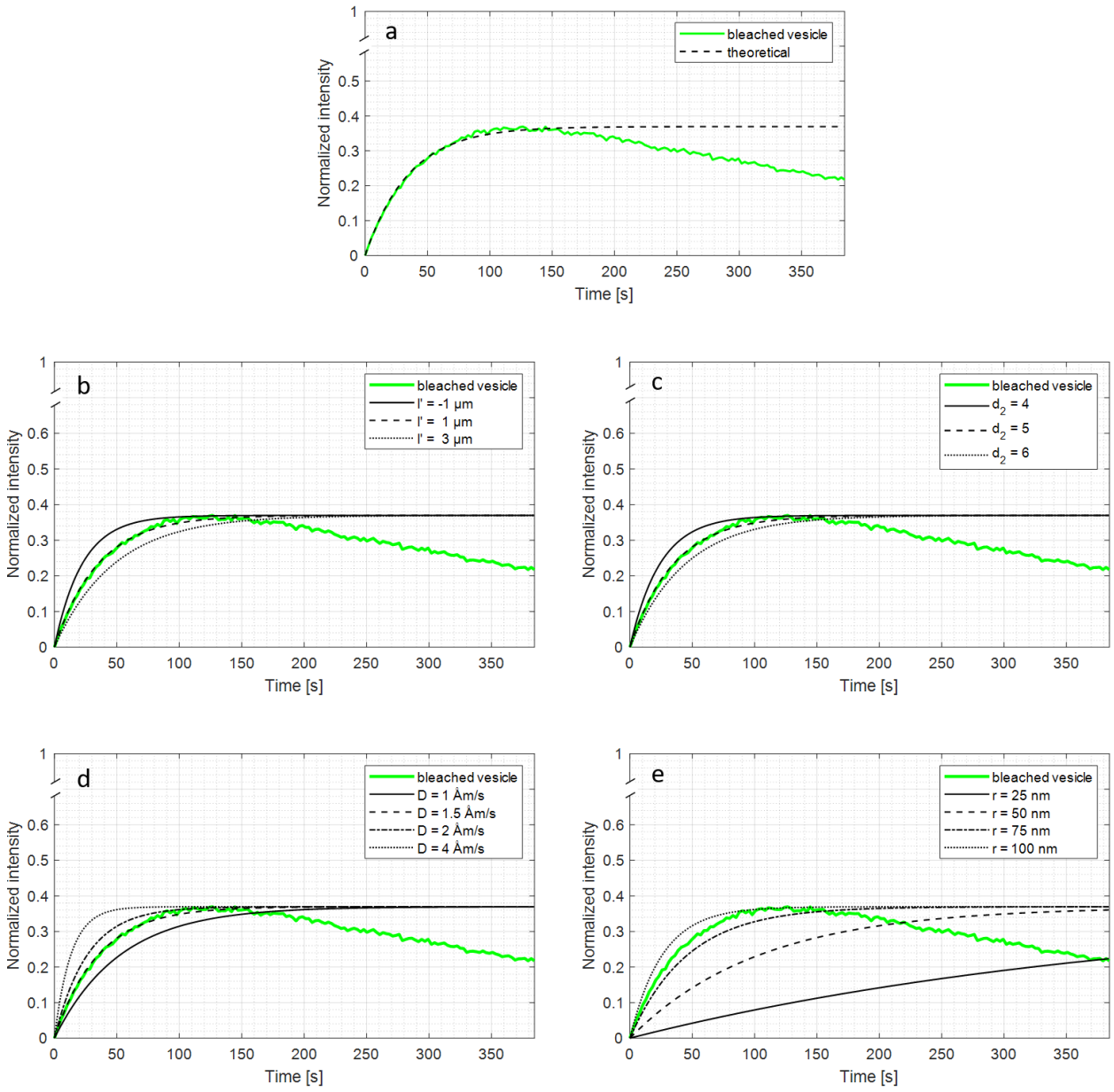

Figure 48: Theoretical curve fits to the recovery of the bleached vesicle (in green) and their change in variables. (a) The final theoretical fit from using all the constants. Other curves are obtained when changing only the (b) radius of nanotubes, (c) length of nanotubes, (d) diameter of the neighboring vesicle, or (e) diffusion coefficients.

The FRAP experiment in this section was performed on a network that had encapsulated FAM-DNA. The diffusion coefficient of a single-stranded DNA with 20 bases is around 1.52 Å/s [80]. The diffusion coefficient for ATTO488 and single stranded RNA with ten bases is 4.0 Å/s [81] and 2.0 Å/s [82], respectively. The theoretical fluorescence recovery curves of molecules with

varying diffusion coefficients, including the ATTO488 and ten base RNA, can be observed in **Fig. 48d**. As expected, a vesicle containing a compound with lower diffusion coefficient takes longer to recover.

Bending energy of a nanotube is $\frac{\kappa_b \pi l}{r}$ (**Eq. 8**, section **2.2**,); it is inversely proportional to the radius. In other words, the energy of a nanotube increases with high curvature (1/*r*). The radius of a biological tunneling nanotube typically ranges between 25-100 nm [28, 73]. The radii of ER nanotubes are around 30 nm, and in some species, they can be as small as 15 nm [83]. Upholding these curvatures require energy which is provided by the stabilizing proteins. Examples of membrane deforming and remodeling proteins are clathrin and dynamin, which are responsible for the budding of vesicles and fission of nanotubes. [84] **Fig. 48e** shows the curve fitting according to nanotube radius. Among all the variables, it has the biggest impact in diffusion-based transport rate, especially at lower radii. Since the radii of biological tubular structures can be lower than model systems, this could also mean that in modern biological systems the diffusion rates are expected to be lower.

Fig. 48a shows that in this network, the flow of FAM-DNA in a vesicle with a diameter of 4μ is comparable to that of 2-vesicle system with nanotube radius of 86 nm. This was just one of the many possible approximations, as similar fits can be achieved by changing two or more variables at once. As long as the values are reasonable, especially with respect to nanotube radius, any combination which gives a relaxation time of 35 s when plugged into **Eq. 13** will also fit the recovery curve. However, none of these fits can accurately represent the 4-vesicle-network, because they are calculated with an equation meant for a 2-vesicle system.

5 Conclusion

The first aim of this thesis was to grow protocell-nanotube networks with label-free lipids to eliminate the possible impact of fluorescence dyes in formation and development of PNNs. DIC microscopy was used to image the transparent network structures. The formation of PNNs made both from bacteria- and plant-derived lipids, was observed.

The second and main purpose of the work in this thesis was to investigate whether the nanotubes in the PNNs were open and could facilitate the transport of compounds between distant vesicular compartments. Since the first goal was successfully achieved, next, the transport capabilities of the unlabeled PNNs were studied, with fluorescently labeled cargo locally delivered to the networks.

Superfusion of the PNNs with the above-mentioned constituents delivered by a microfluidic pipette, induced protocell growth while simultaneously enabling the uptake. The ATTO488-dye, FITC-RNA (10-bases) and single-stranded FAM-DNA (20-bases) were encapsulated in selected compartments inside the PNNs. A 3D confocal micrograph captured the ATTO488 internalized in both the protocells and nanotubes. The transport of fluorophores was confirmed via fluorescence recovery after photobleaching. Briefly, selected compartments in a PNN encapsulating fluorescently labeled cargo, were photo-bleached using high power laser and the recovery was monitored. The recovery time, the time which took the internal fluorescence intensity of a compartment to reach steady state, was generally 1–3 minutes for protocells with connected compartments that were maximum 5 μm apart. Recovery times were mostly in agreement with the diffusion coefficients of cargo molecules.

We demonstrated through FRAP experiments that the compartments in protocell-nanotube networks, can redistribute compounds via nanotubes acting as highways for transportation. The results, which are summarized in **Figure 49** support the hypothesis about communication and division of primitive cells that are interconnected with nanotubes.

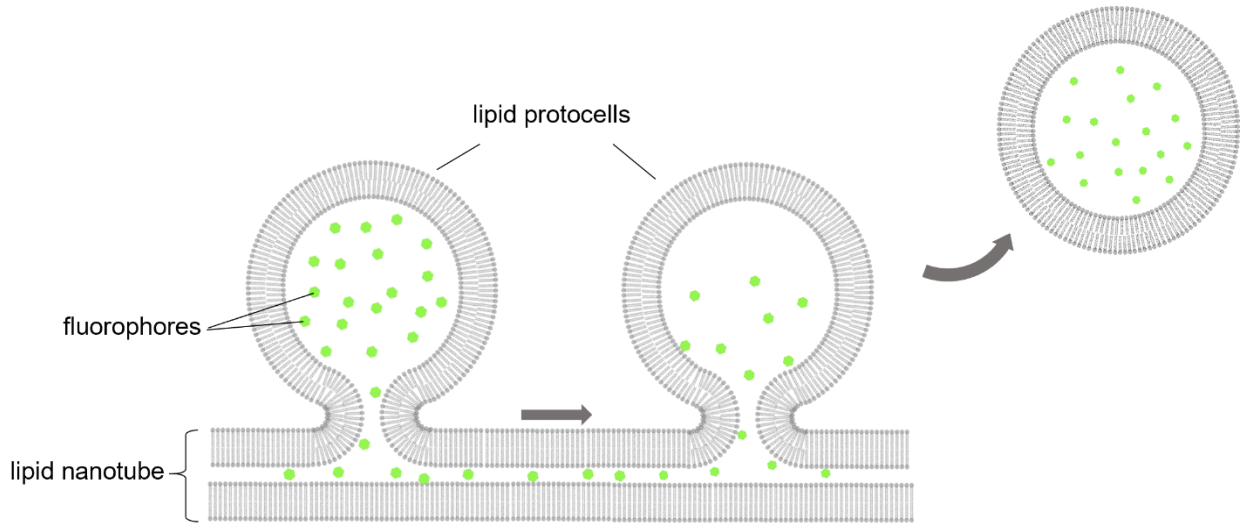

Figure 49: PNN formation with unlabeled lipids, and transport of molecules between protocells via the nanotubular connections. The observations suggest a possible mechanism for communication between primitive cells.

The results are in some simple ways similar to cell-to-cell communication in modern cells. Cellular communication occurs when a signaling molecule secreted from one cell, reaches to another cell at a distance, by which it is recognized and taken up. One of the ways that the signaling compounds are released from one cell is, passive diffusion. This is similar to what the model protocells in PNNs perform. [3]. A direct means of communication between cells occurs through tunneling nanotubes [28] which in the PNN model studied in this thesis, are directly represented. It is plausible that the primitive cell networks have communicated, i.e., exchanged information, via tunneling lipid nanotubes and shared contents by transport via molecular diffusion.

As a next step, larger compounds such as nanoparticles, delivered via liposomal fusion, can be introduced to PNNs to find the size limit of effective transportation. Finally, prebiotic reaction networks [85] can be encapsulated and run in the PNNs, which would bring this model system a step closer towards abiogenesis.

References

[1] I. Gilmour, M. A. Sephton, A. Conway, D. A. Rothery, M. Anand, B. W. Jones, M. R. Patel, S. P. Schwenzer, and J. C. Zarnecki, *An Introduction to astrobiology*, 3rd ed. Cambridge: Cambridge University; in association with Open University, 2018.

[2] B. Ghosh, R. Bose, and T. Y. D. Tang, "Can coacervation unify disparate hypotheses in the origin of cellular life?," *Current opinion in colloid & interface science*, vol. 52, p. 101415, 2021, doi: 10.1016/j.cocis.2020.101415.

[3] B. Alberts, J. H. Wilson, and T. Hunt, *Molecular biology of the cell*, 6th ed. New York: Garland Science, 2015.

[4] O. Leslie E, "Prebiotic Chemistry and the Origin of the RNA World," *Critical Reviews in Biochemistry and Molecular Biology*, vol. 39, no. 2, pp. 99-123, 2004, doi: 10.1080/10409230490460765.

[5] S. M. Awramik, "Palaeontology Respect for stromatolites," *Nature*, vol. 441, no. 7094, pp. 700-701, 2006, doi: 10.1038/441700a.

[6] T. Djokic, M. J. Van Kranendonk, K. A. Campbell, M. R. Walter, and C. R. Ward, "Earliest signs of life on land preserved in ca. 3.5 Ga hot spring deposits," *Nat Commun*, vol. 8, no. 1, pp. 15263-15263, 2017, doi: 10.1038/ncomms15263.

[7] B. Damer and D. Deamer, "The Hot Spring Hypothesis for an Origin of Life," *Astrobiology*, vol. 20, no. 4, pp. 429-452, 2020, doi: 10.1089/ast.2019.2045.

[8] D. Deamer, "The Role of Lipid Membranes in Life's Origin," *Life (Basel)*, vol. 7, no. 1, p. 5, 2017, doi: 10.3390/life7010005.

[9] J. Baross, M. J. Russell, D. Kelley, and W. Martin, "Hydrothermal vents and the origin of life," *Nat Rev Microbiol*, vol. 6, no. 11, pp. 805-814, 2008, doi: 10.1038/nrmicro1991.

[10] R. M. Hazen and D. A. Sverjensky, "Mineral surfaces, geochemical complexities, and the origins of life," *Cold Spring Harb Perspect Biol*, vol. 2, no. 5, pp. a002162-a002162, 2010, doi: 10.1101/cshperspect.a002162.

[11] E. Parrilli, F. Sannino, G. Marino, and M. L. Tutino, "Life in icy habitats: new insights supporting panspermia theory," *Atti della Accademia nazionale dei Lincei. Rendiconti Lincei. Scienze fisiche e naturali*, vol. 22, no. 4, pp. 375-383, 2011, doi: 10.1007/s12210-011-0136-2.

[12] D. W. Deamer, W. R. Hargreaves, and S. J. Mulvihill, "Synthesis of phospholipids and membranes in prebiotic conditions," *Nature*, vol. 266, no. 5597, pp. 78-80, 1977, doi: 10.1038/266078a0.

[13] M. Rao, J. Eichberg, and J. Oró, "Synthesis of phosphatidylcholine under possible primitive earth conditions," *J Mol Evol*, vol. 18, no. 3, pp. 196-202, 1982, doi: 10.1007/BF01733046.

[14] M. Rao, J. Eichberg, and J. Oró, "Synthesis of phosphatidylethanolamine under possible primitive earth conditions," *J Mol Evol*, vol. 25, no. 1, pp. 1-6, 1987, doi: 10.1007/BF02100033.

[15] K. H. Lemke, R. J. Rosenbauer, and D. K. Bird, "Peptide synthesis in early earth hydrothermal systems," *Astrobiology*, vol. 9, no. 2, pp. 141-146, 2009, doi: 10.1089/ast.2008.0166.

[16] M. W. Powner, B. Gerland, and J. D. Sutherland, "Synthesis of activated pyrimidine ribonucleotides in prebiotically plausible conditions," *Nature,* vol. 459, no. 7244, pp. 239-242, 2009, doi: 10.1038/nature08013.
[17] P. Walde, "Building artificial cells and protocell models: Experimental approaches with lipid vesicles," *BioEssays,* Note vol. 32, no. 4, pp. 296-303, 2010, doi: 10.1002/bies.200900141.
[18] A. J. Dzieciol and S. Mann, "Designs for life: protocell models in the laboratory," *Chem Soc Rev,* vol. 41, no. 1, pp. 79-85, 2011, doi: 10.1039/c1cs15211d.
[19] M. Abbas, W. P. Lipi ski, J. Wang, and E. Spruijt, "Peptide-based coacervates as biomimetic protocells," *Chem Soc Rev,* vol. 5, no. 6, pp. 369-375, 2021, doi: 10.1039/d0cs00307g.
[20] P. A. Monnard and P. Walde, "Current ideas about prebiological compartmentalization," *Life,* Review vol. 5, no. 2, pp. 1239-1263, 2015, doi: 10.3390/life5021239.
[21] K. Adamala and J. W. Szostak, "Competition between model protocells driven by an encapsulated catalyst," *Nature Chemistry,* Article vol. 5, no. 6, pp. 495-501, 2013, doi: 10.1038/nchem.1650.
[22] I. Budin and J. W. Szostak, "Physical effects underlying the transition from primitive to modern cell membranes," *Proc Natl Acad Sci U S A,* vol. 108, no. 13, pp. 5249-5254, 2011, doi: 10.1073/pnas.1100498108.
[23] I. Gozen and P. Dommersnes, "Biological lipid nanotubes and their potential role in evolution," *The European physical journal. ST, Special topics,* vol. 229, no. 17-18, pp. 2843-2862, 2020, doi: 10.1140/epjst/e2020-000130-7.
[24] J. C. Gray, J. A. Sullivan, J. M. Hibberd, and M. R. Hansen, "Stromules: Mobile Protrusions and Interconnections Between Plastids," vol. 3, ed. Oxford, UK, 2001, pp. 223-233.
[25] M. R. Hanson and K. M. Hines, "Stromules: Probing Formation and Function," *Plant physiology,* vol. 176, no. 1, p. 128, 2018, doi: 10.1104/pp.17.01287.
[26] M. Dupont, S. Souriant, G. Lugo-Villarino, I. Maridonneau-Parini, and C. Verollet, "Tunneling Nanotubes: Intimate Communication between Myeloid Cells," *Frontiers in Immunology,* vol. 9, 2018, doi: 10.3389/fimmu.2018.00043.
[27] G. P. Dubey and S. Ben-Yehuda, "Intercellular Nanotubes Mediate Bacterial Communication," *Cell,* vol. 144, no. 4, pp. 590-600, 2011, doi: 10.1016/j.cell.2011.01.015.
[28] A. Rustom, R. Saffrich, I. Markovic, P. Walther, and H.-H. Gerdes, "Nanotubular Highways for Intercellular Organelle Transport," *Science,* vol. 303, no. 5660, pp. 1007-1010, 2004, doi: 10.1126/science.1093133.
[29] S. Jérôme, S. Pia, R. Ralf, B.-W. Françoise, and B. Patricia, "Vesicles surfing on a lipid bilayer: Self-induced haptotactic motion," *Proceedings of the National Academy of Sciences,* vol. 103, no. 33, p. 12382, 2006, doi: 10.1073/pnas.0601400103.
[30] M. Liang, L. Ying, P. Junya, W. Danni, Z. Xiaoxin, C. Yitong, C. Lilian, Y. Xiaojun, D. Yanan, and Y. Li, "Discovery of the migrasome, an organelle mediates release of cytoplasmic contents during cell migration," *Cell Research,* 2014, doi: 10.1038/cr.2014.135.
[31] A. Ainla, I. Gözen, B. Hakonen, and A. Jesorka, "Lab on a Biomembrane: Rapid prototyping and manipulation of 2D fluidic lipid bilayers circuits," *Scientific Reports,* Article vol. 3, 2013, Art no. 2743, doi: 10.1038/srep02743.

[32] E. Sackmann, "Supported membranes: Scientific and practical applications," *Science,* vol. 271, no. 5245, p. 43, 1996.
[33] I. Wegrzyn, H. Zhang, O. Orwar, and A. Jesorka, "Nanotube-interconnected liposome networks," *Nano Communication Networks,* vol. 2, no. 1, pp. 4-15, 2011, doi: 10.1016/j.nancom.2011.02.003.
[34] M. Karlsson, K. Sott, M. Davidson, A.-S. Cans, P. Linderholm, D. Chiu, and O. Orwar, "Formation of Geometrically Complex Lipid Nanotube-Vesicle Networks of Higher-Order Topologies," *Proc Natl Acad Sci U S A,* vol. 99, no. 18, pp. 11573-11578, 2002, doi: 10.1073/pnas.172183699.
[35] J. Aldo, S. Natalia, Z. Haijiang, O. Bahanur, H. Bodil, and O. Owe, "Generation of phospholipid vesicle-nanotube networks and transport of molecules therein," *Nature Protocols,* vol. 6, no. 6, p. 791, 2011, doi: 10.1038/nprot.2011.321.
[36] A. Karlsson, M. Karlsson, R. Karlsson, K. Sott, A. Lundqvist, M. Tokarz, and O. Orwar, "Nanofluidic networks based on surfactant membrane technology," *Analytical Chemistry,* Article vol. 75, no. 11, pp. 2529-2537, 2003, doi: 10.1021/ac0340206.
[37] E. S. Köksal, S. Liese, I. Kantarci, R. Olsson, A. Carlson, and I. Gözen, "Nanotube-Mediated Path to Protocell Formation," *ACS Nano,* Article 2019, doi: 10.1021/acsnano.9b01646.
[38] G. Murtas, "Early self-reproduction, the emergence of division mechanisms in protocells," *Mol Biosyst,* vol. 9, no. 2, pp. 195-24, 2013, doi: 10.1039/c2mb25375e.
[39] T. F. Zhu and J. W. Szostak, "Coupled Growth and Division of Model Protocell Membranes," *J. Am. Chem. Soc,* vol. 131, no. 15, pp. 5705-5713, 2009, doi: 10.1021/ja900919c.
[40] İ. Gözen, "A hypothesis for protocell division on the early earth," *ACS Nano,* Review vol. 13, no. 10, pp. 10869-10871, 2019, doi: 10.1021/acsnano.9b06584.
[41] K. Sott, T. Lobovkina, L. Lizana, M. Tokarz, B. Bauer, Z. Konkoli, and O. Orwar, "Controlling Enzymatic Reactions by Geometry in a Biomimetic Nanoscale Network," *Nano Letters,* vol. 6, no. 2, pp. 209-214, 2006, doi: 10.1021/nl052078p.
[42] S. Bingaman, V. H. Huxley, and R. E. Rumbaut, "Fluorescent Dyes Modify Properties of Proteins Used in Microvascular Research," *Microcirculation,* vol. 10, no. 2, pp. 221-231, 2003, doi: 10.1038/sj.mn.7800186.
[43] L. D. Hughes, R. J. Rawle, and S. G. Boxer, "Choose your label wisely: water-soluble fluorophores often interact with lipid bilayers," *PLoS One,* vol. 9, no. 2, pp. e87649-e87649, 2014, doi: 10.1371/journal.pone.0087649.
[44] J. L. Tymoczko, J. M. Berg, and L. Stryer, *Biochemistry : a short course*, 3rd ed. New York: Macmillan, 2015.
[45] J. Jouhet, "Importance of the hexagonal lipid phase in biological membrane organization," *Front Plant Sci,* vol. 4, pp. 494-494, 2013, doi: 10.3389/fpls.2013.00494.
[46] H.-J. Butt, K. Graf, and M. Kappl, *Physics and chemistry of interfaces*, 3rd, revised and enlarged ed. Weinheim: Wiley-VCH, 2013.
[47] D. van Swaay and A. deMello, "Microfluidic methods for forming liposomes," *Lab Chip,* vol. 13, no. 5, pp. 752-767, 2013, doi: 10.1039/c2lc41121k.
[48] K. J. Seu, L. R. Cambrea, R. M. Everly, and J. S. Hovis, "Influence of Lipid Chemistry on Membrane Fluidity: Tail and Headgroup Interactions," *Biophysical Journal,* vol. 91, no. 10, pp. 3727-3735, 2006, doi: 10.1529/biophysj.106.084590.

[49] N. A. Campbell, L. A. Urry, M. L. Cain, S. A. Wasserman, P. V. Minorsky, and J. B. Reece, *Biology : a global approach*, 11th ed. New York: Pearson Education, 2018.
[50] M. M. Hanczyc, S. S. Mansy, and J. W. Szostak, "Mineral Surface Directed Membrane Assembly," *Orig Life Evol Biosph*, vol. 37, no. 1, pp. 67-82, 2007, doi: 10.1007/s11084-006-9018-5.
[51] P. G. de Gennes, "Wetting: statics and dynamics," *Reviews of Modern Physics*, vol. 57, no. 3, pp. 827-863, 1985, doi: 10.1103/RevModPhys.57.827.
[52] W. Helfrich, "Elastic Properties of Lipid Bilayers: Theory and Possible Experiments," *Zeitschrift für Naturforschung C. A journal of biosciences*, vol. 28, no. 11, pp. 693-703, 1973, doi: 10.1515/znc-1973-11-1209.
[53] R. Phillips, J. Kondev, J. Theriot, and H. G. Garcia, *Physical Biology of the Cell*. Garland Science, 2013.
[54] E. Sackmann, "Membrane bending energy concept of vesicle- and cell-shapes and shape-transitions," *FEBS letters*, vol. 346, no. 1, pp. 3-16, 1994, doi: 10.1016/0014-5793(94)00484-6.
[55] S. Jõemetsa, K. Spustova, K. Kustanovich, A. Ainla, S. Schindler, S. Eigler, T. Lobovkina, S. Lara-Avila, A. Jesorka, and I. Gözen, "Molecular Lipid Films on Microengineering Materials," *Langmuir*, vol. 35, no. 32, pp. 10286-10298, 2019, doi: 10.1021/acs.langmuir.9b01120.
[56] I. Gözen, P. Dommersnes, I. Czolkos, A. Jesorka, T. Lobovkina, and O. Orwar, "Fractal avalanche ruptures in biological membranes," *Nature Materials*, vol. 9, no. 11, pp. 908-912, 2010/11/01 2010, doi: 10.1038/nmat2854.
[57] I. Gözen, "The self-spreading double bilayer/Advances in lipid membrane nanotechnology," ed, 2013.
[58] P. G. Dommersnes, O. Orwar, F. Brochard-Wyart, and J. F. Joanny, "Marangoni transport in lipid nanotubes," *Europhysics letters*, vol. 70, no. 2, pp. 271-277, 2005, doi: 10.1209/epl/i2004-10477-9.
[59] T. Bilal and I. Gzen, "Formation and dynamics of endoplasmic reticulum-like lipid nanotube networks," *Biomater. Sci.*, vol. 5, no. 7, pp. 1256-1264, 2017, doi: 10.1039/c7bm00227k.
[60] M. J. Hope, M. B. Bally, L. D. Mayer, A. S. Janoff, and P. R. Cullis, "Generation of multilamellar and unilamellar phospholipid vesicles," *Chemistry and physics of lipids*, vol. 40, no. 2, pp. 89-107, 1986, doi: 10.1016/0009-3084(86)90065-4.
[61] E. S. Köksal, P. F. Belletati, G. Reint, R. Olsson, K. D. Leitl, I. Kantarci, and I. Gözen, "Spontaneous formation and rearrangement of artificial lipid nanotube networks as a bottom-up model for endoplasmic reticulum," *Journal of Visualized Experiments*, Article vol. 2019, no. 143, 2019, Art no. e58923, doi: 10.3791/58923.
[62] E. S. Köksal, S. Liese, L. Xue, R. Ryskulov, L. Viitala, A. Carlson, and I. Gözen, "Rapid Growth and Fusion of Protocells in Surface-Adhered Membrane Networks," *Small (Weinheim an der Bergstrasse, Germany)*, vol. 16, no. 38, pp. 2002529-n/a, 2020, doi: 10.1002/smll.202002529.
[63] M. Wilson. "Immersion Objectives: Using Oil, Glycerol, or Water to Overcome some of the Limits of Resolution." https://www.leica-microsystems.com/science-lab/immersion-objectives-using-oil-glycerol-or-water-to-overcome-some-of-the-limits-of-resolution/ (accessed May 03, 2021).

[64] W. Ockenga. "Fluorescence in Microscopy." https://www.leica-microsystems.com/science-lab/fluorescence-in-microscopy/ (accessed May 03, 2021).
[65] D. H. Shin, M. Mamun, J. Almonte, C. Margraves, Y. T. Kang, S.-H. Lee, and C. K. Choi, "A Noninvasive Method to Predict Fluid Viscosity and Nanoparticle Size using Total Internal Reflection Fluorescence Microscopy (TIRFM) Imaging," *Microfluidics and Nanofluidics,* vol. 20, 02/23 2016, doi: 10.1007/s10404-016-1710-9.
[66] H. H. Jaffe and A. L. Miller, "The fates of electronic excitation energy," *J. Chem. Educ,* vol. 43, no. 9, p. 469, 1966, doi: 10.1021/ed043p469.
[67] T. J. Fellers and M. W. Davidson. "Introduction to Confocal Microscopy." https://www.olympus-lifescience.com/en/microscope-resource/primer/techniques/confocal/confocalintro/ (accessed May 03, 2021).
[68] W. Ockenga. "Differential Interference Contrast (DIC)." https://www.leica-microsystems.com/science-lab/differential-interference-contrast-dic/ (accessed May 03, 2021).
[69] A. Ainla, G. D. M. Jeffries, R. Brune, O. Orwar, and A. Jesorka, "A multifunctional pipette," *Lab Chip,* vol. 12, no. 7, pp. 1255-1261, 2012, doi: 10.1039/c2lc20906c.
[70] A. Ainla, E. T. Jansson, N. Stepanyants, O. Orwar, and A. Jesorka, "A Microfluidic Pipette for Single-Cell Pharmacology," *Anal. Chem,* vol. 82, no. 11, pp. 4529-4536, 2010, doi: 10.1021/ac100480f.
[71] R. Karlsson, M. Karlsson, A. Karlsson, A.-S. Cans, J. Bergenholtz, B. Åkerman, A. G. Ewing, M. Voinova, and O. Orwar, "Moving-Wall-Driven Flows in Nanofluidic Systems," *Langmuir,* vol. 18, no. 11, pp. 4186-4190, 2002, doi: 10.1021/la025533v.
[72] M. Tokarz, B. Hakonen, P. Dommersnes, O. Orwar, and B. Åkerman, "Electrophoretic Transport of Latex Particles in Lipid Nanotubes," *Langmuir,* vol. 23, no. 14, pp. 7652-7658, 2007, doi: 10.1021/la700336u.
[73] H. Zhang, "Artificial and Intercellular Nanotubes," Doctor of Philosophy PhD, Department of Chemical and Biological Engineering, Chalmers University of Technology, 2013.
[74] C. Kappel and R. Eils, "Fluorescence recovery after photobleaching with the Leica TCS SP2," 2004.
[75] I. Gozen and P. Dommersnes, "Pore dynamics in lipid membranes," *The European physical journal. ST, Special topics,* vol. 223, no. 9, pp. 1813-1829, 2014, doi: 10.1140/epjst/e2014-02228-5.
[76] K. Spustova, E. S. Köksal, A. Ainla, and I. Gözen, "Subcompartmentalization and Pseudo-Division of Model Protocells," *Small (Weinheim an der Bergstrasse, Germany),* vol. 17, no. 2, pp. e2005320-n/a, 2021, doi: 10.1002/smll.202005320.
[77] T. Lobovkina, P. Dommersnes, J.-F. Joanny, J. Hurtig, and O. Orwar, "Zipper dynamics of surfactant nanotube Y junctions," *Phys Rev Lett,* vol. 97, no. 18, pp. 188105-188105, 2006.
[78] I. Derényi, F. Jülicher, and J. Prost, "Formation and interaction of membrane tubes," *Phys Rev Lett,* vol. 88, no. 23, pp. 238101-2381014, 2002, doi: 10.1103/PhysRevLett.88.238101.
[79] L. Lizana and Z. Konkoli, "Diffusive transport in networks built of containers and tubes," *Phys Rev E Stat Nonlin Soft Matter Phys,* vol. 72, no. 2 Pt 2, pp. 026305-026305, 2005, doi: 10.1103/PhysRevE.72.026305.

[80] E. Stellwagen and N. C. Stellwagen, "Determining the electrophoretic mobility and translational diffusion coefficients of DNA molecules in free solution," *Electrophoresis,* vol. 23, no. 16, pp. 2794-2803, 2002, doi: 10.1002/1522-2683(200208)23:16<2794::AID-ELPS2794>3.0.CO;2-Y.
[81] P. Kapusta, "Absolute Diffusion Coefficients: Comilation of Reference Data for FCS Calibration," ed, 2010.
[82] A. Werner, "Predicting translational diffusion of evolutionary conserved RNA structures by the nucleotide number," *Nucleic Acids Res,* vol. 39, no. 3, pp. e17-e17, 2011, doi: 10.1093/nar/gkq808.
[83] Y. Shibata, J. Hu, M. M. Kozlov, and T. A. Rapoport, "Mechanisms shaping the membranes of cellular organelles," *Annu Rev Cell Dev Biol,* vol. 25, no. 1, pp. 329-354, 2009, doi: 10.1146/annurev.cellbio.042308.113324.
[84] S. L. Schmid and V. A. Frolov, "Dynamin: Functional Design of a Membrane Fission Catalyst," *Annu Rev Cell Dev Biol,* vol. 27, no. 1, pp. 79-105, 2011, doi: 10.1146/annurev-cellbio-100109-104016.
[85] Q. P. Tran, Z. R. Adam, and A. C. Fahrenbach, "Prebiotic Reaction Networks in Water," *Life (Basel),* vol. 10, no. 12, p. 352, 2020, doi: 10.3390/life10120352.

Appendix

The phospholipids from the lipid extracts used in this thesis are listed in **Table 7** and **Table 8**. These are all phosphopglycerides that were mentioned to be the most abundant membrane lipids in section **2.1.1.**

Table 7: SPL lipid content

Lipids	**wt%**
PC	45.7
PE	22.1
PI	18.4
PA	6.9
Unknown	6.9
Total	100.0

Table 8: EPL lipid content

Lipids	**wt%**
PC	67.0
PG	23.2
DPG	9.8
Unknown	0.0
Total	100.0

After the FAM-DNA exposure in **Fig. 29**, the PNN was exposed to ATTO488 as shown in **Figure 50**. The fluorescence intensity from the ATTO488 fluorophores inside the protocells in **Fig. 50** is higher compared to the fluorescence from FAM-DNA (**Fig. 29d**). The FRAP experiment following this encapsulation, resulted in the spreading in **Fig. 36**.

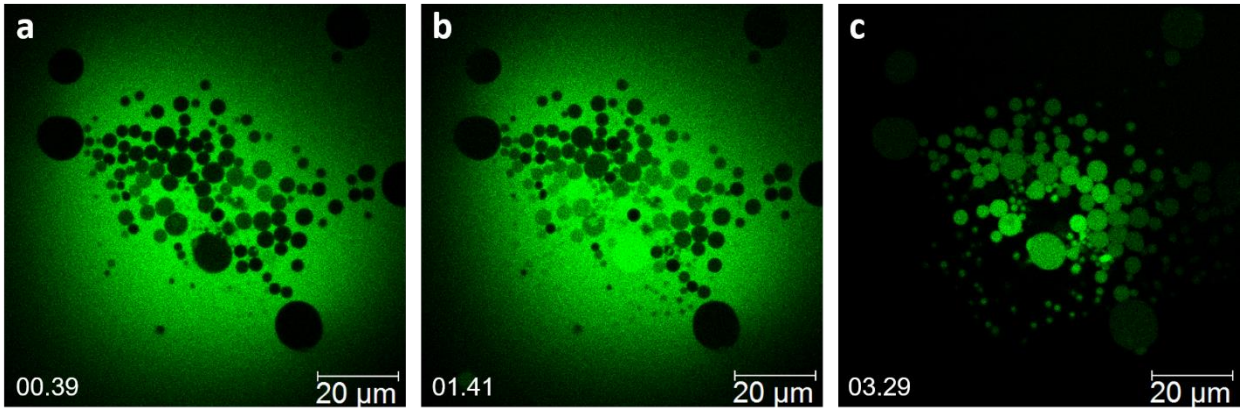

Figure 50: ATTO488 exposure to a PNN for 3 min and 30 s.